Lancaster University

Magnetic field generation in plasmas driven by Weibel-like instabilities

Cinzia Chiappetta, PhD thesis

Physics Department

Lancaster University

A thesis submitted for the degree of

Doctor of Philosophy

July, 2024

Magnetic field generation in plasmas driven by Weibel-like instabilities

Cinzia Chiappetta, PhD thesis.
Physics Department of Lancaster University, Lancaster University

Abstract

The origin of magnetic fields in astrophysics remains one of the most crucial scientific questions, given that their temporal and spatial scales are fundamental for explaining observations of energetic events such as gamma-ray bursts (GRBs) and supernova remnants (SNRs). It is now widely recognised that the creation and intensification of magnetic fields depend significantly on plasma instabilities. For instance, the Weibel instability (WI), also known as the current filamentation instability (CFI), can amplify magnetic fields and lead to the formation of electromagnetic shock waves, where particles can be accelerated to high energies while emitting strong bursts of radiation. Significant efforts have been made to reproduce these fundamental mechanisms in the laboratory through experiments that preserve the scale differences of astrophysical scenarios. Due to advancements in sophisticated simulation tools, it is now possible to understand a wide range of astrophysical problems and develop laboratory experiments to replicate these events. In this thesis, I examine the onset and long-term development of the CFI in counterstreaming electron-ion flows. Using two-dimensional kinetic simulations performed with the semi-implicit energy-conserving code ECsim, I investigate the evolution of the instability on ion timescales. The numerical results indicate that the magnetic field driven by the instability survives for hundreds of ion plasma periods. The instability produces magnetic field filaments that evolve from sub-electron scales to beyond the ion inertial length, depending on the flow velocity and the plasma anisotropy. The ion anisotropy, which remains substantial throughout the simulations, sustains the coalescence process of magnetic filaments. In the second phase of the numerical investigation into CFI, I studied the interaction between a neutral ultra-relativistic electron-positron beam and a magnetised plasma using the PIC code OSIRIS. I investigated how a pre-existing magnetic field, oriented parallel to the beam propagation, modifies the growth and saturation of kinetic instabilities. Without a magnetic field, the dominant instability is the CFI, which causes modes perpendicular to the direction of the beam. By increasing the strength of the magnetic field, it is possible to observe a transition toward progressively more oblique modes. The growth rate of

these modes is smaller than that of the CFI. In all cases, these instabilities generate a magnetic field perpendicular to both the beam velocity and the wavenumber. These simulations indicate that the instability-driven field reaches higher values at saturation in the presence of higher degrees of magnetisation. The effect of longitudinal beam variation was also explored, demonstrating that even less dense, longer longitudinal beams can still cause kinetic instabilities, although the magnetic field grows at a slower rate. Finally, to probe the physics underpinning the interaction in the laboratory, I examined the propagation of the electron beam into the plasma, considering the CLARA laboratory parameters. The preliminary results show the growth of the electric field components and the transverse magnetic field.

Contents

List of Figures

List of Tables

Chapter 1

Introduction

1.1 Importance of magnetic field generation and plasma microinstabilities in astrophysical contexts

Understanding how the magnetic field is generated and evolves in plasmas is of great importance for the study of astrophysical scenarios.

Synchrotron radiation associated with processes such as gamma-ray bursts (GRBs), supernova remnant (SNRs) and pulsar wind outflows hints at the presence of strong magnetic fields [1], [2]. The latter fields are usually related to collisionless shock waves and colliding plasmas [3], [4], but a full modelling of their origin and long-term evolution is still lacking.

Collisionless shocks are found across various astrophysical environments, where there is a significant release of energy over a short period, such as in active galaxy nuclei (AGNs), pulsar wind nebulae, and SNRs. These shocks are also responsible for producing non-thermal particles, such as cosmic rays (CRs) [5]. A shock, which may be defined as a discontinuity in the macroscopic plasma state can develop when fast plasma flows are present. At a macroscopic level, a shock is characterised by a sudden and pronounced change in the plasma state [6]. The discontinuity in the plasma state in hydrodynamic shock waves is caused by collisional effects that irreversibly dissipate the kinetic energy of the fluid crossing the shock. However, in the absence of particle collisions, plasma microinstabilities can be responsible for the dissipation of kinetic energy, leading to the formation of shocks in the plasma [3], [7], [8].

In astrophysical contexts such as AGNs and GRBs, collisionless kinetic instabilities are being considered as potential explanations for the origin of magnetic fields. These instabilities may play a role in generating the magnetic fields observed in these phenomena [3], [9]. Among the different instabilities, the Weibel instability and the

current filamentation instability (CFI) are known to provide efficient mechanisms for the generation of magnetic fields in unmagnetised plasmas [10], [11]. The Weibel instability occurs when there is an anisotropy in the velocity distribution of particles in the plasma. This anisotropy can arise from various processes, such as shock formation or laser-plasma interactions. When such an anisotropy exists, it leads to the filamentation of current within the plasma, resulting in the formation of small scale current filaments. These filaments then give rise to localied magnetic fields due to the Ampere's law, which states that a current produces a magnetic field around it. The CFI, on the other hand, is driven by current perpendicular to an external magnetic field. When there is a sufficient gradient in the current density perpendicular to the magnetic field, small perturbations in the current density can grow rapidly through the process of filamentation. This leads to the formation of filamentary structures in the plasma, accompanied by the generation of magnetic fields. These instabilities can mediate the formation of collisionless shocks, which can accelerate particles to high energies [3], [7], [8].

The material released by SNRs typically moves at non-relativistic speeds (up to 10% the speed of light) [12], meanwhile, shocks in the other astrophysical environments mentioned above are propelled by relativistic and even ultra-relativistic streams. Indeed, electromagnetic instabilities develop in each of these systems as a result of the ejected plasma interacting with the surrounding medium. These instabilities can produce strong fields, enough to isotropise the flows and eventually drive shock formation. In these cases, information on accelerated particle dynamics can be retrieved by indirect astrophysical observations that rely on the high-energy particle radiation spectrum. SNRs have contributed the majority of the information available, and evidence of a synchrotron spectrum is particularly clear in SN1006. Figure 1.1 provides Advanced Satellite for Cosmology and Astrophysics (ASCA) satellite X-ray measurements of the supernova SN1006 remnant [13]. These observations demonstrate that the emissions from the edges of the remaining shell are dominated by radiation from electrons. Inside the shock front, electrons were accelerated to an energy of roughly 100 TeV. Very high-energy CRs are probably the product of ion acceleration at energies similar to those in the shell [13].

Many astrophysical phenomena, including GRBs, have shown how essential large-scale magnetic fields are [14]. Also in these cases, electromagnetic plasma microinstabilities can provide the powerful magnetic fields needed to explain the non-thermal radiation. Gamma-ray bursts manifest in two distinct phases: an initial burst of radiation dominated by high-energy emissions, followed by a longer-lasting afterglow emitting across various wavelengths. Recent observations have unveiled that certain GRBs emit in the TeV band, expanding the comprehension of these phenomena. These bursts originate from ultra-fast jets emitted by compact objects, resulting in two phases of emission: the initial burst and the subsequent

Figure 1.1: SN1006 from NASA's Chandra X-ray Observatory revealing SNR. The colour in the figure shows the radio (red), X-ray (blue) and visible light (yellow). SN1006 is located about $7,000$ light years from Earth [13].

afterglow. Indeed, measurements of GRBs in the afterglow zone seem to indicate that synchrotron emission, which can only be explained by the existence of strong magnetic fields, is the most plausible source for the fast emission [15]. GRBs are considered the brightest objects in the cosmos [1]. They were accidentally detected in the late 1960s by U.S. military spy satellites called Vela [16], which were launched to search for possible Soviet nuclear tests in violation of the Treaty on the Prohibition of Nuclear Weapons Tests in the Atmosphere, signed in 1963. These satellites were equipped with gamma-ray detectors since a nuclear explosion produces gamma-rays. After that, several GRBs have been observed. In 1991, the Burst and Transient Source Experiment (BATSE) was launched to understand the source of these mysterious events. For nine years, the sky was observed and thousands of GRBs were recorded. In March 2000, BATSE published startling results that seemed to confirm the cosmic distribution of GRBs as shown Fig. 1.2. The physics of GRBs is still unclear, although numerous satellites are nowadays engaged in observing them. A GRB event is a rare event that can last from one millisecond to tens of minutes, often reaching a peak energy of 100 keV. Gamma-ray burst photons typically carry significantly higher energies compared to photons emitted by the Sun. GRB photons are often detected with energies ranging from a few hundred kiloelectronvolts (keV) to several megaelectronvolts (MeV). In contrast, photons emitted by the Sun are mainly in the visible light range, peaking around 1 to 3 electronvolts (eV), corresponding to the visible spectrum. Light from a typical GRB is also hundreds of times brighter than that from a typical supernova. Most GRBs observed so far emit energy E on the order
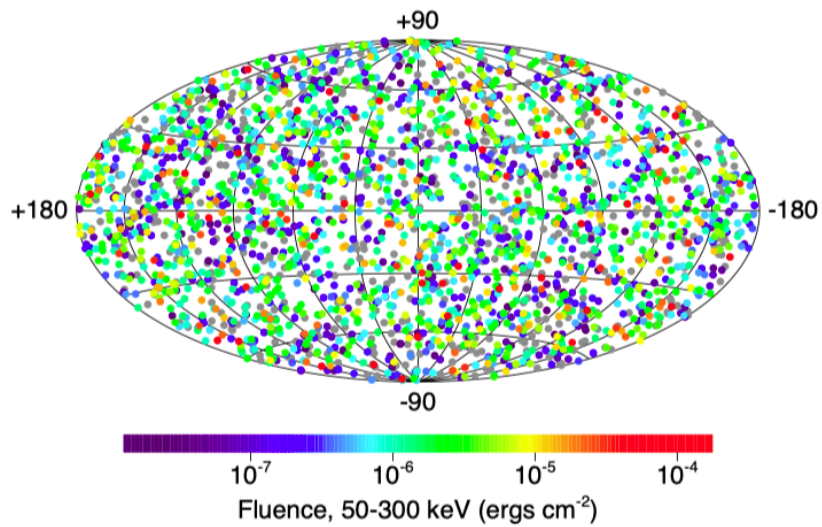
Figure 1.2: Location of 2704 GRBs recorded by the BATSE satellite. The projection is in galactic coordinates; the plane of the Milky Way Galaxy is along the horizontal line in the middle of the figure. The burst locations are colour-coded based on the fluence, which is the energy flux of the burst integrated over the total duration of the event. Long duration, bright bursts appear in red, and short duration, weak bursts appear in purple. Grey is used for bursts for which the fluence cannot be calculated due to incomplete data [17] .

of approximately 10^{51-54} erg, which is about a few per cent of an almost complete conversion of the Sun mass into radiant energy. The time T_{90} during which 90% of the outburst energy is visible is commonly used to divide GRBs into two groups: long outbursts with $T_{90} > 2\,\text{s}$ and short outbursts with $T_{90} < 2\,\text{s}$. The gamma-ray photons of the outbursts often reach a peak value of a few hundred keV and have a non-thermal spectrum that can be described with a power law:

$$N(E)dE \propto E^{-\beta}dE, \tag{1.1}$$

with a spectral index $\beta \approx 2$, where N is the number of photons with energy E [18]. The rate of detected GRBs is about one burst per day. The object or the system of objects responsible for the GRBs, the so called internal engine, is still unknown, due to the optical thickness of the engine which impedes direct observations. It is unclear how such an emission might occur from a small source. The discovery of GRB 030329 indicates that catastrophic star deaths involving core collapse can produce GRBs [19].

There is a compactness problem that is related to these energetic events and arises due to the large energy involved in a short time variability. A small percentage of high energy gamma-ray photons can be seen in the measured GRB spectrum. These photons can form electron-positron couples when they interact with photons of lower energy via $\gamma\gamma \longrightarrow e^+e^-$. Considering a fluence F of gamma-rays for an isotropic source of size R_i at a distance D, the initial optical depth $\tau_{\gamma\gamma}$ for the pair production process is defined as:

$$\tau_{\gamma\gamma} = \frac{f_p \sigma_T F D^2}{R_i^2 m_e c}, \tag{1.2}$$

where f_p is the fraction of photons involved in the process, σ_T is the Thomson cross-section, m_e the electron or positron mass and c is the speed of light in vacuum [18]. The optical depth measures how likely a photon is to scatter when passing through a medium with charged particles. Higher optical depth means a greater chance of scattering. In dense environments, like those where pair production occurs, optical depth also indicates the likelihood of high-energy photons producing particle pairs as they travel through the medium. It would be impossible to observe the radiation released by the source because, for typical GRB conditions, the resulting optical depth $\tau_{\gamma\gamma}$ is incredibly thick [20]. By supposing that gamma-rays are produced by ultra-relativistic sources travelling towards us, the compactness problem can be solved. In this regime, the fraction of photons f_p is smaller by a factor $\gamma^{-2\beta}$ and the radius from which the radiation is emitted is larger by a factor γ^2, where γ is the Lorentz factor of the source moving towards an observer at rest and β is the spectral index of the emission. The optical depth of Eq. (1.2) is then reduced by a factor γ^β. The compactness problem can then be resolved by assuming sources moving relativistically towards us with a Lorentz factor $\gamma \approx 100$. This result led to the relativistic fireball model, which explains gamma-ray production and afterglow.

1.1.1 The fireball beam model

The fireball model is one of the few models proposed to explain why GRBs have such high energy levels [1], [21], [22]. It also tries to explain the time scales that govern them, as well as why they produce an afterglow. Moreover, the model contributes to answering important questions about GRBs, such as why they are so variable over short time scales. The interaction of the fireball beam, which has relativistic factors ranging from 10^2 to 10^6, with the external medium can drive plasma kinetic instabilities, which generate field structures that accelerate particles to high energies. As particles accelerate to such high speeds, their kinetic energy is dissipated to produce strong radiation bursts with wavelengths ranging from gamma-rays to radio waves. The remainder of the energy is stored in the interstellar medium (ISM) and creates the observed afterglow. The central idea behind the fireball model is that gamma-ray emission in GRBs occurs behind a shock that has evolved within a shell moving with a Lorentz factor greater than one.

Figure 1.3 shows a schematic diagram of the internal/external shock model that evolves in four stages: 1) a compact source (not directly observable) generates a relativistic energy flow; 2) the energy is relativistically transferred from the source regions; 3) when faster shells pass slower ones, a shock is formed, converting the kinetic energy of the relativistic ejecta into interior energy of accelerated particles, then, the visible gamma-rays are produced; 4) the afterglow is caused by the surrounding ISM, which further slows down the relativistic outflow, whose speed has already been reduced but not stopped by the internal shocks. The internal shocks refer to collisions that occur within the relativistic outflow ejected from the central source. This outflow consists of shells of material moving at different velocities. As these shells propagate outward, the faster-moving ones catch up to and collide with the slower-moving ones.

The scientific community generally agrees that plasma instabilities are reasonable mechanisms for magnetic field generation in GRBs. These plasma instabilities occur naturally. Sources of free energy in the plasma, which might be connected to anisotropies or shear velocities can rapidly lead to instabilities and produce the magnetic fields necessary to explain non-thermal radiation [24]. When a GRB explodes, it ejects a dense relativistic jet into the interstellar plasma. As a result, a return current may form, and plasma microinstabilities can be triggered. In many cases, the simultaneous growth of longitudinal and transverse instabilities results in the exponential amplification of oblique modes, which are combinations of these instabilities. It is known that these instabilities can produce strong magnetic fields [25]. These intense magnetic fields scatter charged particles, causing the emission of electromagnetic radiation.
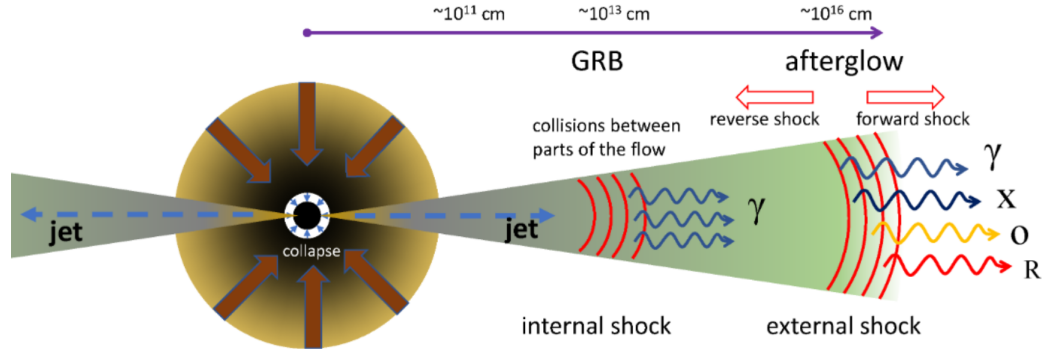
Figure 1.3: The fireball model for GRB and afterglow generation [26]. The fireball model is a theoretical model used to explain the generation of GRBs and their afterglows. According to this model, GRBs are produced when a massive star collapses into a black hole or a neutron star, and the resulting explosion generates afterglows at progressively longer wavelengths from gamma-ray, X-ray to optical (O) and radio (R) bands.

1.2 Relevance of magnetic field generation and plasma microinstabilities for laboratory plasmas

The generation of magnetic fields in plasmas is not only relevant in astrophysical frameworks, but also in laser-plasma experiments.

The availability of ultra-intense (intensities $> 10^{19} \, \text{W/cm}^2$) and ultra-short (duration $\approx$ fs) laser pulses and ultra-relativistic particle beams has opened the possibility of mimicking astrophysical environments in the laboratory [27]–[29]. The physics underpinning astrophysical events can be thus clarified by the design of properly scaled laboratory experiments, which leverage these technologies.

In particular, plasma microinstabilities relevant to magnetic field generation have been explored in the laboratory through the interpenetration of counterstreaming collisionless plasma flows [29]–[31]. The experimental setup typically involves two solid targets that are irradiated by laser pulses to create two interpenetrating plasma flows. This configuration is favorable for the development of the CFI, which arises due to the interaction between the two counterstreaming plasmas. As the two plasma flows interact, the CFI may also lead to the formation of two collisionless shock fronts spreading away from each other, with the shocked plasma in between. Understanding how these shocks form and evolve is important for a wide range of astrophysical
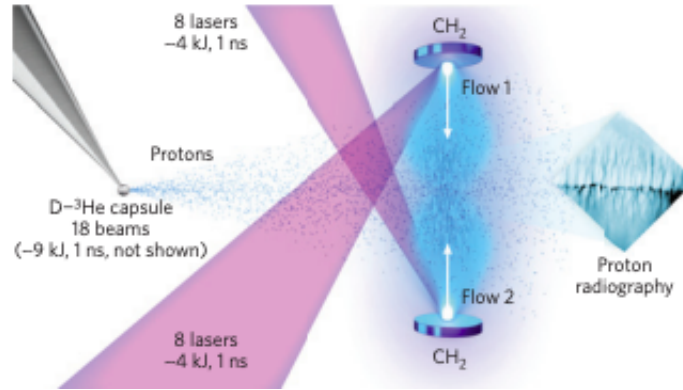
Figure 1.4: Experimental setup to produce two counterstreaming plasmas by irradiating two plastic targets with kJ-ns laser pulses. Proton radiography is used to examine the interaction zone [30].

systems, including SNRs, GRBs, and AGN. Several studies have shown magnetic field creation via Weibel-like instabilities in interpenetrating flows [27], [29], [30]. The configuration shown in Fig. 1.4, obtained at the OMEGA Laser Facility, involved the interpenetration of flows with a density of $n_e \approx 5 \times 10^{18}\,\mathrm{cm}^{-3}$ and a measured plasma velocity of $1000/2000\,\mathrm{km\ s}^{-1}$ [30]. Proton radiography was used to investigate the interaction zone, revealing the filamentary structure typical of the early stages of the CFI.

An analogous configuration with higher plasma density ($n_e \approx 10^{19}\,\mathrm{cm}^{-3}$) has been investigated at the National Ignition Facility. In this experimental campaign symmetric and counterstreaming plasma flows were produced by the ablation of deuterated carbon targets with each target irradiated by 84 laser beams [32]. X-ray self-emission measurements from the plasma indicate the formation of a strongly compressed and heated zone when the two flows interact. This interaction region becomes Weibel-unstable, potentially driving the development of two collisionless shock fronts propagating away from each other within the plasma, with the shocked plasma situated in between. The processes related to the development of the Weibel instability and of Weibel-mediated collisionless shocks in the context of laboratory astrophysics is confirmed by electron energy measurement. These measurements show that electrons can be accelerated to relativistic non-thermal energy levels through small-scale turbulence induced during the shock transition. This particular experiment is relevant to understand electron acceleration at shocks in young SNRs [32].

The CFI has been driven in the laboratory also via the interaction of an ultra-relativistic electron beam with a static plasma [33]. The experiment involved a

plasma-filled vacuum chamber created by ionising a gas with an electric discharge. A high-current electron beam generated outside the chamber was then injected into the plasma. Optical imaging techniques were used to measure the properties of the plasma and to image the possible formation of current filaments due to the instability. The study showed that when the transverse size of the relativistic electron beam is sufficiently large, the propagation of the beam drives the CFI, which manifests by splitting the beam into filaments. The filaments are observed to grow in both length and diameter over time and their growth rate appears to be strongly influenced by the plasma density and beam current [33], [34]. These series of experiments inspired novel proposals to investigate the CFI using a quasi-neutral fireball beam composed of electrons and positrons instead of an electron beam only [35], [36]. It is important to note that the polarisation of the synchrotron radiation emitted by a fireball beam is significantly impacted by the presence of weak magnetic field background. Therefore, understanding the structure and composition of current filaments and fields generated by the CFI in the presence of a background magnetic field is crucial for the interpretation of recent observations [37]–[39]. It is important to notice that this setup is particularly relevant to mimicking GRBs in the laboratory [40].

Simulation results reveal the possibility of driving Weibel-like instabilities and turbulent fields also when an intense laser pulse impinges on an overdense or near-critical target [41]–[44]. In this context, a near-critical target denotes a plasma whose density closely approaches the critical density corresponding to the laser wavelength employed in the interaction. The laser can either generate strong temperature anisotropies [45] or act as a piston and generate a fast flow of electrons [41]. In the first case, the temperature anisotropy causes the development of the Weibel instability. In the second case, similarly to that is thought to occur in astrophysics, the stream of electrons flowing through the target is balanced by a return current which creates the counterstreaming flows that lead to the CFI. In both cases a strong long-living magnetic field is produced whose characteristics could be probed with relevant diagnostics.

In recent experimental investigations, the growth and saturation of the electron Weibel instability were observed by employing a moderate-intensity laser and a gas target. The plasma, characterised by controlled density and temperature, was generated through the process of ionisation induced by intense laser fields [46], [47]. The growth and saturation of the electron Weibel instability in the created plasma were directly observed [46]. The evolution of magnetic fields was observed, revealing the formation of a distinct helicoid structure associated with the electron thermal Weibel instability. The study identified magnetic trapping as the dominant saturation mechanism. Furthermore, the analysis of electron velocity distributions indicated the presence of further instabilities, which led to a more uniform electron distribution.

Finally strong magnetic fields developing on the back of solid targets due to Weibel-

like instabilities have been reported also by teams performing experiments on laser-driven ion acceleration [48]–[50]. In these cases, the magnetic field resulted in an unexpected spatial modulation of the produced proton beams, which deteriorated their quality. Therefore, in these cases it is crucial to understand the conditions to quench the instability.

Magnetic field generation due to the CFI has also crucial relevance for fast ignition [51], a promising alternative to more conventional inertial confinement fusion approaches, where fusion is achieved via hydrodynamic compression of a deuterium-tritium pellet [52]. In the fast ignition scheme, compression and ignition occur separately. Initially, a suitable driver is used to compress the deuterium-tritium pellet to very high densities. After this phase, an external source is employed to ignite the compressed fuel, as depicted in Fig. 1.5. This requires lower driver energy with respect to the hydrodynamic approach and thus it allows for achieving higher energy gains. Additionally, the impact of asymmetries and hydrodynamic instabilities is reduced [51]. The original idea behind fast ignition was to use a second short pulse laser to generate relativistic electrons in the tenuous plasma corona surrounding the compressed pellet [51]. Later, it was also proposed to implant a gold cone on the fuel pellet to guide the laser and ensure a more stable laser-plasma interaction [53], [54]. Fast electrons travel through the target and deposit their energy in the compressed core, which gets heated to million of degrees celsius. In turn, this produces the ignition spark that initiates the thermonuclear reaction chain. It was noted that in order to deposit their energy in the core, fast electrons must propagate through the micrometer long corona whose density is $10 - 1000$ times higher that the beam density and these conditions might trigger kinetic microinstabilities, such as the CFI [55]. In turn, these instabilities might consume the free energy of the electron beams and, hence, impede fusion.

1.3 Outline of the thesis

The aim of this doctoral thesis is to describe the process of the development of microinstabilities as one of the possible mechanisms for the generation of magnetic fields in plasmas. The generation and long-time evolution of magnetic fields in the CFI are studied in the first part of the thesis, while the possibility of exploring the generation of magnetic fields in unmagnetised and slightly magnetised plasmas in the laboratory using ultra-relativistic particle beams is investigated in the second part. The studies involve a combination of theoretical derivations and numerical simulations. The latter simulations were performed by employing a kinetic approach and using two different Particle-In-Cell (PIC) codes: OSIRIS and ECsim. These codes adopt different time discretisations and, as a consequence, allow for focusing on different physics regimes and spatio-temporal scales. OSIRIS is an effective instrument
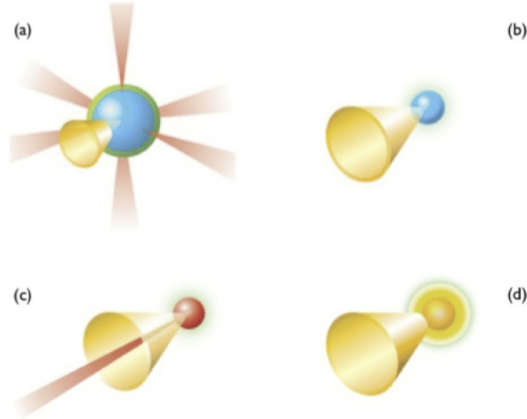
Figure 1.5: Fast ignition scheme. A capsule containing DT fuel and a gold cone is exposed to a group of symmetrically positioned laser beams (a). As a result, the material around the tip of the gold cone collapses, causing the density of the DT fuel to increase hundreds of times over that of solid matter (b). Then, a highly powerful laser is directed at the gold cone tip, resulting in the generation of numerous high-energy electrons (c). These energetic electrons travel into the dense DT fuel and deposit their energy in the compressed fuel, causing the ignition spark (d) [56].

for studying relativistic electron physics. ECsim allows for focusing on the ion physics. The thesis is organised as follows:

In **Chapter 2**, the numerical approach utilised in this thesis is described. I illustrate the main ideas behind the PIC method and report the fundamental equations upon which the technique relies. The different numerical discretisations adopted in OSIRIS and ECsim are explained and the advanteges of the two codes revealed.

In **Chapter 3**, I investigate the onset and evolution of the CFI driven by two identical counterpropagating plasmas composed of electrons and ions with realistic mass ratio. By using the code ECsim, I explore how the instability generates an intense magnetic field and how this field is amplified over time scales of hundreds of ion plasma periods and evolves towards larger and larger spatial scales. Thus this study provides an overview of the non-linear dynamics of the ion CFI on unprecedented spatial and temporal scales.

In **Chapter 4**, through 2D kinetic simulations performed with the code OSIRIS, I illustrate the physics underpinning the propagation of ultra-relativistic electron-positron fireball beams through a static slightly magnetised plasma. This study employs beam and plasma parameters attainable at the SLAC National Accelerator Laboratory. In this chapter, I also illustrated the propagation of a relativistic electron beam in a static and unmagnetised plasma. The simulation beam parameters are

achievable at CLARA, Compact Linear Accelerator for Research and Applications, located at the Cockcroft Institute of Accelerator Science and Technology.
Chapter 5 presents conclusions and perspectives for future work.

The work described in this thesis was presented at:

- C. Chiappetta, M. E. Innocenti, K. M. Schoeffler, N. Shukla, and E. Boella, On the Current Filamentation Instability in counterpropagating plasma setups, 62nd Annual Meeting of the APS Division of Plasma Physics, (fully remote meeting), 2020, (Poster contribution).

- C. Chiappetta, A numerical systematic study of the current filamentation instability of relevance for laser-solid interaction, Cockcroft Institute Postgraduate Conference, (fully remote meeting), 2020, (Oral contribution). **Award for second best presentation**.

- C. Chiappetta, M. E. Innocenti, K. M. Schoeffler, N. Shukla, and E. Boella, Numerical study of the non-linear phase of the current filamentation instability in electron-ion plasmas, 47th IOP Plasma Physics Conference, (fully remote meeting), 2021, (Poster contribution).

- C. Chiappetta, M. E. Innocenti, K. M. Schoeffler, N. Shukla, and E. Boella, On the long-term dynamics of the Current Filamentation Instability, EPS Conference on Plasma Physics, (fully remote meeting), 2021, (Poster contribution).

- C. Chiappetta, M. E. Innocenti, K. M. Schoeffler, N. Shukla, and E. Boella, The Current Filamentation Instability in the long-time evolution, National Astronomy Meeting, (fully remote meeting), 2021, (Oral contribution).

- C. Chiappetta, M. E. Innocenti, K. M. Schoeffler, N. Shukla, and E. Boella, In silico magnetic field generation in plasmas, Postgraduate Research Conference, Lancaster University, (fully remote meeting), 2021, (Poster contribution)

- C. Chiappetta, M. E. Innocenti, K. M. Schoeffler, N. Shukla, and E. Boella, Exploring the interaction between ultra-relativistic fireball beams and magnetised plasmas, 63rd Annual Meeting of the APS Division of Plasma Physics, (fully remote meeting), 2021, (Poster contribution).

- C. Chiappetta, Ultra-relativistic electron-positron beam interaction with magnetised plasma as a platform to explore processes relevant for astrophysics in the laboratory, Cockcroft Institute, Postgraduate Conference, (fully remote meeting), 2021, (Oral contribution).

- C. Chiappetta, M. E. Innocenti, K. M. Schoeffler, N. Shukla, and E. Boella, In silico magnetic field generation in plasmas, Faculty of Science and Technology Science Week, (Lancaster University), 2022, (Poster contribution).

- C. Chiappetta, M. E. Innocenti, K. M. Schoeffler, N. Shukla, and E. Boella, Numerical simulations modelling the interaction of ultra-relativistic neutral fireball beams with magnetised plasmas, EPS Conference on Plasma Physics, (fully remote meeting), 2022, (Poster contribution).

- C. Chiappetta, M. E. Innocenti, K. M. Schoeffler, N. Shukla, and E. Boella, Current filamentation instability on ion time scales, 48th IOP Annual Plasma Physics Conference, (fully remote meeting), 2022, (Oral contribution).

- C. Chiappetta, M. E. Innocenti, K. M. Schoeffler, N. Shukla, and E. Boella, Non-linear evolution of the current filamentation instability on ion time scales, 64th Annual Meeting of the APS Division of Plasma Physics, (Spokane, Washington), 2022, (Oral contribution).

This work is also currently being summarised in the following publications:

- C. Chiappetta, M. E. Innocenti, K. M. Schoeffler, N. Shukla, and E. Boella, The Current Filamentation Instability in the long-time evolution, to be submitted to The Astrophysical Journal (2023).

- C. Chiappetta, M. E. Innocenti, K. M. Schoeffler, N. Shukla, T. Silva, and E. Boella, Multidimensional simulations of ultra-relativistic particle beam interaction with magnetised plasma, to be submitted to Journal of Plasma Physics (2023).

Chapter 2

Numerical techniques to explore the onset and development of microinstabilities in collisionless plasmas

2.1 Introduction

The aim of this thesis work is the study of magnetic field generation in collisionless plasma due to Weibel-like instabilities [57]–[59]. This requires the analysis of the linear and non-linear phases of kinetic instabilities. If the linear phase of kinetic instabilities can be investigated resorting to analytical models, to explore the non-linear dynamics of plasmas during the evolution of these micro-instabilities and the interaction between particles and waves, which naturally follow their development, a numerical approach is necessary. In addition, numerical simulations are also crucial to examine multi-dimensional effects, which are hardly treated by analytical models because of the objective difficulty in carrying out calculations involving two or three dimensions. The dynamics of collisionless plasmas at a kinetic level may be described using Vlasov equation [60]. Thus, to model these plasmas using computer simulations, the Vlasov equation could be solved numerically using for instance finite difference or finite elements techniques [61]. This is what so-called Vlasov codes do by modelling the evolution of the distribution function of particles in phase space. However, the fact that the plasma distribution function is 6-dimensional makes solving Vlasov equation for all the plasma species a challenge also with modern computing resources. This is why a Lagrangian approach employing a particle method is usually adopted. This is the idea underpinning the PIC method. When adopting this technique, the motion of a large number of computational particles representative of several real plasma particles

and their interactions with the electromagnetic fields are tracked. Furthermore, modern codes implementing this numerical technique are easily parallelisable and can take full advantage of today supercomputing resources. Thus, PIC simulations have been widely used in this work to reach the pre-fixed goal. Access to the essential computational resources was crucial for conducting these simulations, made possible by utilising both the High End Computing Cluster (HEC) at Lancaster University and the Galileo 100 supercomputer at CINECA (Italy).

This chapter will describe the main ideas behind the PIC method. Particle-In-Cell techniques use both explicit and implicit methods to simulate plasma dynamics; each has distinct characteristics. Explicit schemes, such as the leapfrog system, are very efficient in terms of computing and are appropriate for well-resolved timescales such as those encountered in collisionless plasmas. Nevertheless, especially at high plasma densities, they may be subject to numerical instabilities. On the other hand, implicit approaches are more favorable for collisional plasmas or systems with stiff timescales due to their stability benefits, despite their computational intensity. Choosing between the two can be affected by various elements, including what kind of plasma being simulated, the needed resolution, and computer resources. Selecting the appropriate method involves balancing these factors to ensure accurate and efficient simulations tailored to the specific characteristics of the plasma system under study.

2.2 PIC Algorithm

In the PIC method, macro-particles are utilised to represent a large number of individual particles in the plasma. Unlike point-like particles, macro-particles have a finite-size, which introduces an important characteristic: a reduced interaction between computational particles, even when they overlap. This means that a single macro-particle can account for multiple real particles, resulting in computational efficiency while still capturing the collective behavior of the plasma. PIC techniques rely on solving the fundamental physical equations governing particle motion and electromagnetic field evolution.

The Vlasov-Maxwell system is a set of equations that most accurately describes a collisionless plasma (i.e. a plasma with $\nu/\omega_p \ll 1$, being ν the collision frequency and $\omega_p = \sqrt{4\pi n e^2/m}$ the plasma frequency and $\varepsilon_p \ll 1$, being ε_p the plasma parameter, which is the ratio of the plasma potential and kinetic energy). The Vlasov equation is given by [62]:

$$\frac{\partial f_\alpha}{\partial t} + \mathbf{v} \cdot \partial_{\mathbf{x}} f_\alpha + q_\alpha \left(\mathbf{E} + \frac{\mathbf{v} \times \mathbf{B}}{c} \right) \cdot \partial_{\mathbf{p}} f_\alpha = 0, \tag{2.1}$$

where $f_\alpha(\mathbf{x}, \mathbf{p}, t)$ is the distribution function of the species α, having mass m_α and charge q_α, $\mathbf{x} = (x, y, z)$ is the position, $\mathbf{v} = (v_x, v_y, v_z) = \mathbf{p}/m_\alpha\gamma$ is the velocity, $\mathbf{p}$ the

momentum, $\gamma = \sqrt{1 + \mathbf{p}^2/m_\alpha^2 c^2}$ the Lorentz factor. The electric and magnetic fields are $\mathbf{E}$ and $\mathbf{B}$, respectively. The Vlasov equation has to be coupled with Maxwell's equations for the description of the electromagnetic fields:

$$\nabla \cdot \mathbf{E} = 4\pi\rho, \tag{2.2}$$

$$\nabla \cdot \mathbf{B} = 0, \tag{2.3}$$

$$\nabla \times \mathbf{E} = -\frac{1}{c}\frac{\partial \mathbf{B}}{\partial t}, \tag{2.4}$$

$$\nabla \times \mathbf{B} = \frac{4\pi}{c}\mathbf{J} + \frac{1}{c}\frac{\partial \mathbf{E}}{\partial t}. \tag{2.5}$$

The charge density ρ and current density $\mathbf{J}$ for all the plasma species α are given by [62]:

$$\rho(\mathbf{x}, t) = \sum_\alpha q_\alpha \int f_\alpha(\mathbf{x}, \mathbf{p}, t) d^3p, \tag{2.6}$$

$$\mathbf{J}(\mathbf{x}, t) = \sum_\alpha q_\alpha \int \frac{\mathbf{p}}{\gamma m_\alpha} f_\alpha(\mathbf{x}, \mathbf{p}, t) d^3p. \tag{2.7}$$

The distribution function has 6 dimensions, which poses a significant challenge when attempting to solve a combination of the Vlasov and Maxwell equations (Eq. (2.1) and Eqs. (2.2)-(2.5), respectively). Such a task would require computational resources that are currently unavailable.

A simple technique for simulating the behaviour of a system of interacting particles, such as a plasma, is to track the dynamics of each of its individual particles by computing the force acting on each of them as the total of the contributions of all the particles making up the system. This approach, although extremely intuitive, is computationally expensive. For a system of N particles, each particle is subject to the interactions with $(N-1)/2$ other particles, ensuring that each pair of particles is counted only once. Consequently, the total number of operations needed to describe the system's dynamics is $N(N-1)/2$. This particle-particle method, which considers interactions between individual particles, is sometimes a requirement when dealing with strongly coupled systems. However, very often the large number of particles and the large number of the operations required make this approach inconvenient. Luckily, for weakly coupled plasmas as those of interest for this work a workaround can be adopted which make simulations feasible: the use of particle clouds. Particle clouds, called macro-particles, or computational particles are alternatives to modelling each individual point particle and may all be thought of as pieces of phase space. This approach is defined as finite-size particle approach. The Coulomb force between point-like particles is proportional to r^{-2}, with r the distance between two particles and this indicates that for $r \to 0$ the force has a singularity, while for $r \to \infty$ it

gradually decreases. This trend for large values of r is the reason behind the collective behaviour of a collisionless plasma. Finite-size particles suffer the same long-range force as point particles, but when the distance between them becomes less than their diameter, they start to overlap, causing the force to tend to 0. This behaviour allows then to avoid the singularity when finite-size particles approach each other while also precisely simulating the long-range interactions between them, *de facto* modelling the dynamics of a collisionless plasma. This suggests that a system may still be thought of as weakly coupled in finite-size particle methods even when the effective number of interacting particles is reduced [59].

In a PIC approach, the phase space is approximated by the superposition of macro-particles p, so that the distribution function of each species α can be estimated as:

$$f_\alpha(\mathbf{x}, \mathbf{p}, t) = \sum_p f_p(\mathbf{x}, \mathbf{p}, t). \tag{2.8}$$

The PIC method works by assigning a specific distribution, containing free parameters representing the particle position and velocity to each macro-particle. In this approach, the distribution function in a section of phase space where N_p computational particles are included may be characterised by a relation of the form:

$$f_p(\mathbf{x}, \mathbf{p}, t) = N_p W_x(\mathbf{x} - \mathbf{x}_p)\delta(\mathbf{p} - \mathbf{p}_p), \tag{2.9}$$

where W_x is the spatial shape function of the computational particle.

By inserting the discrete distribution function, as provided by Eq. (2.9), into the Vlasov Eq. (2.1), and considering each macro-particle independently, it can be observed that the relativistic equations of motion are satisfied by:

$$\frac{\mathrm{d}\mathbf{x}_p}{\mathrm{d}t} = \frac{\mathbf{p}_p}{m_p\gamma_p}, \tag{2.10}$$

$$\frac{\mathrm{d}\mathbf{p}_p}{\mathrm{d}t} = q_p\left(\mathbf{E}_p + \frac{\mathbf{v}_p}{c} \times \mathbf{B}_p\right), \tag{2.11}$$

where the subscript p is used to indicate the pth particle, with $p = 1, 2, \cdots N_p$.

The PIC algorithm has several implementations that depend on the temporal discretisation adopted for Maxwell's and motion equations. The forthcoming sections will provide a thorough examination of explicit and semi-implicit methods.

2.3 Explicit method

In a typical electromagnetic explicit PIC algorithm, Maxwell's and motion equations are solved in staggered order. The electromagnetic field is computed by

keeping the particle frozen. The fields are then updated in accordance with the currents and charges determined from the locations and velocities that were collected at the previous time interval [63].

The leap-frog algorithm is a popular method used in the explicit PIC method to discretise motion equations in time. In the leap-frog scheme a second-order accuracy scheme is used for time integration [57]. The charge-conserving current deposition algorithm firstly proposed by Villasenor and Buneman is used to ensure that the discretised charge conservation equation holds at any time if it is satisfied at $t = 0$ [64]. Using this scheme, the discretised relativistic motion equations read:

$$\mathbf{p}_p^{n+\frac{1}{2}} = \mathbf{p}_p^{n-\frac{1}{2}} + q_\alpha \Delta t \left[\mathbf{E}_p^n(\mathbf{x}_p^n) + \left(\frac{\mathbf{v}_p^{n+\frac{1}{2}} + \mathbf{v}_p^{n-\frac{1}{2}}}{2c} \right) \times \mathbf{B}_p^n(\mathbf{x}_p^n) \right], \tag{2.12}$$

$$\mathbf{x}_p^{n+1} = \mathbf{x}_p^n + \Delta t \frac{\mathbf{p}_p^{n+\frac{1}{2}}}{m_p \gamma_p}. \tag{2.13}$$

In this algorithm position and momentum are staggered by half-time interval: the momentum at time $n + 1/2$ is used to update the position from time interval n to $n + 1$. Similarly to this, the momentum is updated through quatitites computed at time n from time $n - 1/2$ to time $n + 1/2$ (see Fig. 2.1). In addition, the presence of $\mathbf{E}_p^n$ and $\mathbf{B}_p^n$ in the equations implies that the fields have been computed beforehand and are known before the implementation of the particle mover. This allows for the calculation of the momentum using the fields interpolated to the already determined particle position. Usually, two successive time levels are averaged, as in the example below:

$$\mathbf{B}_g^n = \frac{1}{2}(\mathbf{B}_g^{n+1/2} + \mathbf{B}_g^{n-1/2}). \tag{2.14}$$
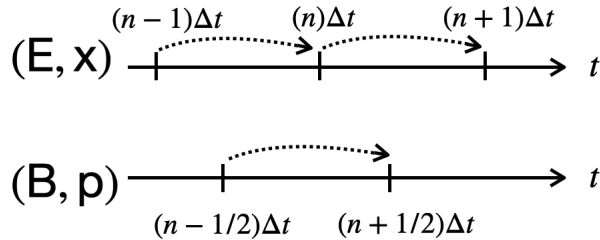
Figure 2.1: Visual representation of the leap-frog algorithm.

A possible discretisation method for Maxwell's equations based on the leap-frog
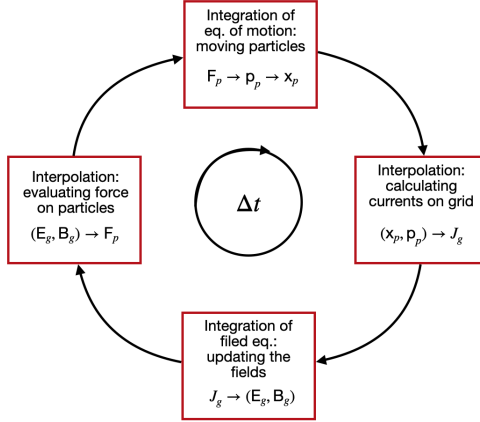
Figure 2.2: Time cycle of the explicit PIC algorithm. Particles are indicated with indexes $p = 1, 2, 3 \cdots N_p$ and grid cells with indexes g.

algorithm can be expressed as follows:

$$\nabla_g \times \mathbf{E}^n = -\frac{1}{c} \frac{\mathbf{B}_g^{n+1/2} - \mathbf{B}_g^{n-1/2}}{\Delta t}, \tag{2.15}$$

$$\nabla_g \times \mathbf{B}^{n+1/2} = \frac{1}{c} \frac{\mathbf{E}_g^{n+1} - \mathbf{E}_g^n}{\Delta t} + \frac{4\pi}{c} \mathbf{J}_g^{n+1/2}, \tag{2.16}$$

where notation ∇_g represents the application of the curl operator to calculate the field at a specific grid point g. According to Eq. (2.12), a conventional explicit PIC method requires the magnetic field at time n to compute the velocity at time $n + 1/2$. However, Eq. (2.15) provides the magnetic field at time $n + 1/2$ as Eq. 2.14.

Maxwell's equations are generally solved using the so-called finite difference time domain (FDTD) approach. In this method, the spatial discretisation of electromagnetic fields involves using a Yee grid, where the fields are discretised in a staggered manner in space [65]. In the Yee scheme, time is discretised using a second-order leap-frog scheme as given by Eqs. (2.15) and (2.16). In the Yee scheme for FDTD approach, the curl operators in the Faraday (Eq. (2.15)) and Ampere's (Eq. (2.16)) equations are spatially centred. It also ensures that the other two Maxwell's equations (Eq. (2.2) and Eq. (2.4)), which are not solved in typical explicit PIC codes, are automatically satisfied at any time if they hold at $t = 0$ and special care is taken to deposit the current density on the grid (for instance employing the Villasenor and Buneman's scheme).

The typical explicit PIC loop is shown in Fig. 2.2. Explicit PIC methods are the simplest and most straightforward type of PIC methods. In this method, particle positions and velocities are updated explicitly at each time step based on the electric and magnetic fields calculated at the previous time step. The explicit method is easy

to implement, computationally efficient and can be highly accurate for problems with smooth solutions or small time steps. However, this scheme introduces significant constraints due to the numerical discretisation of Maxwell's equations. The Courant-Friedrichs-Lewy (CFL) condition is a crucial stability criterion that must be satisfied in numerical simulations [66]. This condition places an upper limit on the time step to ensure that the simulation captures the propagation of signals at the speed of light c through grid cells accurately and stably. Mathematically, the CFL condition can be expressed as:

$$\Delta t < \frac{1}{c}\left(\sum_i \frac{1}{\Delta x_i^2}\right)^{-1/2}, \tag{2.17}$$

where Δt is the time step and Δx_i is the spatial resolution of the grid in the i-th direction. Equation (2.17) relates the time step to the spatial resolution on the grid and ensures that the simulation is numerically stable by preventing information from propagating faster than the grid resolution can resolve. However, even with this stability condition, certain numerical artefacts can still arise in PIC simulations. For instance, simulating ultra-relativistic particles can lead to the unphysical emission of Cherenkov-like radiation due to the numerical Cherenkov instability. This instability arises if $c\Delta t$ is too small compared to the grid resolution. In this case, the numerical phase velocity of electromagnetic waves has a dependency on the wavenumber and becomes less than c for high frequency small wavelength electromagnetic waves. Clearly this is a purely numerical artefact [67]. As a consequence particles can reach velocities higher than the numerical phase velocity of electromagnetic waves. This numerical effect is more pronounced for high frequency, small wavelength electromagnetic waves, leading to larger numerical errors.

Furthemore, the numerical solution may become unstable due to the particle mover discretisation when the following condition is not respected:

$$\omega_{\text{pe}}\Delta t < 2, \tag{2.18}$$

where $\omega_{\text{pe}} = \sqrt{4\pi n_e e^2/m_e}$ with n_e the electron number density, m_e the electron mass and e the elementary charge. The stability condition expressed by Eq. (2.18) can be obtained by performing a Von Neumann stability analysis of the numerical scheme used to solve the motion equations. The violation of the condition (2.18), i.e. when the time step is too large leads to the unphysical heating of particles, making the simulation results unreliable [68]–[70].

Finally, when a grid is used to solve field equations, a numerical instability called the finite grid instability could be triggered. This is due to the loss of information that occurs when continuous particle motion is approximated by projecting the particle onto grid points and integrating over control volumes to determine densities. This loss of information leads to aliasing errors, which can cause numerical instabilities in the

simulation [57], [71]. The problem of aliasing in the explicit PIC algorithm becomes severe when the spatial resolution, Δx, is much greater than the Debye length $\lambda_D = \sqrt{k_B T_e / 4\pi e^2 n_e}$ where k_B is the Boltzmann constant and T_e the electron temperature [57], [72], [73]. This instability, in turn, causes unphysical electron heating. The instability can be avoided in the case of linear interpolation by ensuring:

$$\Delta x < \lambda_D \pi. \tag{2.19}$$

The spatial resolution of explicit PIC simulations is severely limited by this constraint. As a consequence, when using explicit PIC, one is very often forced to over-resolved with respect to the physics of interest (the majority of electromagnetic processes in plasmas occur at scales that are orders of magnitude bigger than λ_D).

During the development of this thesis, the explicit PIC code OSIRIS [74], [75] has been employed to explore the propagation of ultra-relativistic beams into static plasmas (Chapter 4). OSIRIS is a massively parallel, fully relativistic and fully object-oriented PIC code. In order to advance the particles, the Boris pusher [76] has been used. The code is electromagnetic, so only Ampere's (Eq. (2.4)) and Faraday's (Eq. (2.5)) equations are used to advance the fields. The code implements a traditional finite difference time domain scheme leveraging the Yee discretisation. In recent years, it has been equipped also with a customised spectral solver, the so-called Fei algorithm [77], [78]. When using this algorithm, instead of being solved in real space, Maxwell's equations are solved in Fourier space. Thus the solver is numerically dispersionless, which means that it does not suffer from the numerical Cherenkov instability [77], [78]. As a consequence the solver is particularly useful when modelling ultra-relativistic particle beams as done for the study which will be presented in Chapter 4.

2.4   Fully implicit method

The numerical constraints typical of the explicit PIC algorithm pose limitations on the plasma spatial and temporal scales that can be modelled. These limitations are a consequence of the fact that particles are advanced using frozen fields and fields are computed using the current calculated freezing the particles [63]. A fully-implicit approach reintroduces the coupling between particles and fields typical of plasmas. According to this approach, an implicit discretisation in time for Maxwell's and motion equations is adopted. As a consequence, the severe stability constraints that affect the explicit implementation of the PIC algorithm are overcome. However, the implicit scheme requires the solution of a set of non-linearly coupled equations [63]. This obviously increases the mathematical cost of the algorithm and, since iterative methods must be adopted, could lead to convergence issues [79]. The semi-implicit PIC scheme represents a good compromise in this sense. It avoids the severe

constraints of the explicit PIC algorithm, but removes the complexity of the non-linear coupling and reduces the computational cost per time step of the fully implicit PIC algorithm [80].

2.5 Semi-implicit method: the Implicit Moment Method

The computational cost of the fully implicit PIC method has become manageable only in recent years thanks to the availability of larger and larger computational resources and the progress in the mathematical development of non-linear solvers. Thus, alternative approaches were developed mainly to simplify the non-linear coupling between fields and particles introduced by the fully implicit method, while still retaining the benefits of an implicit discretisation in time of the relevant equations [63]. As a result, what are called semi-implicit PIC techniques were formulated. The overarching idea behind the semi-implicit algorithm is to linearise the coupling between particles and fields, so to obtain a coupled linear system of equations instead of a full non-linear system. This concept has been introduced in both the Implicit Moment Method [81] and the direct implicit method [82] with some variations. Essentially, in these algorithms, the plasma response to the field changes over a time step that goes into Maxwell's equations is approximated. The rest of this section is dedicated to describe the Implicit Moment Method and the non-relativistic PIC code iPIC3D [79], predecessor of the code ECsim [80], [83]–[85] used to perform the studies presented in Chapter 3.

The Implicit Moment Method implements non-relativistic discretised equations of motion, which are expressed as follows [79]:

$$\mathbf{x}_p^{n+1} = \mathbf{x}_p^n + \Delta t \bar{\mathbf{v}}_p, \tag{2.20}$$

$$\mathbf{v}_p^{n+1} = \mathbf{v}_p^n + \frac{q_p}{m_p} \Delta t \left[\mathbf{E}_p^{n+\theta}(\bar{\mathbf{x}}_p) + \frac{\bar{\mathbf{v}}_p \times \mathbf{B}_p^n(\bar{\mathbf{x}}_p)}{c} \right], \tag{2.21}$$

where all quantities evaluated at $n + \theta$ are computed using the equation $\xi^{n+\theta} = \theta \xi^{n+1} + (1 - \theta)\xi^n$, where $\theta = 0$ implies an explicit scheme, and $\theta = 1$ implies a fully implicit scheme [63]. The quantities denoted with an overbar as $\bar{\mathbf{v}}_p$ and $\bar{\mathbf{x}}_p$, represent an average between the time steps n and $n + 1$.

By employing the θ-scheme, the discretised Faraday and Ampere's equations

become:

$$\nabla_g \times \mathbf{E}^{n+\theta} = -\frac{1}{c}\frac{\mathbf{B}_g^{n+1} - \mathbf{B}_g^n}{\Delta t}, \tag{2.22}$$

$$\nabla_g \times \mathbf{B}^{n+\theta} = \frac{1}{c}\frac{\mathbf{E}_g^{n+1} - \mathbf{E}_g^n}{\Delta t} + \frac{4\pi}{c}\mathbf{J}_g^{n+\theta}. \tag{2.23}$$

Equations (2.22) and (2.23) are combined to obtain the following equation for $\mathbf{E}^{n+\theta}$:

$$\mathbf{E}^{n+\theta} = \mathbf{E}_g^n + c\theta\Delta t\left(\nabla \times \mathbf{B}_g^n - \frac{4\pi}{c}\mathbf{J}_g^{n+\theta}\right) - (c\theta\Delta t)^2 4\pi\nabla\rho_g^{n+\theta}, \tag{2.24}$$

where the charge density ρ_g and current density $\mathbf{J}_g$ need to be evaluated at $n+\theta$. These quantities, for each species α, are found via a Taylor expansion of the interpolation function used to transfer information between the grid and particles and read:

$$\rho_{\alpha g}^{n+\theta} = \rho_{\alpha g}^n - \theta\Delta t\sum_p q_p\bar{\mathbf{v}}_p\nabla W(\mathbf{x}_g - \mathbf{x}_p^n) = \rho_{\alpha g}^n - \theta\Delta t\nabla \cdot \sum_p q_p\bar{\mathbf{v}}_p W(\mathbf{x}_g - \mathbf{x}_p^n), \tag{2.25}$$

$$\mathbf{J}_{\alpha g}^{n+\theta} = \hat{\mathbf{J}}_{\alpha g} - \frac{\Delta t}{2}\mu_{\alpha g} \cdot E_\theta - \frac{\Delta t}{2}\nabla \cdot \hat{\Pi}_{\alpha g}, \tag{2.26}$$

the current and the pressure tensor are defined respectively as:

$$\hat{\mathbf{J}}_{\alpha g} = \sum_p q_p\hat{\mathbf{v}}_p W(\mathbf{x}_g - \mathbf{x}_p^n), \tag{2.27}$$

$$\hat{\Pi}_{\alpha g} = \sum_p q_p\hat{\mathbf{v}}_p\hat{\mathbf{v}}_p W(\mathbf{x}_g - \mathbf{x}_p^n). \tag{2.28}$$

The current for each species is thus defined as:

$$\mathbf{J}_{\alpha g}^{n+\theta} = \hat{\mathbf{J}}_{\alpha g} - \theta\Delta t\nabla \cdot \sum_p q_p\hat{\mathbf{v}}_p\hat{\mathbf{v}}_p W(\mathbf{x}_g - \mathbf{x}_p^n) + \frac{\mu_{\alpha g} \cdot \mathbf{E}^{n+\theta}}{4\pi\theta\Delta t}, \tag{2.29}$$

where $\hat{\mathbf{v}}_p = \beta_p^n\mathbf{v}_p^n$ provides the velocity rotated by the magnetic field through the matrix β_p^n defined as:

$$\beta_p^n = \frac{1}{1 + (\Phi_\alpha|\mathbf{B}_p^n|)^2}\left[\mathbf{I} + \Phi_\alpha\mathbf{I} \times \frac{\mathbf{B}_p^n}{c} + \Phi_\alpha^2\frac{\mathbf{B}_p^n\mathbf{B}_p^n}{c^2}\right], \tag{2.30}$$

with $\Phi_\alpha = q_p\Delta t/2m_p$ [63]. The dielectric tensor $\mu_{\alpha g}$ in Eq. (2.25) describes the impact of the electric field on the plasma density and current [63] and reads:

$$\mu_{\alpha g}^n = 4\pi\theta\Delta t\rho^n\sum_p \beta_p^n. \tag{2.31}$$

The Taylor expansion used to express $\rho^{n+\theta}$ and $\mathbf{J}^{n+\theta}$ leads to moment equations, which provide a linear approximation of the particle response to the fields [84]. As a result, the temporal cycle is similar to that implemented in an explicit PIC method, albeit more complex [84] (see Fig. 2.3).
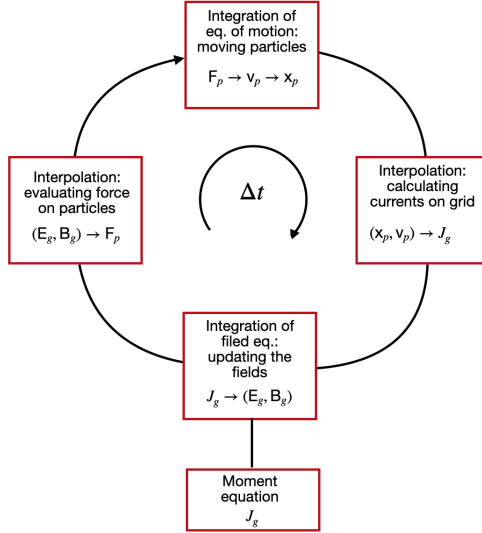
Figure 2.3: Diagram of the time cycle in a semi-implicit PIC technique. Through the linearisation of moment equations, the current is estimated outside the loop. The current may be roughly calculated in this way without moving the particles.

2.6 Energy Conserving Semi-Implicit Method

As a consequence of the linearisation introduced into Maxwell's equations to simplify the particle response to the fields, the Implicit Moment Method does not conserve energy. This usually leads to an artificial numerical cooling of the plasma that needs to be carefully monitored and assessed during simulations. In practice, the way to reduce the impact of the numerical cooling translates into choosing spatial and temporal steps sufficiently small with negative impact on the modelling of multiscale problems [84].

The Energy Conserving Semi-Implicit Method, in short ECsim, was introduced to remedy this issue.

In ECsim a new particle mover is used. According to this mover, the position of the particles is advanced as in the DIM D1 [86] scheme, while their velocity according

to the θ-scheme [81]:

$$\mathbf{x}_p^{n+1/2} = \mathbf{x}_p^{n-1/2} + \Delta t \mathbf{v}_p^n, \tag{2.32}$$

$$\mathbf{v}_p^{n+1} = \mathbf{v}_p^n + \frac{q_p}{m_p}\Delta t \left[\mathbf{E}_p^{n+\theta}(\mathbf{x}_p^{n+1/2}) + \frac{\bar{\mathbf{v}}_p \times \mathbf{B}_p^n(\mathbf{x}_p^{n+1/2})}{c} \right], \tag{2.33}$$

where electric and magnetic fields at the position $\mathbf{x}_p^{n+1/2}$ are known. The term $\bar{\mathbf{v}}_p = (\mathbf{v}_p^{n+1} + \mathbf{v}_p^n/2)$ is the averaged particle velocity. If one rewrites the velocity $\bar{\mathbf{v}}_p$ that appears in Eq.(2.33) as:

$$\bar{\mathbf{v}}_p = \hat{\mathbf{v}}_p + \Phi_\alpha \hat{\mathbf{E}}_p, \tag{2.34}$$

where the hatted quantities have been rotated with the rotation matrix β_p^n provided by Eq. (2.30) (e.g. $\hat{\mathbf{E}}_p = \beta_p^n \mathbf{E}_p^n$ and $\hat{\mathbf{v}}_p = \beta_p^n \mathbf{v}_p^{n+\theta}$) then the source term $\mathbf{J}_g^{n+1/2} = \bar{\mathbf{J}}_g = \sum_\alpha \bar{\mathbf{J}}_{g\alpha}$ in Eq. (2.23) is readily found as:

$$\bar{\mathbf{J}}_{\alpha g} = \frac{1}{V_g}\sum_p q_p \bar{\mathbf{v}}_p W(\mathbf{x}_p^{n+1/2} - \mathbf{x}_g) = \hat{\mathbf{J}}_{\alpha g} + \frac{\Phi_\alpha}{V_g}\sum_p q_p \beta_p^n \mathbf{E}_p^{n+\theta} W_{pg}. \tag{2.35}$$

Here, $\hat{\mathbf{J}}_{\alpha g} = \frac{1}{V_g}\sum_p q_p \hat{\mathbf{v}}_p W_{pg}$ and $W_{pg} = W(\mathbf{x}_p^{n+1/2} - \mathbf{x}_g)$. The current term is normalized to the cell volume V_g. Expressing $\mathbf{E}_p^{n+\theta}$ as a function of the electric field evaluated on the grid, Eq. (2.35) becomes:

$$\bar{\mathbf{J}}_{\alpha g} = \hat{\mathbf{J}}_{\alpha g} + \frac{\Phi_\alpha}{V_g}\sum_{g'}\left(\sum_p q_p \beta_p^n W_{pg} W_{pg'}\right)\mathbf{E}_{g'}^{n+\theta} = \hat{\mathbf{J}}_{\alpha g} + \frac{\Phi_\alpha}{V_g}\sum_{g'} M_{\alpha,gg'}^{ik} \mathbf{E}_{g'}^{n+\theta}, \tag{2.36}$$

where the mass matrices definition $M_{\alpha,gg'}^{ik} = \sum_p q_p \beta_p^{ik,n} W_{pg} W_{pg'}$ [87] has been introduced. Note that here, the subscript g refers to the index of the cell where the mass matrix is computed, g' refers to the index of the cell where the particle is located. The indexes i and k stand for the Cartesian vector components e.g. $i, k = 1, 2, 3$. For each grid node, there are 27 mass matrices in 3D. However, due to symmetry only 14 mass matrices are computed at each time step [80].

The new mover (Eqs. (2.32) and (2.33)) and the exact formulation for the current density that can be derived with it (Eq. (2.36)) have the striking consequence to ensure perfect energy conservation in the code [83]. Thus, the artificial cooling typical of the Implicit Moment Method is avoided. This means that spatial and temporal resolutions of simulations can be chosen only based on the physics of interest, hence allowing for modelling multiscale plasma problems at a limited computational cost with respect to fully implicit methods.

Chapter 3

The current filamentation instability on ion time scales

3.1 Introduction

This chapter focuses on studying the growth of the CFI in non-relativistic electron-ion plasma flows that are counterstreaming.

The CFI arises from an infinitesimal magnetic field perturbation, leading to the formation of current filaments that amplify the magnetic field. While the linear phase of the instability has been extensively studied (see [88] and references therein), the long-term evolution of the fields on ion time scales and the mechanism behind the instability saturation remain largely unexplored.

This study utilises a kinetic approach to provide a statistical description of the plasma and investigates the non-linear dynamics of the CFI using two-dimensional kinetic simulations. The results of this work highlight the transition from an electron-driven phase to an ion-driven phase and examine the merging of current filaments and the mechanism of instability saturation. Understanding the non-linear phase of the instability and the evolution of fields on large spatial and long temporal scales is essential to gain deeper insight into astrophysical and laboratory processes, such as shock formation.

In the following chapter, the statistical description of purely transverse electromagnetic waves in plasma was employed to derive the CFI dispersion relation. Two-dimensional kinetic simulations were then conducted using the ECsim code to investigate the non-linear dynamics of the instability on ion time scales for hundreds of ion plasma periods. The main PIC simulation results were analysed, with a focus on the shift from the electron-driven phase to the ion-driven phase. A detailed study was conducted on the current filaments generated by the instability, including an analysis of their merging trend. The merging rate deduced from the study, along with

the analysed instability saturation mechanism, contributes to a better understanding of the system dynamics.

3.2 Derivation of the analytical dispersion relation

In the current section, the analytical description of the linear phase of the purely transverse ion CFI is presented. This can be studied by linearising the Vlasov equation (Eq. (2.1)) and Faraday and Ampere's equations (Eqs. (2.4) and (2.5)). Physical quantities, which are dependent on space and time, can be expressed in the following form:

$$\Phi(\mathbf{x}, t) = \Phi_0 + \Phi_1 \exp\left(i\mathbf{k} \cdot \mathbf{x} - \omega t\right), \tag{3.1}$$

where 0 and 1 identify the equilibrium and perturbative states, respectively and $|\Phi_1| \ll |\Phi_0|$ as required by the perturbative approach. By introducing Eq. (3.1) into Eq. (2.1) and neglecting higher order terms, an expression for the perturbed distribution function for the species α is obtained:

$$f_{\alpha 1} = \frac{q_\alpha}{m_\alpha} \frac{\left(\mathbf{E}_1 + \frac{\mathbf{v}}{c} \times \mathbf{B}_1\right) \cdot \frac{\partial f_{\alpha 0}}{\partial v}}{i(\omega - \mathbf{k} \cdot \mathbf{v})}. \tag{3.2}$$

Using the same technique, the linearised Faraday and Ampere's Eqs. (2.4) and (2.5) are obtained:

$$i\mathbf{k} \times \mathbf{E}_1 = \frac{1}{c} i\omega \mathbf{B}_1, \tag{3.3}$$

$$i\mathbf{k} \times \mathbf{B}_1 = \frac{4\pi}{c} \mathbf{J}_1 - \frac{i}{c} \omega \mathbf{E}_1. \tag{3.4}$$

Combining Eqs. (3.3) and (3.4) leads to:

$$[\mathbf{k} \times (\mathbf{k} \times \mathbf{E}_1)] + \frac{4\pi}{c^2} i\omega \mathbf{J}_1 + \frac{\omega^2}{c^2} \mathbf{E}_1 = 0, \tag{3.5}$$

where the first order perturbation of the current density reads:

$$\mathbf{J}_1 = \sum_\alpha q_\alpha n_\alpha \int d^3\mathbf{v}\mathbf{v} f_{\alpha 1} = \sigma \cdot \mathbf{E}_1. \tag{3.6}$$

Here, σ is the conductivity tensor and its components are given by:

$$\sigma_{ij} = -i \sum_\alpha \frac{n_\alpha q_\alpha^2}{m_\alpha} \int_{-\infty}^{\infty} d^3\mathbf{v} \frac{v_i}{(\omega - \mathbf{k} \cdot \mathbf{v})} \left[\left(1 - \frac{\mathbf{v} \cdot \mathbf{k}}{\omega}\right) \frac{\partial f_{\alpha 0}}{\partial v_j} + \left(\frac{\mathbf{k}}{\omega} \cdot \frac{\partial f_{\alpha 0}}{\partial \mathbf{v}}\right) v_j\right]. \tag{3.7}$$

By utilising the $(\mathbf{A} \times (\mathbf{B} \times \mathbf{C})) = (\mathbf{A} \cdot \mathbf{C})\mathbf{B} - (\mathbf{A} \cdot \mathbf{B})\mathbf{C}$ identity vector the first term on the left-hand side of Eq. (3.5) can be written as:

$$[\mathbf{k} \times (\mathbf{k} \times \mathbf{E}_1)] = (\mathbf{k} \cdot \mathbf{E}_1)\mathbf{k} - k^2\mathbf{E}_1. \tag{3.8}$$

Introducing Eq. (3.6) to express $\mathbf{J}_1$ and Eq. (3.8) into Eq. (3.6), the following is obtained:

$$(\mathbf{k} \cdot \mathbf{E}_1)\,\mathbf{k} - k^2\mathbf{E}_1 + \frac{4\pi}{c^2}i\omega\sigma \cdot \mathbf{E}_1 + \frac{\omega^2}{c^2}\mathbf{E}_1 = 0, \tag{3.9}$$

whose generic i^{th} component reads:

$$\left(\sum_j k_j E_{j1}\right)k_i - k^2E_{i1} + \frac{4\pi}{c^2}i\omega\sum_j \sigma_{ij}E_{j1} + \frac{\omega^2}{c^2}E_{i1} = 0. \tag{3.10}$$

Equation (3.10) can be rewritten as:

$$\sum_j \left(k_ik_j - k^2\delta_{ij} + \frac{\omega^2}{c^2}\delta_{ij} + \frac{4\pi}{c^2}i\omega\sigma_{ij}\right)E_{j1} = \sum_j \Lambda_{ij}E_{j1} = 0. \tag{3.11}$$

Equation (3.11) represents a system of 3 equations (one for each $i = 1, 2, 3$ cartesian component). A non-trivial solution can be found only for:

$$\det(\Lambda_{ij}) = 0. \tag{3.12}$$

In order to solve Eq. (3.12), it is useful to reformulate the expression for Λ_{ij} in terms of the dielectric tensor ε_{ij}:

$$\Lambda_{ij} = k_ik_j - k^2\delta_{ij} + \frac{\omega^2}{c^2}\varepsilon_{ij}, \tag{3.13}$$

where $\varepsilon_{ij} = \delta_{ij} + \frac{4\pi i}{\omega}\sigma_{ij}$, or:

$$\varepsilon_{ij} = \delta_{ij} + \sum_\alpha \frac{\omega_{p\alpha}^2}{\omega}\int_{-\infty}^{\infty} d^3\mathbf{v}\frac{v_i}{(\omega - \mathbf{k} \cdot \mathbf{v})}\left[\left(1 - \frac{\mathbf{v} \cdot \mathbf{k}}{\omega}\right)\frac{\partial f_{\alpha 0}}{\partial v_j} + \left(\frac{\mathbf{k}}{\omega} \cdot \frac{\partial f_{\alpha 0}}{\partial \mathbf{v}}\right)v_j\right]. \tag{3.14}$$

The solution of Eq.(3.12) provides the dispersion relation of all the waves allowed in the system. Assuming real wavenumber k, the frequency ω could be complex: $\omega = \omega_R + i\Gamma$. In this case, $\Gamma < 0$, would correspond to an exponentially damped solution, while $\Gamma > 0$ would give an exponentially growing mode, i.e. an instability.

3.3   Weibel or Current Filamentation Instability

The Weibel instability [10] is a purely growing electromagnetic mode. The initial condition to trigger the Weibel instability can be produced by a strong temperature anisotropy (the scenario originally envisioned by [10]) or by counterstreaming flows. In this latter case, the instability is also known as CFI. The instability transfers energy from the particles to the magnetic field. Additionally, during this energy transfer process, the particle distribution function, which describes how particles are distributed in velocity space within the plasma, becomes more isotropic.

The physical picture of the Weibel instability in the presence of counterstreaming electron beams in plasmas was given by B. D. Fried [11]. To understand the physical mechanism of the Weibel instability, it is useful to consider a system with fixed ions and counterstreaming electrons moving parallel and anti-parallel to the x axis (see Fig. 3.1). Initially, no net currents are present because the electrons streaming in different directions are equally distributed in space. In the presence of a small perturbation of the magnetic field of the form $\mathbf{B} = \hat{\mathbf{z}} B_z \cos(k_y y)$, arising from noise, the electrons moving rightwards are pushed into layer I, while those moving leftwards are pushed into layer II. The magnetic field deflects electrons thus creating micro-currents. These micro-currents in turn increase the initial magnetic fluctuation. In the presence of two non-relativistic electron flows this field grows with a rate $\Gamma = \omega_p v_e / c$ where v_e is the electron bulk speed [3].

The Weibel instability is thought to be significant in a variety of astrophysical plasmas, including galactic cosmic settings, SNRs, and GRBs sources, where it is considered the source of the intense magnetic fields necessary to explain the level of observed radiation [1], [3], [9].

3.4   Linear phase of the ion Weibel instability

In the following section, the CFI dispersion relation is obtained for symmetric counterstreaming electron and ion flows that interact along the x direction. Both electrons and ions can be described at equilibrium using a drifting Maxwellian distribution:

$$f_{\alpha 0} = \frac{m_\alpha}{2\pi \sqrt{T_{\alpha,x} T_{\alpha,y}}} \exp\left(-\frac{m_\alpha (v_x - v_\alpha)^2}{2 T_{\alpha,x}} - \frac{m_\alpha v_y^2}{2 T_{\alpha,y}} \right), \qquad (3.15)$$

where the subscript $\alpha = e, i$ has been used to indicate electrons (e) and ions (i), respectively. In Eq. (3.15), v_α represents the drift velocity and $T_{\alpha,x}$ and $T_{\alpha,y}$ the temperature in the longitudinal and in-plane transverse direction, respectively. These temperatures are expressed in energy units. A case $T_{\alpha,y} = T_{\alpha,x}$ and $T_e = T_i$ was
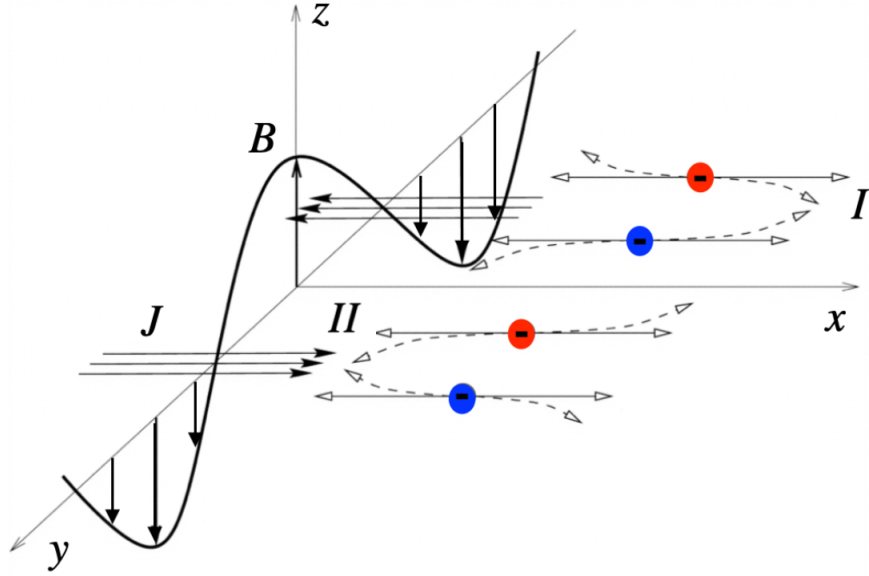
Figure 3.1: Physical picture of Weibel-like instabilities (Weibel instability and CFI). The direction of streaming (for the filamentation instability) or greater thermal velocities (for the Weibel Instability) is x. The red electrons experience negative magnetic field fluctuations, the blue electrons positive magnetic field fuctuations. The resulting motion is marked by the dashed arrows, the areas of particle clustering are indicated as I and II. Adapted from [3].

considered. The counterstreaming plasmas have initial density $n_e = n_i = n_0/2$ and drift velocity $\mathbf{v}_e = \mathbf{v}_i = \pm v\hat{\mathbf{x}}$.

Considering the distribution function expressed by Eq. (3.15) and transverse modes only (e.g. $\mathbf{k} = (0, k_y, 0)$), Eq. (3.12) becomes:

$$\omega^2 \varepsilon_{xx} - k_y^2 c^2 = 0, \tag{3.16}$$

with ε_{xx} given by:

$$\varepsilon_{xx}(k_y, \omega) = 1 + \sum_{\alpha} \frac{\omega_{p\alpha}^2}{\omega} \int d^3\mathbf{v} \left(\frac{v_x}{\omega - k_y v_y} \right) \left[\left(1 - \frac{k_y v_y}{\omega} \right) \frac{\partial f_{\alpha 0}}{\partial v_x} + \frac{k_y v_x}{\omega} \frac{\partial f_{\alpha 0}}{\partial v_y} \right]. \tag{3.17}$$

Using the distribution function Eq. (3.15), then Eq. (3.17) becomes:

$$\varepsilon_{xx}(k_y, \omega) = 1 + \sum_{\alpha} \frac{\omega_{p\alpha}^2}{\omega^2} \left[-1 + Z(\xi_\alpha) \frac{T_{\alpha,x}}{T_{\alpha,y}} + \frac{m_\alpha}{T_{\alpha,y}} v_\alpha^2 Z(\xi_\alpha) \right], \tag{3.18}$$

where the plasma dispersion function $Z(\xi)$ [89] defined as

$$Z(\xi) = \frac{1}{\sqrt{\pi}} \int_0^{\infty} \frac{e^{-x^2}}{x - \xi} dx \qquad (3.19)$$

has been introduced. Considering only purely growing modes ($\omega = i\Gamma$, $\Gamma > 0$), then Eq.(3.16) can be written as [90]:

$$\Gamma^2 + c^2 k_y^2 + \sum_{\alpha} \omega_{p\alpha}^2 - \sum_{\alpha} \omega_{p\alpha}^2 (a_\alpha + 1) \Re \left[1 + \xi_\alpha Z(\xi_\alpha) \right] = 0, \qquad (3.20)$$

where $\xi_\alpha = i \frac{\Gamma}{k_y} \sqrt{\frac{m_\alpha}{2 T_{\alpha,y}}}$, $\Re$ identifies the real part and a_α denotes the anisotropy ratio defined as:

$$a_\alpha = \frac{m_\alpha v_\alpha^2 + T_{\alpha,x}}{T_{\alpha,y}} - 1. \qquad (3.21)$$

By solving Eq. (3.20), the growth rate of the CFI can be found as a function of the wavenumber k.

3.5   Comparison between simulations and linear theory

Here, a comparison will be made between the outcomes of linear theory and the simulation results of the CFI. This step is crucial to validate the numerical code ECsim which will be used for exploring the non-linear evolution of the CFI.

The theoretical dispersion relation Eq. (3.20) is numerically solved to find Γ vs k. This is done by using the in-built Mathematica function FindRoot [91]. In order to compute the growth rate of the purely ionic CFI, electrons will be considered fully isotropic.

The first step to solve Eq. (3.20) with Mathematica consists of expressing the plasma dispersion function (Eq. (3.19)) in terms of the Dawson function:

$$\text{Dawson}(\xi) = e^{-\xi^2} \int_0^{\xi} e^{t^2} dt. \qquad (3.22)$$

By using Eq. (3.22), Eq. (3.19) can be written as:

$$Z(\xi) = i\sqrt{\pi} e^{-\xi^2} - 2\text{Dawson}(\xi), \qquad (3.23)$$

and the dispersion relation for the CFI (Eq. (3.20)) becomes:

$$\hat{k}_y^2 + \hat{\Gamma}^2 + 1 - (\hat{a}_e + 1)\Re(1 + \hat{\xi}_e Z(\hat{\xi}_e)) + \frac{m_e}{m_i} - \frac{m_e}{m_i}(\hat{a}_i + 1)\Re(1 + \hat{\xi}_i Z(\hat{\xi}_i)) = 0. \quad (3.24)$$

Here, hatted quantities identify normalised variables according to:

$$\hat{\Gamma} = \frac{\Gamma}{\omega_{\text{pi}}}, \qquad \hat{k}_y = \frac{k_y c}{\omega_{\text{pi}}}, \qquad \hat{T}_\alpha = \frac{T_\alpha}{m_e c^2}, \qquad \hat{v}_\alpha = \frac{v_\alpha}{c}, \tag{3.25}$$

$$\hat{a}_i = \frac{(m_i/m_e)\hat{v}_i^2 + \hat{T}_{i,x}}{\hat{T}_{i,y}} - 1, \qquad \hat{a}_e = \frac{\hat{v}_e^2 + \hat{T}_{e,x}}{\hat{T}_{e,y}} - 1, \tag{3.26}$$

and

$$\hat{\xi}_i = i\sqrt{\frac{(m_i/m_e)}{2\hat{T}_{i,y}}}\frac{\hat{\Gamma}}{\hat{k}_y}, \qquad \hat{\xi}_e = i\sqrt{\frac{1}{2T_{e,y}}}\frac{\hat{\Gamma}}{\hat{k}_y}. \tag{3.27}$$

As a first step, the growth rate provided by the solution of Eq. (3.24) has been compared with the results of a two-dimensional (2D) simulation.

In this simulation, two counterstreaming plasmas composed of electrons and ions with mass ratio $m_i/m_e = 100$ have been initialised. At this stage, singly charged ions are employed, with a reduced mass ratio to alleviate the computational cost. All species are distributed according to a drifting Maxwellian with temperature $T_{e,xy} = T_{i,xy} = 0.01\,m_e c^2$ and drift velocity $v_e = v_i = \pm 0.2\,c$. After taking these latter parameters into account, the resulting anisotropies are $a_i = 401$ and $a_e = 4$ (see Eq. (3.27)). The temperature and velocity of the particles under consideration cause the high value of ion anisotropy. A high value of ion anisotropy is needed to drive the current filamentation instability significantly. The large anisotropy ensures that the instability can be triggered and grow rapidly, affecting the plasma dynamics. The longitudinal and transverse sizes of the 2D simulation box was choosen to be $L_x = L_y = 10.44\,d_i$, where $d_i = c/\omega_{\text{pi}}$ is the ion skin depth. The box has been discretised with $N_x = N_y = 1044$ cells for a resolution of $\Delta x = \Delta y = \lambda_D = 0.01\,d_i = 0.1\,d_e$, where $d_e = c/\omega_{\text{pe}}$ is the electron skin depth. A time resolution $\Delta t = 0.0069\,\omega_{\text{pi}}^{-1}$ has been adopted and the simulation has run up to $t_{\text{end}} = 59.43\,\omega_{\text{pi}}^{-1} = 5943\,\omega_{\text{pe}}^{-1}$. In this simulation 100 particles-per-cell per species were employed. Periodic boundary conditions have been used for fields and particles in both directions. It could be observed that there might be an excessive level of detail in this simulation, and that ECsim may not require such fine resolution of quantities [83], [84]. This observation relates to the computational resolution of space and time, pointing out that the ECsim scheme doesn't exhibit the same strict correlation between quantities as an explicit system does. Consequently, it is possible to remodel the values to reduce the computational cost while preserving the underlying physics.

In the simulation, the instability develops starting from the numerical noise due to the granularity of the particles. As a result of the instability, the magnetic field grows along the out-of-plane transverse direction z. Since the instability has not been seeded, all the modes that the simulation box can accommodate are allowed to grow. Indeed a variety of waves is observed to grow on different timescales.
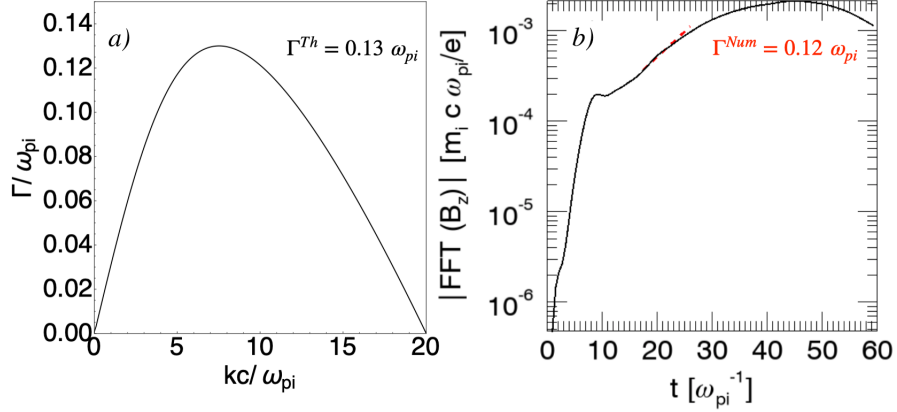
Figure 3.2: Theoretical growth rate of the instability (computed solving numerically Eq. (3.24)) as a function of the wavenumber for the following plasma parameters $m_i/m_e = 100$, $T_{i,xy} = 0.01\, m_e c^2$, $v_i = \pm 0.2\, c$, $a_i = 401$ and $a_e = 0$. The theoretical maximum growth rate $\Gamma^{\mathrm{Th}} = 0.13\, \omega_{\mathrm{pi}}$ occurs for $k = 7.50\, d_i^{-1}$ (a). Evolution in time of the Fourier transform of B_z for $k = 7.50\, d_i^{-1}$ (b). The red dashed line corresponds to the numerical growth rate $\Gamma^{Num} = 0.12\, \omega_{\mathrm{pi}}$.

The theoretical growth rate resulting from the dispersion relation (Eq. (3.24)) is shown in Fig. 3.2 (a). The maximum growth rate $\Gamma = 0.13\, \omega_{\mathrm{pi}}$ is associated to a wavenumber $k = 7.50\, d_i^{-1}$ and wavelength $\lambda = \frac{2\pi}{k} = 0.838\, d_i$. This means that the simulation box is large enough to roughly contain 13 wavelengths of the fastest growing mode. The time evolution of the Fourier transform of B_z as provided from the numerical simulation is reported in Fig. 3.2 (b). The mode with $k = 7.50\, d_i^{-1}$, corresponding to the fastest growing mode indicated by linear theory has been selected. In the simulation, the magnetic field develops on electron-time scales first, then on ion-time scales. By analysing the slope of the curve in Fig. 3.2 (b), it was determined that the numerical growth rate, $\Gamma^{\mathrm{Num}} = 0.13\, \omega_{\mathrm{pi}}$, is in excellent agreement with the theoretical value of $\Gamma^{\mathrm{Th}} = 0.12\, \omega_{\mathrm{pi}}$. Thus this test confirms that ECsim can appropriately model the CFI.

3.6   Convergence study

Before performing larger simulations, it was essential to determine the appropriate numerical resolution in order to balance computational costs and ensure accurate results. The convergence study was crucial to determine the appropriate computational parameters for investigating the non-linear phase of the CFI on ion time scales. The focus of this study was on spatial scale, temporal resolution, and particles-per-cell

settings.

The convergence study employed the same simulation setup considered in Section 3.5. In each simulation numerical parameters have been varied to understand their impact on the numerical results and verify that coarser resolutions still provide meaningful physical results. To ascertain this last point, the temporal evolution of the transverse magnetic field energy density $\varepsilon_{B_z} = \int B_z^2 dV/8\pi$ of all k wavenumber spectrum. The magnetic field topology at saturation time resulting from different runs were compared.

Spatial resolution

The effect of the spatial resolution was analysed by gradually increasing Δx and Δy. A coarser resolution allows for decreasing the number of cells used to discretised the simulation domain with the advantage of decreasing the computational cost of the simulation.

In all simulations the instability grows from numerical noise. Since the noise depends on the total number of particles N with a proportionality of $\frac{1}{\sqrt{N}}$, for this study on the impact of the spatial resolution, the total number of particles in the simulation has been kept constant. This means that when larger values of Δx and Δy were selected the number of particles-per-cell was increased. Increasing grid resolution significantly increases computational time because there are more grid cells to process. This effect is greater than simply increasing the number of particles. While doubling the number of particles doubles the time, increasing the grid resolution can increase the time by much more than double due to the higher complexity of calculations.

Figure 3.3 (a) reports the evolution in time of the B_z energy for different values of spatial resolution. The level of resolution has been gradually reduced. While the most detailed resolution ($\Delta x = \Delta y = 0.01\,d_i = 0.1\,d_e$) was enough to resolve λ_D, the coarsest resolution is $\Delta x = \Delta y = 12\lambda_D$. However, Fig. 3.3 (a) indicates that the growth rate of the instability both on electron time scales ($t \lesssim 10\,\omega_{\rm pi}^{-1}$) and ion time scales ($17\,\omega_{\rm pi}^{-1} \lesssim t \lesssim 38\,\omega_{\rm pi}^{-1}$) is well reproduced in all the cases analysed. Indeed the slope of the curves, which indicate the growth rate of the instability, is nearly the same for $t \gtrsim 10\,\omega_{\rm pi}^{-1}$ and for $17\,\omega_{\rm pi}^{-1} \lesssim t \lesssim 38\,\omega_{\rm pi}^{-1}$. Figure 3.3 (a) also reveals that the level of magnetic field at saturation is well reproduced by all the resolutions. Figures 3.3 (b) and (c) show the snapshots of the topology of the magnetic field B_z at saturation time for the highest ($\Delta x = \Delta y = 0.01\,d_i$) and lowest ($\Delta x = \Delta y = 0.12\,d_i$) spatial resolution, respectively. These plots also indicate that the field amplitude at saturation is equivalent for the smallest and largest cell size considered, thus confirming that a resolution in this range can still reproduce the physics of the non-linear phase of the CFI correctly.

By looking carefully at the evolution of energy and the field topology, it was
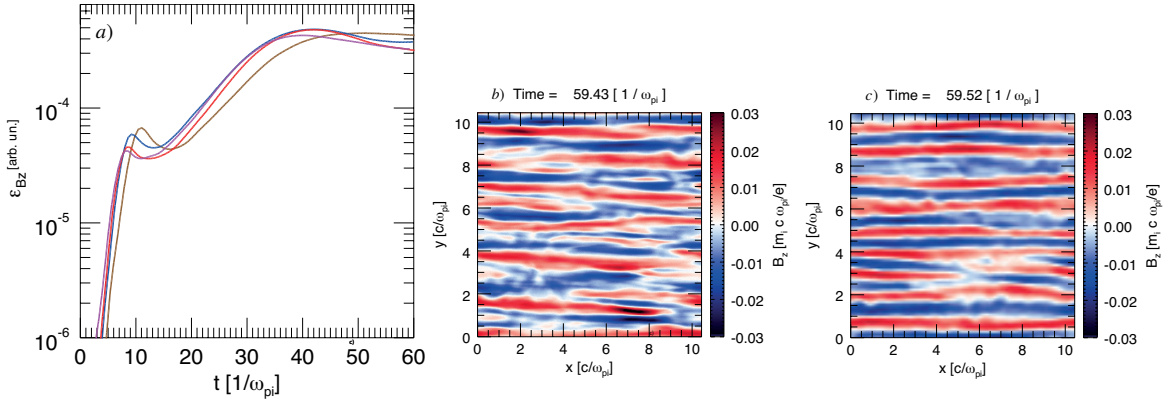
Figure 3.3: Evolution in time of the out-of-plane magnetic field energy for $\Delta x = \Delta y = 0.01$ (magenta), 0.04 (red), 0.08 (blue) and 0.12 (brown) d_i (a). Out-of-plane transverse magnetic field at saturation for $\Delta x = \Delta y = 0.01\,d_i$ (b) and $\Delta x = \Delta y = 0.12\,d_i$ (c).

decided that a spatial grid with $\Delta x = \Delta y = 0.06\,d_i$ (not shown in Fig. 3.3) provides the most accurate results. This resolution stands out as optimal because it lies midway between the resolutions of $0.01\,d_i$ and $0.12\,d_i$, where there is no significant difference in the physics observed. Additionally, it is computationally more efficient compared to $\Delta x = \Delta y = 0.01\,d_i$, considering that computational costs increase with system resolution. It is important to emphasize that $\Delta x = \Delta y = 0.06\,d_i$ correspond to $\Delta x = \Delta y = 6\,\lambda_D$. This largely exceeds the stability condition dictated by Eq. (2.19). Therefore, if such a resolution was to be used with an explicit algorithm, it would quickly leads to the development of numerical instabilities such as the finite grid instability.

Temporal resolution

Another parameter scan has been dedicated to identifying the best temporal resolution. For the analysis of Δt, the same plasma parameters as those illustrated in Section 3.5 were used. A box size of 10.44×10.44 d_i^2 with grid cell size $\Delta x = \Delta y = 0.06\,d_i$ as determined in the scan about the spatial resolution has been employed. The simulations explored the effect of increasingly larger time steps, with the aim of decreasing the number of temporal cycles required to attain saturation. In turn, a smaller number of temporal cycles allows for saving computing resources.

In the first simulation, a time step of $\Delta t = 0.06\,\omega_{\text{pi}}^{-1}$ was used, considering the CFL condition (2.17). It is well known that the semi-implicit approach utilised in ECsim allows for the relaxation of this constraint [83]. The goal of this part is to determine how far this may be pushed while still producing accurate findings.

Figure 3.4 (a) reports the evolution in time of the magnetic field energy B_z in the simulation box for progressively larger values of Δt. All the curves follow extremely similar trends in the linear and non-linear regimes when the magnetic field reaches the maximum value. Snapshots of the out-of-plane magnetic field at saturation ($t \approx 60\,\omega_{\text{pi}}^{-1}$) for various values of Δt are presented in Figs. 3.4 (b) and (c). Studying the filamentary structure of B_z at saturation time reveals a comparable intensity for all Δt. In virtue of this analysis, it has been decided that $\Delta t = 0.08\,\omega_{\text{pi}}^{-1}$ offered the best compromise in term of correctness of the simulation and its duration. Considering that future simulations will run for longer periods, the largest time step was not selected to prevent a significant increase in computational time. Notably, ECsim can accurately simulate the physics with a time step Δt that is 30% larger than the value required by the CFL condition (Eq. (2.17)). This is quite remarkable because when the CFL condition in not satisfied, in an explicit PIC simulation becomes quickly unstable. This means that when employing explicit PIC codes, one is restricted to selecting extremely small Δt, resulting in many more computational iterations and therefore raising the total cost of the simulation in terms of CPU time. While this is not a problem when studying electron physics, it becomes a significant issue when studying ion dynamics.
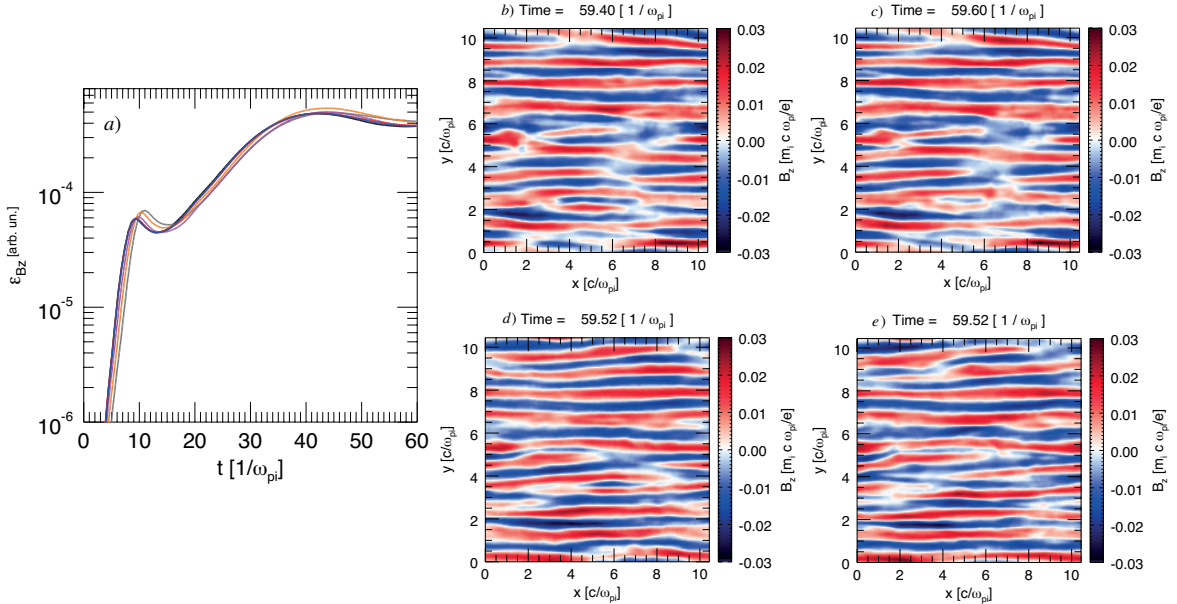

Figure 3.4: Same as Fig. 3.3 (a), but for $\Delta t = 0.04$ (black), 0.06 (blue), 0.08 (red), 0.16 (magenta), 0.24 (orange) and 0.32 (grey) ω_{pi}^{-1} (a). Same as Fig. 3.3 (b), but for $\Delta t = 0.06$ (b), 0.08 (c), 0.24 (d) and 0.32 (e) ω_{pi}^{-1}.

Particles-per-cell

The last parameter to be examined is the number of particles-per-cell.

The computational cost of a simulation strongly depends on the number of particles used. The number of operations to be performed increases with the number of particles. Furthermore, ECsim requires the generation and storage of mass matrices for each particle, thus further increasing the number of CPU hours and memory requirements whenever the number of particles-per-cell employed increases. As a result, it is crucial to keep the number of particles-per-cell as low as possible, but at the same time it is important to ensure that numerical results are physical and not concealed by numerical noise. This is particular relevant for ECsim, which employs only first order splines to interpolate particles to the grid.

In order to identify the lowest number of particles-per-cell, which still ensure consistent results, a series of simulations with a progressively increasing number of particles has been performed. In this parameter scan, grid size and temporal resolution were fixed to the best values identified in the previous convergence studies ($\Delta x = \Delta y = 0.06 \, d_i$ and $\Delta t = 0.08 \, \omega_{\mathrm{pi}}^{-1}$). The result of this set of simulations can be seen in Fig. 3.5 (a), which reports the evolution of the magnetic field energy for simulations employing a different number of particles-per-cell. The first thing to note is that the curves are very similar regardless of the number of particles-per-cell. In the ion phase of the instability ($13 \, \omega_{\mathrm{pi}}^{-1} \lesssim t \lesssim 31 \, \omega_{\mathrm{pi}}^{-1}$), the growth rate is approximately $\Gamma/\omega_{pi} = 0.121$ for 225 particles per cell and 0.119 for 3600 particles per cell. These values are very similar. When the number of particles per cell increases from 225 to 3600, the growth rate decreases by about 1.65%.

Although the reduction in particles-per-cell values does not have a significant impact on the total magnetic field energy, the same cannot be said for the features within the field. Indeed the transverse magnetic filed at saturation shows variation depending on the number of particles-per-cell, as shown in Figs. 3.5 (b) and (c). The most evident variation of the filamentary structure is evident in the 225 particles-per-cell case (Fig. 3.5 (b)), where the central negative field filament has become split and twisted, resulting in the weakening of the magnetic field in the centre of the simulation box. A particle-per-cell case of 3600 is considered the most suitable choice for simulating the ion CFI.

3.7 Non-linear phase of the ion current filamentation instability

This section focuses on the long-time non-linear evolution of the CFI on ion time scales. To explore the non-linear phase of the instability, simulations were performed using the same setup described in Section (3.5), but considering temperatures $T_e =$
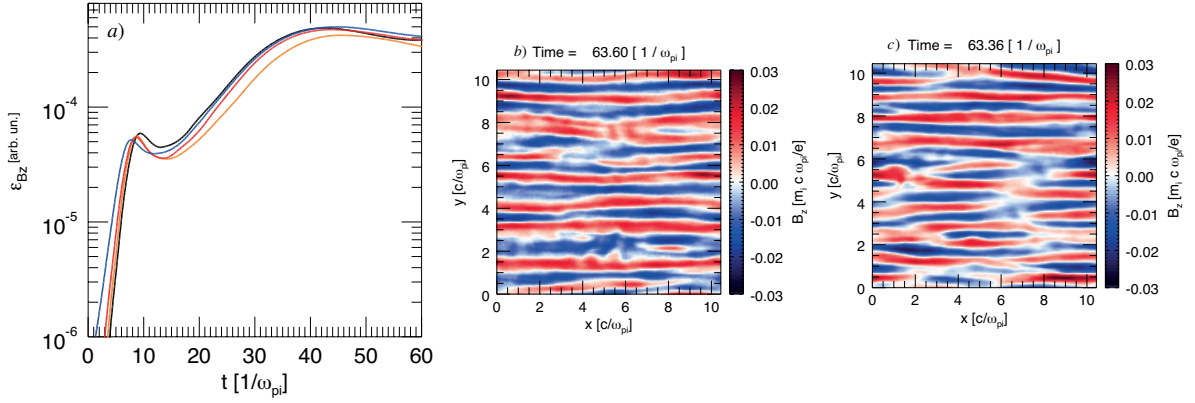
Figure 3.5: Same as Fig. 3.3, but for particles-per-cell 225 (blue), 900 (red), 2025 (brown) and 3600 (black) per species (a). Same as Fig. 3.3, but for 225 (b) and 3600 (c) particles-per-cell per species.

$T_i = 0.0025\,m_e c^2$, drift velocities $v = v_e = v_i$ in the range $[0.044 - 0.1]\,c$ and m_i/m_e in the range $[200 - 1000]$. The thermal velocities are given by $v_{\mathrm{th,e}} = \sqrt{T_e/m_e}$ for electrons and $v_{\mathrm{th,i}} = \sqrt{T_i/m_i}$ for ions. The typical simulation box had size $L_x = L_y = 26\,\lambda = 21.76\,d_i$ with the mesh size $\Delta x = \Delta y = 6\,\lambda_D = 0.06\,d_i$. The temporal step was $0.056\,\omega_{\mathrm{pi}}^{-1}$ and particles were pushed for more than 80000 iterations. Each cell contained 3600 macro-particles per species.

The results of a simulation with $m_i/m_e = 1000$ and $v = \pm 0.044\,c$ are shown first. The ion-to-electron mass ratio is sufficiently close to the real proton-to-electron mass ratio to allow for correctly observing scale separation effects. Figure 3.6 shows the temporal evolution of the normalised out-of-plane magnetic and longitudinal and transverse in-plane electric field energies in the CGS system $\varepsilon_B = \int B_z^2 dV/8\pi\varepsilon_k$ and $\varepsilon_E = \int E_{x,y}^2 dV/8\pi\varepsilon_k$ where ε_k represents the initial total kinetic energy in the system $(m_e + m_i)v^2 L_x L_y$.

This normalised quantity is known as an equipartition parameters and illustrates how much kinetic energy is converted into electromagnetic energy.

The magnetic field equipartition parameter clearly indicates that in the case of counterstreaming electrons and ions, the instability evolves according to three different phases. At first, the magnetic field energy has a very rapid growth until $\simeq 50\,\omega_{\mathrm{pi}}^{-1}$, mainly sustained by the electrons. Indeed, comparing the evolution of the normalised energy in B_z in this simulation with the same quantity but in a simulation with counterpropagating electrons only and ions forming only an isotropic neutralising background, the curves perfectly overlap until $t \simeq 50\,\omega_{\mathrm{pi}}^{-1}$. This confirms that the instability is mainly fuelled by the electrons in this phase. For $t \gtrsim 50\,\omega_{\mathrm{pi}}^{-1}$, the energy in the magnetic field remains nearly constant for about $20\,\omega_{\mathrm{pi}}^{-1}$. After that, it starts

growing again exponentially until $t \simeq 320\,\omega_{\mathrm{pi}}^{-1}$ and saturates at $t \simeq 720\,\omega_{\mathrm{pi}}^{-1}$, after which it remains nearly constant until the end of the simulation. This dynamics is completely different from the case where ions are not streaming. Here, the magnetic field energy starts decaying right after $t \simeq 50\,\omega_{\mathrm{pi}}^{-1}$.

The second exponential growth phase in the electron-ion simulation is sustained by the ions, which begin to feel the effect of the magnetic field and participate in the instability right after the electron phase. The energy of the flow is mainly converted into magnetic field energy. However, the energies of the longitudinal (E_x) and in-plane transverse (E_y) electric field components also increase with time. The electric field component E_y is mainly due to charge separation. The magnetic field drives particles with different charges into different filaments creating regions that are richer in electrons or ions [92].
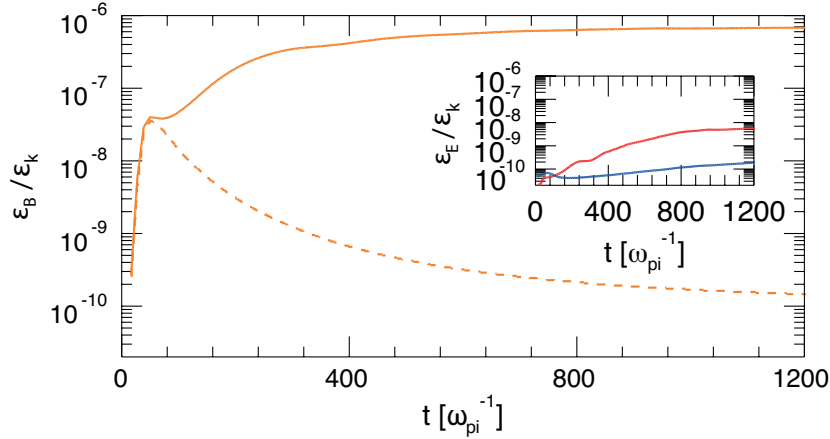
Figure 3.6:   Temporal evolution of B_z energy normalised to the total initial kinetic energy for a simulation with counterstreaming electrons and ions (solid) and counterstreaming electrons solely (dashed). The inset illustrates the time evolution of E_x (blue) and E_y (red) energies in the simulation with counterstreaming electrons and ions. In this simulation, $m_i/m_e = 1000, T_i = T_e = 0.0025\,m_e c^2$ and $v = 0.044\,c$.

Figure 3.7 shows the snapshots of the out-of-plane magnetic field B_z generated by the CFI. The magnetic field exhibits a filamentary structure due to the micro-currents generated by the particles. Figure 3.7 (a) shows the out-of-plane magnetic field at $t = 44.80\,\omega_{\mathrm{pi}}^{-1}$, where the electron Weibel instability generates small filaments with weak intensity. Following the saturation of the electron Weibel instability, the ions begin to respond to the instability, resulting in a further growth of the magnetic field (as observed in Fig. 3.6 for $80\,\omega_{\mathrm{pi}}^{-1} \lesssim t \lesssim 200\,\omega_{\mathrm{pi}}^{-1}$). Almost at the end of the CFI linear phase, $t = 224\,\omega_{\mathrm{pi}}^{-1}$, as illustrated in Fig. 3.7 (b), the field is more intense and the filaments weakly interact.
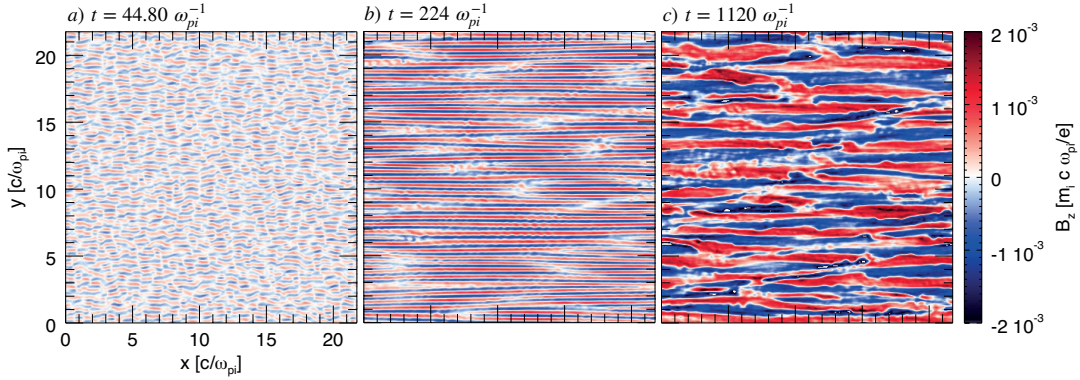
Figure 3.7: Out-of-plane magnetic field B_z at $t = 44.80$ (a), $t = 224$ (b) and $t = 1120\,\omega_{\text{pi}}^{-1}$ (c) for the same simulation of Fig. (3.6).
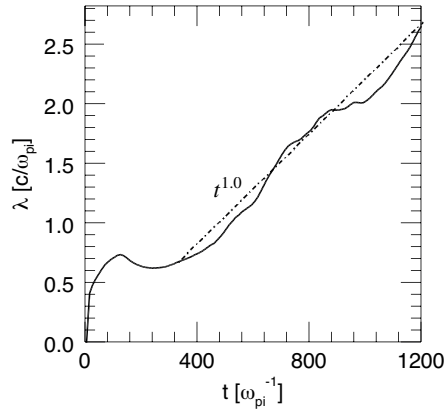
Figure 3.8: Temporal evolution of the average wavelength for the same simulation of Fig. (3.6). The dash dotted line represents a fit of the solid curve and indicates that the merging rate growth is $\propto t$.

As time progresses, the intensity of the magnetic field keeps increasing until t $\simeq 400\,\omega_{\text{pi}}^{-1}$, when the instability saturates. In the meantime, also the wavelength increases. This process continues even after the saturation of the instability ($t \gtrsim 1120\,\omega_{\text{pi}}^{-1}$), when the magnetic field stops growing. At $t = 1120\,\omega_{\text{pi}}^{-1}$ near the end of the simulation (Fig. 3.7 (c)), filaments are much larger and the average wavelength in the box increases. During the non-linear phase of the instability, the magnetic filaments become more and more tilted as they attract each other and merge. This gives rise to longitudinal wave modes, which leads to the growth of the E_x energy.

The magnetic field filaments generated by the instability evolve towards larger spatial scales during the simulation. This evolution is driven by the attraction and merging of filaments with opposite polarity. These filaments carry currents and induce

40

magnetic fields around them. As the simulation progresses, these filaments start to interact with each other. When filaments with opposite polarity come close to each other, their magnetic fields interact. This interaction can lead to a process of magnetic reconnection where the magnetic field lines break and then reconnect, causing a rearrangement of the magnetic field and the merging of adjacent filaments. These processes start during the linear phase of the instability and continue in the non-linear phase and beyond the point of maximum magnetic field energy [4], [93], [94]. Also the kink instability can contribute significantly to the coalescence of magnetic filaments and the formation of large-scale magnetic structures [95], [96]. However, this seems to mainly occur in 3D simulations, where modes in the third direction can develop. The merging process of filaments can be observed in Fig. 3.8, where the temporal evolution of the instability wavelength λ is shown together with a power law fit to determine its rate of variation. The averaged wavelength λ was determined using the formula $\lambda = 2\pi/k$ where k represents the wavenumber derived from the power spectrum of the magnetic field component. The power-law fit for $t \gtrsim 400\,\omega_{\mathrm{pi}}^{-1}$ in the non-linear phase of the instability indicates that the merging rate is $\propto t^{\beta}$ with $\beta = 1.0$. Previous simulations and theoretical models identify a similar power law for the evolution of the correlation length [3], [4]. However, according to these works, $\beta \approx 0.7$. The slightly slower rate with respect to the simulations of this thesis is probably due to the fact that previous works focused on relativistic regimes. In this latter case, due to the higher flow velocity, particles are more difficult for the field to be bent and so the merging process is slower.

As mentioned before, the instability grows at the expense of the particle flows. The free energy of the particles is converted into magnetic field energy causing the growth of the out-of-plane component of the magnetic field in the simulation (see Fig. 3.7). In turn, the field acts on the particles modifying their distribution. Figure 3.9 depicts this phenomenon and shows the phase space of electrons and ions initially flowing from left to right. At $t = 0$, both species exhibit a drifting Maxwellian distribution, as illustrated in Fig. 3.9 (a) and (b). During the electron instability phase, the distribution of electrons undergoes modifications, while the ions remain unaffected. Figure 3.9 (c) depicts this change, which results from the bending of the electrons by the magnetic field. This bending converts their drift velocity into heating and leads to the presence of non-Maxwellian features in their phase space [97]–[99]. During the electron instability, the phase space of ions does not undergo any significant change as shown in Fig. 3.9 (d). However, when the magnetic field strength becomes strong enough to deflect the ions at $t \gtrsim 200\,\omega_{\mathrm{pi}}^{-1}$, their distribution also starts to display phase space modification. As shown in Fig. 3.9 (f), the parallel drift velocity of the ions is transformed mainly into perpendicular heating as a result of this response. The phase space area occupied by the electrons increases throughout the ion phase which means that electron continue to heat up (Fig. 3.9 (e)). Figures 3.9 (g) and (h)
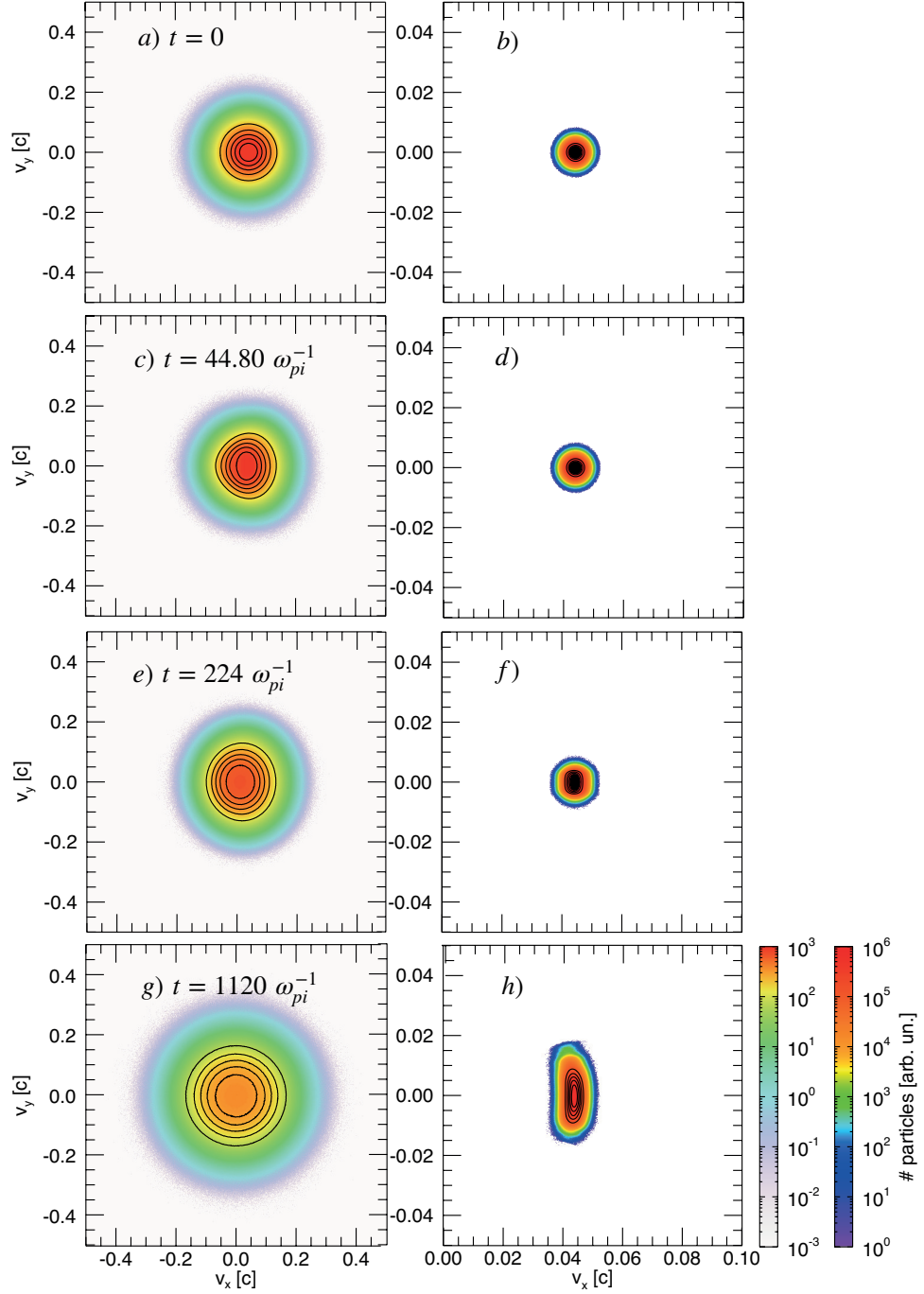
Figure 3.9: Phase space of electrons (left column) and ions (right column) with initial positive drift velocities at $t = 0.0$ (a)-(b), 44.80 (c)-(d), 224 (e)-(f) and 1120 (g)-(h) ω_{pi}^{-1} for the simulation of Fig. (3.6). The black lines represent curves of constant value of the distribution function, also known as contour lines.

display the phase space at $t = 1120\,\omega_{\mathrm{pi}}^{-1}$ for the electron and ion species, respectively. The ion phase space exhibits strong non-Maxwellian features, indicating significant deviations from the initial drifting Maxwellian distribution. In contrast, the electron distribution appears to be thermalised and has returned to a Maxwellian form. By looking at Fig. 3.9, it thus becomes evident that ions provide the free energy for the instability once the electrons have been thermalised [100].
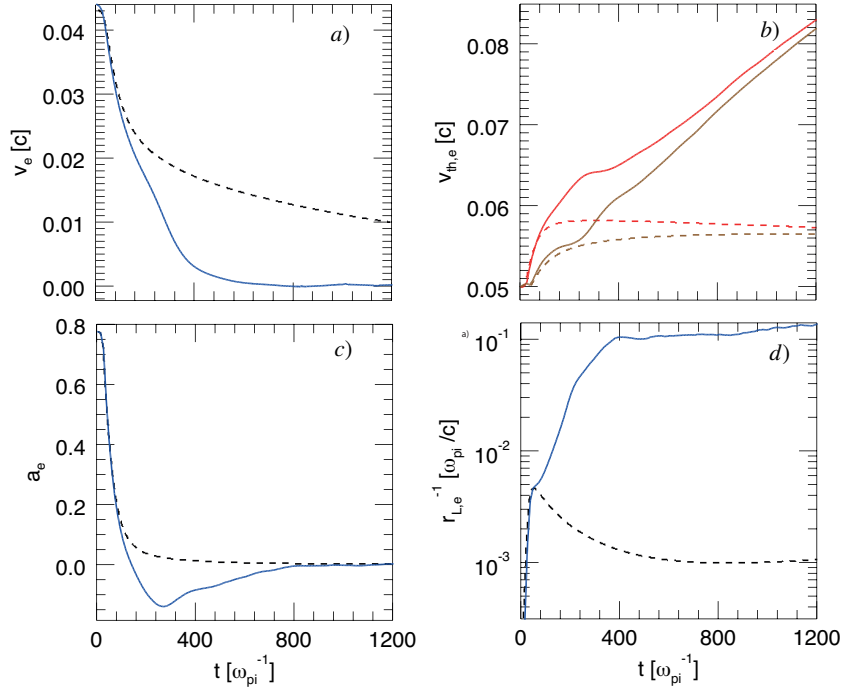
Figure 3.10: Evolution of the electron drift velocity (a), electron thermal speed along x (brown) and y (red) (b), electron anisotropy (c) and inverse electron Larmor radius (d). Solid lines represent results obtained modelling counterstreaming plasmas composed of electrons and ions, while dashed lines are results obtained considering counterstreaming electrons only. The same simulation setup as Fig. (3.6) has been considered.

The analysis of the evolution of some characteristics bulk parameters in the simulation confirms and reinforces the findings of Fig. 3.9. The electron drift velocity averaged over the simulation box, reported in Fig. 3.10 (a), is observed to rapidly decrease during the first phase of the instability where the magnetic field grows on electron time-scales ($t \ll 50\,\omega_{\mathrm{pi}}^{-1}$). When the electron instability reaches saturation ($t \simeq 80\,\omega_{\mathrm{pi}}^{-1}$), electrons still have a bulk velocity different than 0. Their velocity keeps decreasing during the ion phase of the instability ($t \gtrsim 100\,\omega_{\mathrm{pi}}^{-1}$), but at a slower rate.

At $t \simeq 400 \, \omega_{\mathrm{pi}}^{-1}$, when the magnetic field saturates, the electrons have lost their drift velocity. At this point, the bulk velocity is 0 and stays like this until the end of the simulation. It is interesting to compare this trend with the evolution of the electron drift velocity in a simulation with counterstreming electrons only. In this latter case, the drift velocity decreases at the same rate until $t \approx 80 \, \omega_{\mathrm{pi}}^{-1}$, where electron CFI reaches saturation. However, while in the simulation where ions participate to the instability, the electron bulk velocity eventually becomes 0, in this simulation, it keeps decreasing but very slowly and after 80 ion plasma periods, their bulk velocity is still considerable. This implies that the presence of drifting ions further enhances the electron slow-down process. This drift velocity is converted into electron heating. Both temperatures along x and y directions are observed to increase during the simulation (Fig. 3.10 (b)). It is interesting to notice that initially $v_{\mathrm{the},y}$ increases at a higher rate with respect to $v_{\mathrm{the},x}$. When the magnetic field reaches the first local maximum at $t \simeq 80 \, \omega_{\mathrm{pi}}^{-1}$, $v_{\mathrm{the},x}$ also seems to saturate. It then starts to increase again during the non-linear phase of the ion CFI ($t \gtrsim 320 \, \omega_{\mathrm{pi}}^{-1}$). The thermal velocity along y increases at a slightly slower rate after the magnetic field reaches the local maximum and its growth seems to saturate when the ion CFI enters in its non-linear phase. However, after $t \simeq 320 \, \omega_{\mathrm{pi}}^{-1}$, $v_{\mathrm{the},y}$ starts again to increase. Figure 3.10 (b) thus indicates that electrons keep getting heated even during the non-linear phase of the instability when their drift velocity approaches 0. In this phase their temperature appears to increase linearly with time. This picture contrasts with the results obtained from the electron only simulation, where both $v_{\mathrm{the},x}$ and $v_{\mathrm{the},y}$ increase only during the linear phase of the instability. The presence of ions impacts the behaviour of the plasma system. The ions play a role in dragging along the process of electron heating. By altering the structure of the magnetic field, ions influence the heating of electron. Combining $v_e, v_{\mathrm{the},x}$ and $v_{\mathrm{the},y}$ as defined by Eq. (3.21), the evolution of the electron anisotropy averaged over the simulation box can be computed. This is reported in Fig. 3.10 (c). In the linear regime of the electron scale instability, the anisotropy decreases abruptly. It reverses sign for $160 \, \omega_{\mathrm{pi}}^{-1} \lesssim t \lesssim 320 \, \omega_{\mathrm{pi}}^{-1}$ during the ion CFI. The change in sign indicates that the temperature along the y axis exceeds the combined temperature and velocity along the x axis. Consequently, this change substantially alters the anisotropy direction, leading to the predominance of CFI growth with k_x over k_y. It then increases and becomes approximately 0 during the non-linear phase of the instability. Also this parameter follows a different trend in the case of counterstreaming electrons only. The electron anisotropy decreases with the same rate as in the simulation with streaming electrons and ions until $t \approx 80 \, \omega_{\mathrm{pi}}^{-1}$, when the electron scale instability saturates. Then it slowly approaches 0. The evolution of the inverse electron Larmor radius defined as $r_{L,e}^{-1} = \frac{e|B_z|}{m_e c v_e}$, where v_e is the drift electron speed, is also shown in Fig. 3.10 (d). The evolution of this quantity is characterised by an exponential growth with two different growth rates during the

linear phase of the electron and ion instabilities. After the instability on ion time scale saturates, this value remains nearly constant. The ratio $r_{L,e}/\lambda = 0.002$, where λ is provided by Fig. (3.8), being significantly less than 1 indicates that electrons are fully trapped within the magnetic field filaments at the end of the simulation.
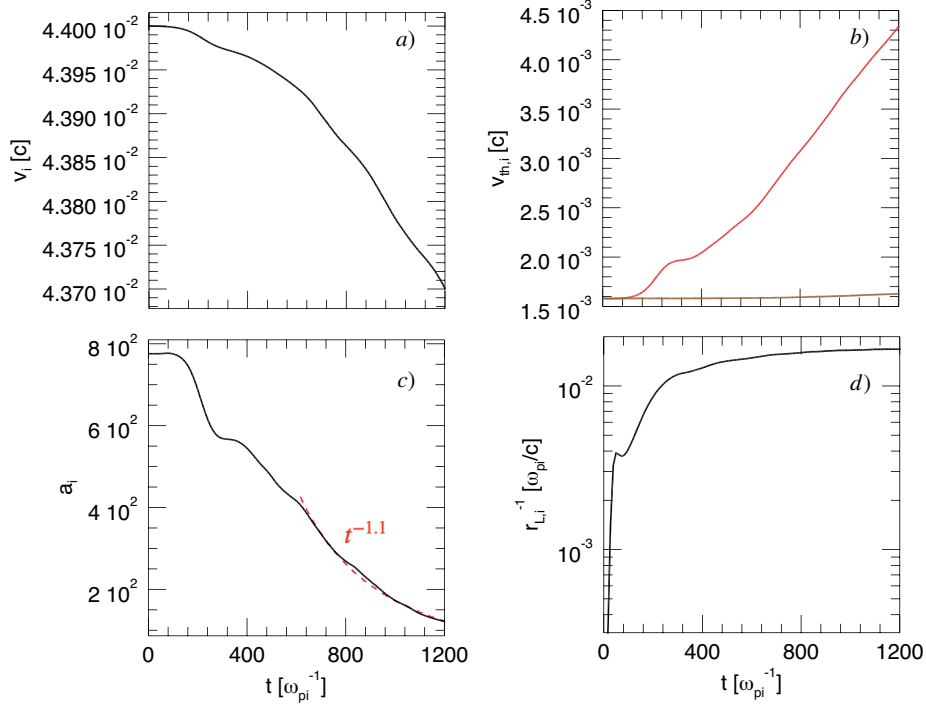
Figure 3.11: Evolution of the ion drift velocity (a), ion thermal speed along x (brown) and y (red) (d), ion anisotropy (c) and inverse ion Larmor radius (d). The red dashed line in (c) represents the rate of decrease of the ion anisotropy. The same simulation setup as Fig. (3.6) has been considered.

The ion bulk parameters are reported in Fig. 3.11. In particular Fig. 3.11 (a) shows the evolution in time of the drift velocity of the ions averaged over the simulation box. This quantity remains unchanged for $t \lesssim 160 \, \omega_{\text{pi}}^{-1}$, when the instability is solely governed by electrons. After that, the drift velocity starts to decrease. Ions loses their drift primarily during the non-linear phase of the instability ($t \gtrsim 400 \, \omega_{\text{pi}}^{-1}$). The longitudinal ion momentum gets converted mainly into perpendicular heating, as it can be seen from Fig. 3.11 (b), which shows the evolution of the ion thermal velocity along x and y averaged over the simulation box. While the ion temperature along y greatly increases during the non-linear phase of the instability, their temperature along x remains almost unchanged and it is observed to only slightly increase towards the end of the simulation. The evolution of the ion anisotropy, computed according to Eq. (3.21), is reported in Fig. 3.11 (c). The anisotropy of the ions shows a

trend similar to the electron anisotropy but the important difference is that at the end of the simulation the value is still high and this is what drives the merging processes. In particular, in the non-linear phase of the ion CFI, the ion anisotropy is observed to decrease as $t^{-1.1}$. If this trend remains unchanged, with a qualitative assessment, the merging process can be expected to continue for more than another 20 ion plasma periods. Finally, the inverse Larmor radius has been computed also for ions as $r_{L,i}^{-1} = \frac{e|B_z|}{m_i c v_i}$ (Fig. 3.11 (c)). The inverse Larmor radius increases exponentially during the electron and ion linear phase of the instability according to two different growth rates, similar to the electrons inverse Larmor radius. At saturation, the value of the inverse Larmor radius continues to increase very slowly as a result of the ion drift velocity becoming progressively smaller, while B_z is nearly constant. At the end of the simulation, the ratio between the ion Larmor radius and the average B_z wavelength in the simulation box is $r_{L,i}/\lambda = 25$. This is 4.4 order of magnitude larger than the electron ratio and suggests that in the simulation the ions are still free to move and are not trapped in the magnetic field filaments. As a consequence the instability can evolve toward larger and larger spatial scales.

3.8 Study of the impact of artificially small ion-to-electron mass ratios on the evolution of the instability

Previous numerical studies have explored the non-linear phase of the CFI on ion time scales using either ions with reduced mass ratios with m_i/m_e in the range $[25-40]$ [35], [94], [100] or relativistic flows with Lorentz factors of up to 10 [92], [101]. In order to understand the impact of using artificially lighter ions, a series of simulations with increasing ion-to-electron mass ratio m_i/m_e have been performed. In these simulations, $v_i = v_e = \pm 0.1\,c$, $T_{e,x}, T_{e,y} = 0.0025\,m_e c^2$ and $m_i/m_e = 200, 400$ and 1000.

The evolution of the out-of-plane transverse magnetic field equipartition parameter for each of the three m_i/m_e values mentioned above is shown in Fig. 3.12. Here, the lack of electron instability in the simulation is connected to the moment of data collection coinciding with electron saturation. The three curves are observed to increase with the same slope, which suggests that the evolution of the equipartition parameter is independent of the ion mass ratio. Hence, the growth rate of the ion CFI appears to be independent on the ion-to-electron mass ratio. Also the magnitude of ε_{B_z} at saturation does not seem to depend on this parameter. Indeed at saturation, this quantity is approximately the same in all three simulations. This might be due to the fact that changing the mass ratio, but keeping a fixed value of drift velocity increases the initial anisotropy of the ions. This increase in initial anisotropy might
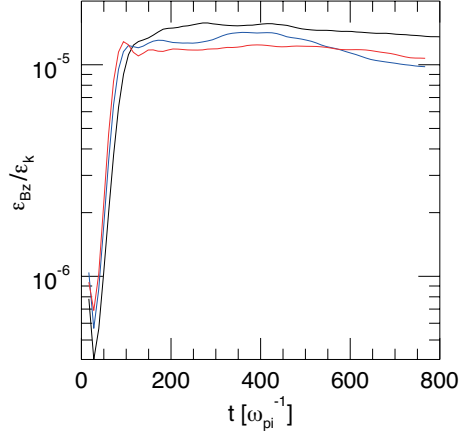
Figure 3.12: Evolution of the out-of-plane transverse magnetic field equipartition parameter for an electron-ion flow with drift velocity $v = \pm 0.1\,c$ and mass ratio $m_i/m_e = 200$ (red), $m_i/m_e = 400$ (blue) and $m_i/m_e = 1000$ (black).
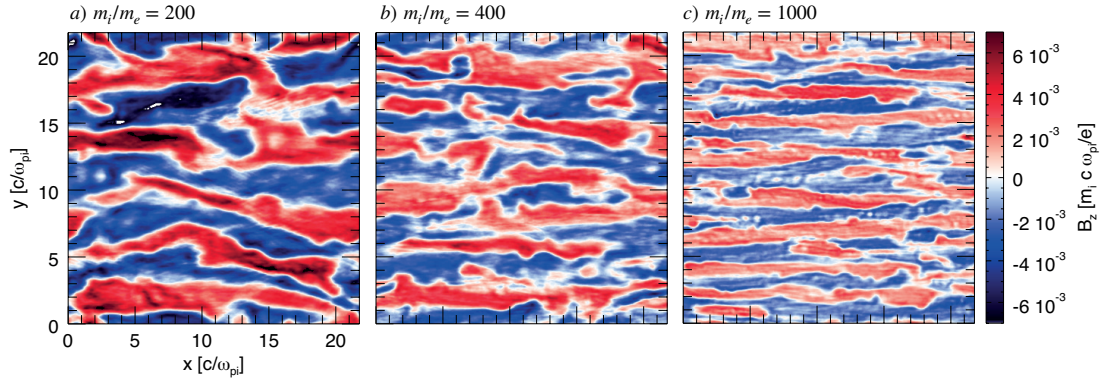
Figure 3.13: Out-of-plane magnetic field B_z in the simulation box at $t = 772.80\,\omega_{\text{pi}}^{-1}$ for $m_i/m_e = 200$ (a), 400 (b) and 1000 (c). The simulation setups correspond to those used in Fig. (3.12).

then compensate for the different ion-to-electron mass ratios and leads to similar evolutions for the equipartition parameter. The most evident difference in these simulations is given by the out-of-plane transverse field topology at the end of the simulations ($t \simeq 800\,\omega_{\text{pi}}^{-1}$) as shown in Fig. 3.13. In the case of $m_i/m_e = 200$, the magnetic field filaments are big (Fig. 3.13 (a)). Few wavelengths are present in the simulation box. The filaments are very tilted and the absolute value of the field is high. For $m_i/m_e = 400$, the size of the filaments is slightly smaller and the field is weaker (Fig. 3.13 (b)). When m_i/m_e is increased to 1000, several filaments are still visible in the simulation box (Fig. 3.13 (c)). The wavelength of the instability is about half the value reached at the end of the simulation for $m_i/m_e = 200$. The evolution of the
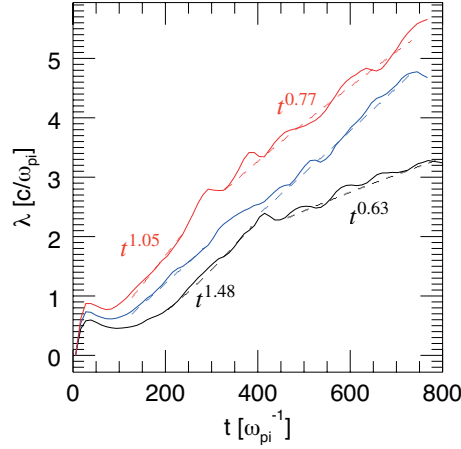
Figure 3.14: Evolution of B_z wavelength averaged over the simulation box for $m_i/m_e = 200$ (red), 400 (blue) and 1000 (black). Dashed lines indicate fits t^β with varying β. The simulation setups correspond to those used in Fig. (3.12).

average wavelength of B_z in the simulation box, reported in Fig. 3.14, quantitatively explains what observed in the plots of the field topology (Fig. 3.13). The average value of the wavelength increases throughout the duration of the whole simulation and it does not seem to saturate despite each simulation modelling hundreds of ion plasma periods. Depending on the value of m_i/m_e, filaments in the magnetic field cascade towards larger and larger spatial scales at different merging rates. In all cases investigated, the merging rate is proportional to t^β with β varying between 0.63 and 1.05. Furthermore, the rate at which filaments merge does not appear to be uniform during the duration of the simulation, but it decreases. A possible factor is the effect of secondary plasma instabilities, which can develop as the filaments merge. These instabilities can modify the merging process and introduce additional complexity to the system, leading to a decrease in the merging rate. The geometry of the magnetic field and the properties of the plasma can also play a role in the merging dynamics. For example, the presence of asymmetric or irregularly shaped magnetic fields can lead to a decrease in the merging rate due to the increased complexity of the merging process.

3.9   Study of the impact of different flow velocities on the evolution of the instability

This section is dedicated to understand the impact on the instability of the initial drift velocity when the same mass ratio is considered. For this reason a series of simulations with $m_i/m_e = 1000$, $T_{e,x} = T_{e,y} = 0.0025\, m_e c^2$ and $v_i = v_e = v$ in the
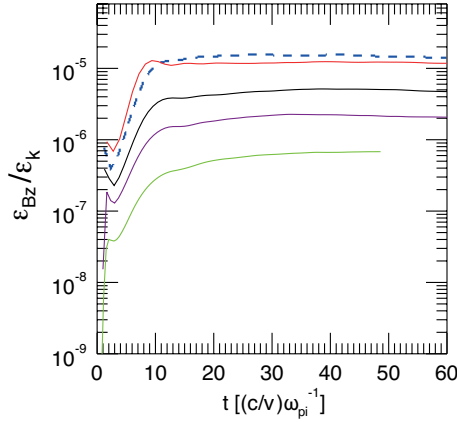
Figure 3.15: Evolution of the out-of-plane transverse magnetic field equipartition parameter for simulations with $m_i/m_e = 1000$ and drift velocity $v_i = v_e = v = \pm 0.1$ (red), ± 0.075 (black), ± 0.06 (purple) and ± 0.044 (green) c. The dashed blue line is the results of a simulation with $m_i/m_e = 200$ and $v = \pm 0.1\, c$. Please note that t on the x axis has been normalised to $(c/v)\omega_{\mathrm{pi}}^{-1}$ for allowing a better comparison of the different curves.

range $[0.1 - 0.044]\, c$ has been performed. The role of the initial ion anisotropy has also been investigated and previous results have been compared with a simulation where $m_i/m_e = 200$ and $v_i = v_e = \pm 0.1\, c$, which lead to an initial ion anisotropy of 816 (same as for the simulation with $m_i/m_e = 1000$ and $v_i = v_e = \pm 0.044\, c$).

Figure 3.15 shows the evolution in time of the B_z equipartition parameter for the aforementioned simulations. Note that time here has been normalised to $(c/v)\omega_{\mathrm{pi}}^{-1}$. By analysing this plot, it appears clear that the growth rate and the magnetic field at saturation have distinct values in the different simulations. Given the normalisation used, this result seems to indicate that the growth rate depends only on the drift velocity, with higher velocities corresponding to higher growth rates and higher values of B_z equipartition parameter at saturation. This appears to be confirmed also by comparing the two simulations with the same initial bulk flow, but different mass ratios. Indeed, in this case, the growth rate trends are similar in the linear and non-linear regime. It is also interesting to consider simulations starting from the same level of initial anisotropy (e.g. $m_i/m_e = 200$, $v_e = v_i = v = \pm 0.1\, c$ and $m_i/m_e = 1000$, $v_e = v_i = v = \pm 0.044\, c$). In these cases, different values for field growth rate and equipartition parameter at saturation are observed, meaning that therefore, as long as the drift velocity is the same, the growth rate is not significantly influenced by the anisotropy.

Figure 3.16 illustrates the transverse out-of-plane field topology at saturation time. By decreasing the drift velocity, the magnetic field undergoes filament modifications that result in straighter and less intense field compared to the case with the smallest
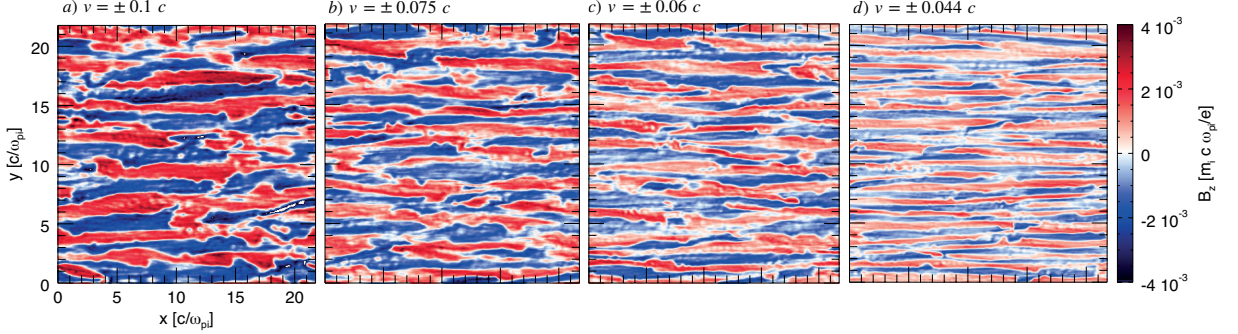
Figure 3.16: Out-of-plane magnetic field B_z in the simulation box at $t = 884.8\,\omega_{\rm pi}^{-1}$ for simulations with $m_i/m_e = 1000$ and $v_i = v_e = v = \pm 0.1$ (a), ± 0.075 (b), ± 0.06 (c) and ± 0.044 (d) c.

drift velocity. This change in the field is attributed to the merging of magnetic filaments, which redistributes the magnetic field energy and can cause magnetic field coalescence that alters the magnetic field topology. As a result, certain regions may have a more uniform magnetic field with weaker intensity. These considerations are reinforced by looking at Fig. 3.17, where the evolution of the average wavelength in the simulation box is reported. Again in this case, to have a better grasp of the underpinning physics, time has been normalised to $(c/v)\omega_{\rm pi}^{-1}$. With this normalisation, it can be observed that the average wavelength follows the same dynamics in all the simulations with the same ion-to-electron mass ratio. Indeed all the curves overlap, which is an indication of the fact that, given the same ion mass, the merging rate depends on the initial flow velocity. Since in these simulations, the initial anisotropy is different, Fig. 3.17 also indicates that given the same ion mass, the anisotropy does not have a significant impact on the evolution of the merging rate and the rate at which the magnetic field cascades towards larger scales. As before, it is interesting also to connect these results on the merging rate with that of a simulation performed with a reduced mass ratio. By comparing the simulation with $m_i/m_e = 200$ and $v = \pm 0.1\,c$ and the simulation with $m_i/m_e = 1000$ and $v = \pm 0.1\,c$, it is evident that in the former case the field evolves toward larger scales more rapidly. The same conclusion holds when the simulation with $m_i/m_e = 200$ and $v = \pm 0.1\,c$ is compared with the simulation with $m_i/m_e = 1000$ and $v = \pm 0.044\,c$, where the instability is triggered by the same initial level of ion anisotropy. Indeed also in this case, the field evolves toward larger scales more rapidly in the simulation with smaller mass ratio. Thus these tests seem to indicate that the ion-to-electron mass has a significant impact on the speed at which B_z evolves towards larger spatial scales. This means that previous works which consider artificially smaller mass ratios to speed up the simulations might have overestimated this quantity.
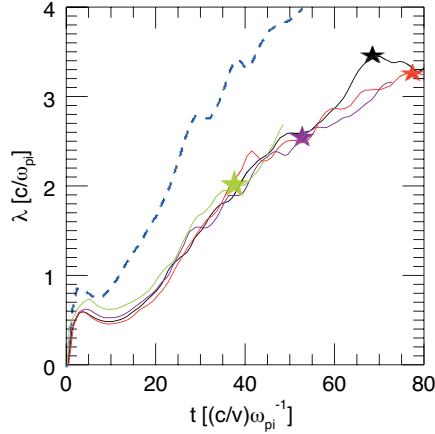
Figure 3.17: Evolution of B_z wavelength averaged over the simulation box with $m_i/m_e = 1000$ and $v_i = v_e = \pm 0.1$ (red), ± 0.075 (black), ± 0.06 (purple) and ± 0.044 (green) c. The dashed blue line represents the evolution of the average wavelengths for a simulation with $m_i/m_e = 200$ and $v_i = v_e = v = \pm 0.1\,c$ (same initial anisotropy as green line). The normalisation for t adopted in Fig. (3.15) has been used. Stars indicate $t = 884.8\,\omega_{\rm pi}^{-1}$ at which the field B_z is shown in Fig. (3.16).

3.10   Summary

In this study, the growth and saturation of electron-ion counterstreaming plasma flows were investigated using PIC simulations. The plasma dynamics on ion time scales was examined using the semi-implicit energy-conserving code ECsim [102]. The evolution of the magnetic field was analysed for various ion-to-electron mass ratios, different initial ansotropy values and many drift velocities.

The findings demonstrate that the magnetic field generated by the instability maintains its strength over hundreds of plasma periods. The behaviour of ions is observed to undergo significant changes during the initial linear phase of the instability. This is characterized by a rapid reduction in ion anisotropy, accompanied by the conversion of parallel kinetic energy into perpendicular heating. This phenomenon indicates a dynamic process where the ions motion transitions, influencing energy distribution and thermalisation. Following the linear phase of the instability, the ion anisotropy exhibits a continuous decrease. The role of the anisotropy becomes important in driving the long-term behaviour of the instability, marked by the continuous coalescence of magnetic filaments. The relationship between mass ratios and filament merging rates becomes evident as smaller mass ratios consistently translate to accelerated rates of filament coalescence. This observation highlights the significant role that mass ratios play in shaping the dynamics of this phenomenon. Meanwhile, higher drift velocities lead to a more rapid merging of the filamentary

structures.

Chapter 4

Magnetic field generation due to microinstabilities driven by ultra-relativistic particle beams

4.1 Introduction

Ultra-relativistic particle jets composed of electrons and positrons are common in astrophysical environments and are associated with some of the most luminous astrophysical objects, such as GRBs, SNRs and AGNs. The interaction of these jets with the surrounding medium drives a variety of plasma phenomena including the generation of intense magnetic fields and particle acceleration, which then cause the emission of gamma rays via synchrotron radiation. The possibility to explore in the laboratory the physics of relativistic outflows would be of great interest not only for astrophysics, but also to understand the physics of relativistic beam-plasma interactions. Although it is extremely challenging to replicate astrophysical conditions experimentally, modern accelerator facilities such as FACET-II at the SLAC National Accelerator Laboratory [103] may offer a solution. This chapter explores via simulations the possibility to recreate some astrophysical scenarios in the laboratory. In particular, it examines the prospect of using relativistic and ultra-relativistic electron and electron-positron (fireball) beams to mimic the interaction of astrophysical jets with the surrounding plasma with focus on possible kinetic instabilities, such as the CFI [33]. In the first part of the chapter, numerical simulations are employed to investigate the microphysics governing the movement of a neutral electron-positron beam into a magnetised plasma. A range of plasma magnetisation levels is considered to capture the different interaction scenarios. The longitudinal size of the beam is systematically varied to analyse its impact on the interaction process. The simulations are designed to emulate future laboratory

astrophysics experimental setups, targeting parameters achievable at FACET-II where both ultra-relativistic electron and positron bunches will soon be available. The second part of the chapter focuses on analysing the microphysics connected to the propagation of a relativistic electron beam into an unmagnetised plasma. In this case, simulations model beam parameters achievable at the Compact Linear Accelerator for Research and Applications (CLARA) at the Cockcroft Institute of Accelerator Science and Technology [104]. The final goal of this study is then to propose an experiment in the near future to probe the physics demonstrated in these simulations and make connections with astrophysical settings.

4.2 Relativistic fireball beam propagation through a static magnetised plasma

This section presents a series of 2D simulations conducted to investigate the microphysics underpinning the propagation of a neutral beam composed of electrons and positrons, known as fireball beam, into a magnetised plasma. The simulations aim at finding a possible configuration to explore the interaction between ultra-relativistic astrophysical jets with the interstellar medium in the laboratory via properly scaled experiments.

In the absence of a background magnetic field, the propagation of an ultra-relativistic beam composed in equal measures of electrons and positrons may drive the CFI and generate a strong magnetic field [22], [35]. This occurs as the ultra-relativistic beam propagates through the plasma, inducing a return current in the plasma to maintain charge neutrality. The interaction between the beam and the return current can lead to the growth of instabilities, such as the CFI. In this process, the return current acts as a seed for the development of filamentary structures and amplifies magnetic fields through this mechanism. In particular, the development of the instability is determined by two parameters: the transverse beam size σ_r relative to the plasma skin depth and the Lorentz factor of the beam γ_b [33]. In the regime where the transverse beam size is larger than the plasma skin depth ($\sigma_r > c/\omega_p$) the return current passes through the beam, creating conditions for kinetic instabilities to develop. In this regime, if $\gamma_b \gg 1$, the interaction between the beam and the plasma leads to the generation of filamentary structures and the development of the CFI, while if $\gamma_b \ll 1$, the longitudinal two stream instability is expected to occur. In both cases, these microinstabilities can significantly affect the beam stability and propagation. On the other hand, when the transverse beam size is smaller than the plasma skin depth ($\sigma_r < c/\omega_p$), the plasma return current flows outside the beam. This particular regime is highly favourable for plasma wakefield accelerators (PWFA) and the CFI does not occur [30], [33]. In PWFA setups, where the transverse beam size

is smaller than the plasma skin depth, the beam-plasma interaction primarily involves the formation of plasma waves that can efficiently accelerate charged particles. By understanding the interplay between the transverse beam size, the Lorentz factor and the plasma skin depth, it is possible gain insights into the conditions necessary for the CFI to occur [33].

The presence of a pre-existing background magnetic field, as that characterising the intergalactic medium, could lead to different physics. Understanding how this pre-existing field modifies the onset and development of plasma microinstabilities and the generation of strong magnetic fields is the focus of the PIC simulations illustrated in this section. For this purpose, simulations model a beam made of an equal number of electrons and positrons with a density profile $n_b(x,y) = n_{b0} \exp\left(-x^2/\sigma_x^2 - y^2/\sigma_y^2\right)$, where $\sigma_x = 0.99\,c/\omega_p = 10.2\,\mu\mathrm{m}$ is the bunch length root mean square (RMS) and $\sigma_y = 2.0\,c/\omega_p = 20.4\,\mu\mathrm{m}$ is the bunch transverse size RMS. The peak beam density is $n_{b0} = 0.37\,n_0$ where $n_0 = 2.7 \times 10^{17}\,\mathrm{cm}^{-3}$ is the electron plasma background density. Simulations follow the beam with a moving window travelling at the speed of light c along the x axis. The beam moves with a velocity $\mathbf{u}_b = v_b\gamma_b\mathbf{e}_x$ and an initial Lorentz factor of $\gamma_b = 56000$. An isotropic Maxwellian in velocity space with a thermal spread of $v_{th} = 1.7 \times 10^{-5}\,c$ for both electrons and positrons has been considered. The typical simulation box has dimensions of $L_x = 14.08\,c/\omega_p$ and $L_y = 46.08\,c/\omega_p$, from $-L_y/2$ to $L_y/2$. The spatial resolution is set to $\Delta x = \Delta y = 0.02\,c/\omega_p$, with a time step of $0.011\,\omega_p^{-1}$, unless differently specified. Each cell in the simulation contains 9 particles-per-cell per species and a fourth order interpolation scheme has been selected. The box has absorbing boundary conditions in the transverse direction, which means that particles that pass through the boundary in the transverse direction are eliminated from the simulation. Perfectly Matched Layers (PML) are an advanced method used as absorbing boundary conditions in simulations to prevent reflections of electromagnetic waves at the boundaries. Vay's hybrid algorithm effectively implements PML. In the code, this is achieved by introducing additional damping terms and modifying the field equations within the PML region to simulate absorption. Additionally, the fields are absorbed at the boundary by gradually reducing them to zero, in order to prevent the reflection of waves back into the box. The fireball beam is initially set up in vacuum and when it starts to propagate meets a plasma with density profile $\propto 0.5(\tanh(10x_1) + 1)$. This density profile was chosen to prevent misleading fields brought on by an abrupt plasma-to-vacuum transition. An intense beam in the absence of external fields propagating in vacuum evolves in its self-fields. The radial electric force due to the beam space charge always dominates the self-magnetic pinching force. The simulation started with a neutral fireball beam in vacuum to ensure its stable propagation with a constant radius. The plasma was modelled with mobile cold electrons with $v_{th} = 1.7 \times 10^{-5}$ and immobile ions which only provide charge neutrality. It is acceptable to ignore the motion of ions that are typically
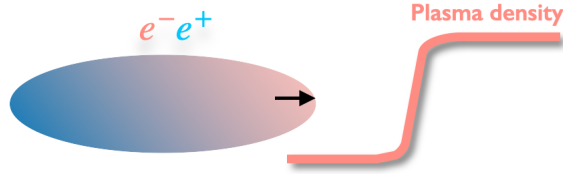
Figure 4.1: Sketch of the simulation setup. The e^-e^+ neutral beam drifts in the x positive direction interacting with a static plasma.

mobile, as the relevant processes of interest operate on timescales significantly shorter than those associated with ion movement. The Fei algorithm [77], [78] mentioned in Chapter 2 has been employed to avoid numerical effects due to the presence of ultra-relativistic particles. Finally, it has been verified that different spatial and temporal resolutions, number of particles per cell and interpolation levels yield similar results showing that the obtained results are physical and not due to numerical artefacts [105]. The external magnetic field was set up as $\mathbf{B}_0 = B_0 \mathbf{e}_x$. The simulation setup is schematically presented in Fig. 4.1, where the e^-e^+ neutral beam drifts in the x positive direction interacting with a static plasma.

The presence of a background magnetic field in the direction parallel to the particle propagation is expected to influence the growth and development of kinetic instabilities. For instance, it has been shown that in the case of infinite counterstreaming electron plasmas the presence of an external magnetic field aligned with the electron bulk motion suppresses the formation of filaments due to the CFI when such field is above a critical threshold [43].

In order to analyse the influence of a background magnetic field on the microphysics of the interaction between an electron-positron beam and a static plasma, a series of simulations has been carried out. In these simulations, a uniform background magnetic field with increasing amplitude has been considered. In particular B_0 has been varied between 0 and 8.5 MG.

Figure 4.2 displays the evolution of the magnetic and electric field energies versus beam propagation distance for different magnetisation levels of the plasma. The electromagnetic field energies are normalised to the total kinetic energy of the particles $\varepsilon_p = m_e c^2 (\gamma_b - 1) V_b$, where $V_b = \sigma_x \sigma_y \pi$ is the volume of the beam (values are then re-normalised to ε_{B_g}, where B_g is the field at which the growth turns exponential, usually after 5 cm of propagation; this re-normalisation was performed to enable a direct comparison with [22]). By normalising the magnetic field energy to ε_p, can relate the energy stored in the fields to the total rest energy of the particles in the beam and the spatial extent of the beam. Figure 4.2 (a) shows that in the absence of a background magnetic field the propagation of the beam into the plasma causes the generation and amplification of the magnetic field in the out-of-plane direction. The out-of-plane

magnetic field is observed to grow at a rate $\Gamma_{B_z} = 1.41 \times 10^{-3}\,\omega_p$. Simultaneously, the growth of the electric field components in the propagation direction E_x and in the in-plane transverse direction E_y occurs. Both fields exhibit similar growth rates to the B_z. When a background magnetic field with strength of 2.8 MG in the beam propagation direction is present, the out-of-plane magnetic field (B_z) exhibits a slightly lower growth rate of $1.21 \times 10^{-3}\,\omega_p$ (Fig. 4.2 (b)). In this case, the growth of the longitudinal and transverse electric field components (E_x and E_y) is also evident, although these fields grow at a lower rate with respect to the unmagnetised case of Fig. 4.2 (a). The similarity in the growth between E_y and B_z for $B_0 = 2.8$ MG suggests a strong correlation between these two field components. By increasing the external magnetic field intensity to 5.6 MG (Fig. 4.2 (c)), B_z is observed to grow at a much lower rate of $8.9 \times 10^{-4}\,\omega_p$. Furthermore, the saturation level begins to shift forward in propagation, indicating a modified behaviour under the increased magnetic field intensity. For a higher magnetisation value of $B_0 = 8.5$ MG (Fig. 4.2 (d)), the growth rate of B_z decreases to $6.5 \times 10^{-4}\,\omega_p$. In the case shown in Fig. 4.2 (d), the saturation level, where the growth rates of B_z, E_x and E_y stabilise, occurs after approximately 25 cm of beam propagation into the plasma. This indicates that the system requires a long plasma for the instability caused by the beam to saturate. Figure 4.3 (a) presents the growth rate (Γ/ω_p) of B_z for a range of initial external magnetic field values from 0 to 8.5 MG and provides confirmation of the observations made earlier. The growth rates of the out-of-plane magnetic field component (B_z) are significantly influenced by the level of background magnetisation. Specifically, as the external magnetic field intensity increases, a distinct decrease in the growth rate of B_z, as well as E_x and E_y, is observed. In particular, the growth rate of B_z appears to decrease linearly with B_0. The variation of Γ/ω_p within a small range of magnetisation values, specifically from 0 to 0.6 MG, is depicted in Fig. 4.3 (b). As this plot shows, a low level of magnetisation does not significantly impact the growth of the out-of-plane magnetic field (B_z), as it remains relatively constant across this range.

Figure 4.4 provides snapshots of the out-of-plane magnetic field configuration after the fireball beam has propagated a distance of 29.5 cm into the plasma. This distance (29.5 cm) was selected in order to compare the non linear phase of the instability. In the absence of an external magnetic field aligned with the beam bulk speed (Fig. 4.4 (a)), the magnetic field in the out-of-plane direction presents a filamentary structure characterised by straight horizontal filaments. The presence of completely perpendicular modes seems to indicate that in this case the magnetic field growth is caused by the CFI. Indeed the instability growth rate appears to be in good agreement with the maximum growth rate predicted by the theory for the relativistic CFI driven by a beam: $\Gamma^{Th} = v_b/c\sqrt{\eta/\gamma_b}\,\omega_p \simeq 2.6 \times 10^{-3}\omega_p$ [106]; here the small difference could be justified by the fact that the theory is derived for an infinite beam, but also by the fact that in the simulations, the growth rate is computed from the energy of B_z,
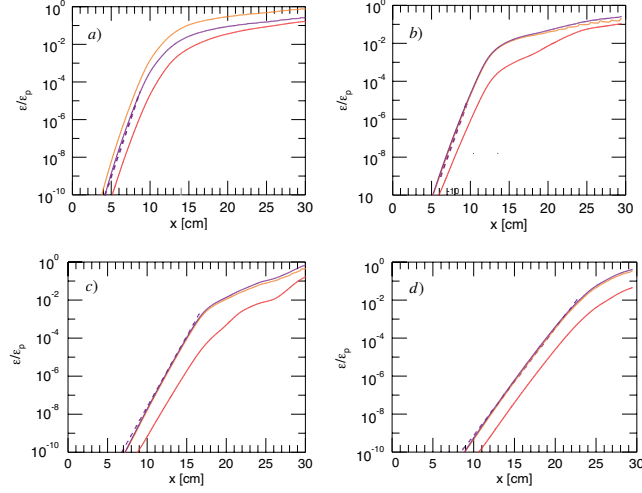
Figure 4.2: Equipartition parameter of B_z (violet), E_x (red) and E_y (orange) versus fireball beam propagation distance for $B_0 = 0$ (a), 2.8 (b), 5.6 (c) and 8.5 (d) MG. The dashed lines show the growth rate of B_z energy.
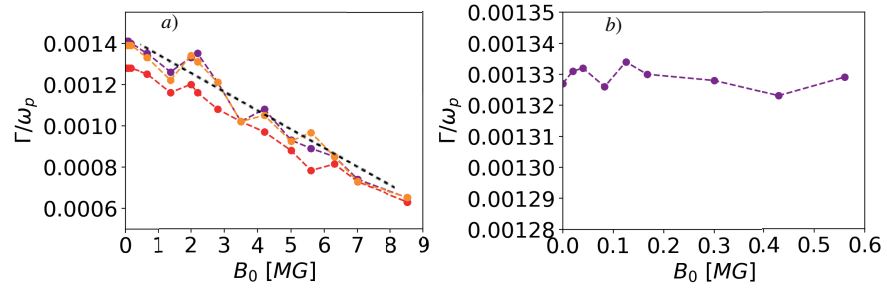
Figure 4.3: Growth rate of longitudinal electric field E_x (red), transverse electric field E_y (orange) and magnetic field B_z (purple) versus background magnetic field B_0 (a). The black dashed line results from a linear fit of the data. Detail of Fig. (a) showing B_z for B_0 between 0 and 0.6 MG (b).

thus summing over the contribution of all wavenumbers. As a fireball beam passes through a plasma, its electrons repel the background electrons, while its positrons attract them. To maintain overall charge neutrality in the plasma, a return current forms. The presence of a return current passing through the beam induces the CFI with the amplification of every infinitesimal perturbation of the magnetic field. The development of CFI and the growth of the magnetic field induce the development of transverse and longitudinal electric fields of electrostatic and inductive nature, respectively [35].

The presence of a background magnetic field in the direction of the beam propagation enhances the oblique characteristics of the filaments. As higher values of background magnetic field are considered, the out-of-plane magnetic field due to the instability stops exhibiting only straight filaments (Figs. 4.4 (b)-(d)). Oblique filaments start to appear as the beam propagates through the plasma. The topology of the field thus hints to the growth of oblique modes together with the growth of transverse modes. As the magnitude of the external magnetic field becomes higher and higher, filaments become more and more tilted indicating that oblique modes become more and more important. Perpendicular modes still develop in front of the oblique modes, but their spatial extent is reduced. The presence of a background magnetic field thus appears to change the nature of the instability triggered by the ultra-relativistic beam. If for small B_0 up to about 0.6 MG, given the field topology and the almost constant growth rate, the growth of B_z is due to the CFI, for higher values of B_0, B_z is certainly due to the interplay of different kinetic instabilities.

Figure 4.5 (a) shows electron and positron particle densities in the absence of B_0. The tail of the beam clearly shows filaments visible in both the electron and positron densities. For $B_0 = 2.8$ MG, a slight tilt can be observed in the electron and positron density filaments (Fig. 4.5 (b)), along with a corresponding tilt in the E_x profile (Fig. 4.5 (f)). As the magnetisation level increases to $B_0 = 5.6$ MG, the tilt of the filaments in the electron particle density becomes more pronounced (Fig. 4.5 (c)), arising in a oblique configuration of the E_x field (Fig. 4.5 (g)). Figure 4.5 (d) illustrates the electron-positron particle density for the highest value of background magnetic field considered ($B_0 = 8.5$ MG). In this case, the filaments become more twisted, displaying complex interconnections. The corresponding longitudinal electric field (E_x) exhibits oblique modes with an increased number of filaments (Fig. 4.5 (h)). Thus, these plots show that the presence of an external magnetic field alters the characteristics of the modes triggered by the propagation of an ultra-relativistic fireball beam in a static plasma. The magnetic field introduces additional forces and constraints on the charged particle motion, leading to more complex and distorted filament structures in both the particle density and the longitudinal electric field, as well as the generated out-of-plane magnetic field.

The impact on the growth of B_z of a progressively longer beam has also been
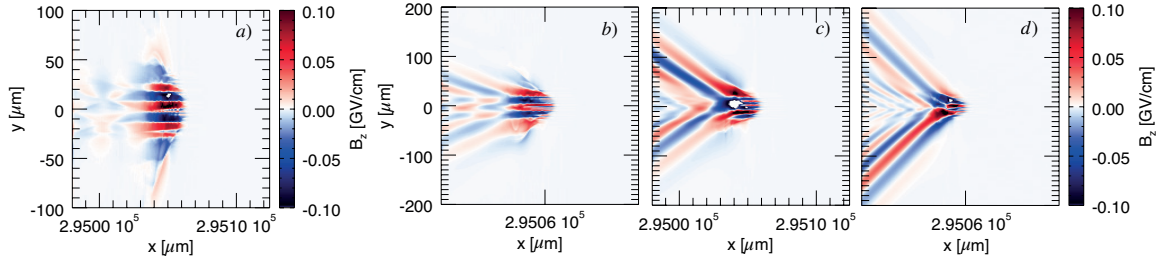
Figure 4.4: Out-of-plane magnetic field B_z after the beam has propagated 29.5 cm into the plasma for $B_0 = 0$ (a), 2.8 (b), 5.6 (c) and 8.5 (d) MG.
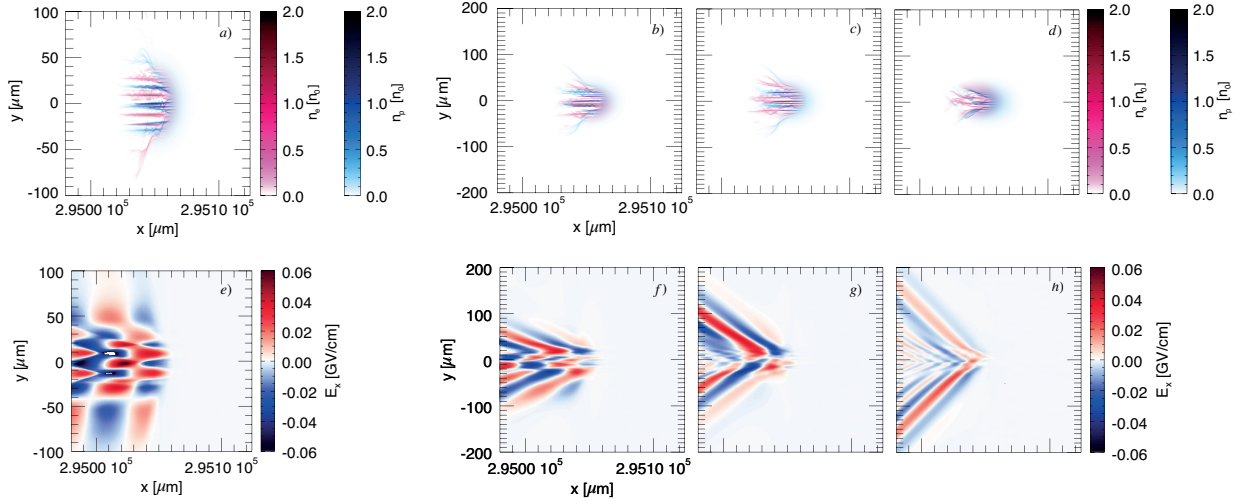

Figure 4.5: Electron (pink) and positron (blue) density (upper panels) and longitudinal electric field E_x (lower panels) after the beam has propagated 29.5 cm into the plasma for $B_0 = 0$ (a, e), 2.8 (b, f), 5.6 (c, g) and 8.5 (d, h) MG.

Cases	σ_x	n_{b0}/n_0	$L_x[c/\omega_p] \times L_y[c/\omega_p]$
$B_0 = 5.6$ MG $\sigma_y = 2\,c/\omega_p = 20.4\,\mu\mathrm{m}$			
I	$\sigma_x = \sigma_{x,0} = 0.99\,c/\omega_p = 10.2\,\mu\mathrm{m}$	0.37	14.08×46.08
II	$1.25\ \sigma_{x,0}$	0.29	17.60×46.08
III	$1.50\ \sigma_{x,0}$	0.24	21.10×46.08
IV	$1.75\ \sigma_{x,0}$	0.21	24.60×46.08
V	$2\ \sigma_{x,0}$	0.185	28.16×96.16
VI	$3\ \sigma_{x,0}$	0.123	42.23×138.20
VII	$4\ \sigma_{x,0}$	0.092	56.31×138.20
VIII	$5\ \sigma_{x,0}$	0.074	70.40×184.32
IX	$6.29\ \sigma_{x,0}$	0.058	89.60×184.32

Table 4.1: Summary of the simulations performed to investigate the effect of longer beams on the generation of magnetic field via kinetic instabilities. In these simulations, $B_0 = 5.6$ MG. The number of total particles composing the fireball beams has been kept constant, as well as the transverse beam size σ_y. As larger values of σ_x are considered, the peak density of the beam n_{b0}/n_0 decreases. The last column reports the size of the simulation box in the different runs.

analysed. To explore the effect on the instability of a longer fireball beam, 2D simulations modelling the beam propagation through a static magnetised plasma with a $B_0 = 5.6$ MG have been performed. In these simulations, the real number of particles composing the fireball beam has been maintaied constant. This choice has been made to better simulation results with possible experiments, where stretching the particle beams will lower the bunch peak density. As a consequence in the simulations, when considering larger values of σ_x, lower values of $\eta = n_{b0}/n_0$ were initialised. In particular, σ_x assumes values in the range from 1 to $6.29\,c/\omega_p$ and the corresponding density η varies from 0.37 to 0.058. Table 4.1 lists the simulations performed and the values of σ_x and beam density considered. The table also reports the size of the simulation box for the different runs. L_x was increased to accomodate longer beams, while L_y was increased to allow the oblique modes to develop without worrying about the transverse boundary conditions. In these simulations, the box was divided into cells with dimensions of $\Delta x = \Delta y = 0.02\,c/\omega_p$. The number of cells N_x and N_y was determined based on the size of the box.

Figure 4.6 displays the evolution of the magnetic and electric field energies versus beam propagation distance, normalised to the kinetic energy ε_p and the value of the out-of-plane magnetic field B_z when the its growth starts to be exponential. Figures 4.6 (a) and (e) show these quantities for the smallest σ_x considered ($\sigma_x = \sigma_{x,0} =$
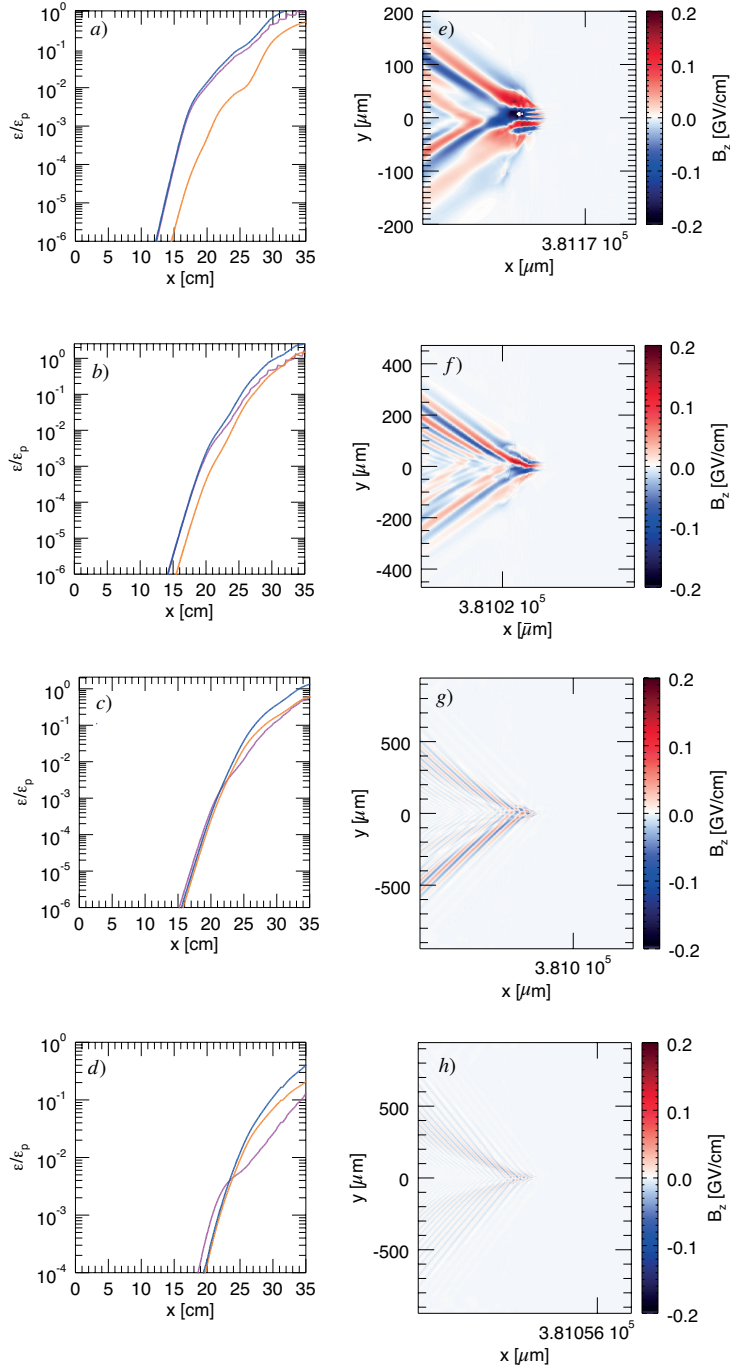
Figure 4.6: Equipartition parameter for B_z (blue), E_x (orange) and E_y (purple) versus fireball beam propagation distance (left panels) and out-of-plane transverse magnetic field (right panels) for beams with longitudinal length $\sigma_x = \sigma_{x,0} = 10.2\,\mu\text{m}$ (a)-(e), $2\sigma_{x,0}$ (b)-(f) $5\sigma_{x,0}$ (c)-(g) and $6.29\sigma_{x,0}$ (d)-(h).
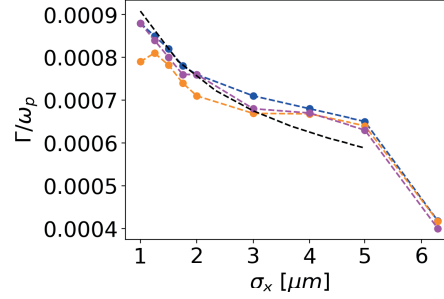
Figure 4.7: Growth rate of longitudinal electric field E_x (orange), in-plane transverse electric field E_y (purple) and transverse out-of-plane magnetic field B_z (blue) versus longitudinal beam size. The black dashed line represents a fit of the simulation data $\propto \sigma_x^{-2}$.

$10.2\,\mu\text{m}$). In this case, the transverse electric field (E_y) and the transverse magnetic field (B_z) energy trend overlap, and both energies present a growth rate of $\Gamma_{Bz} = \Gamma_{Ey} = 8.5 \times 10^{-3}\,\omega_p$, while the E_x energies grow at a slightly lower rate. The out-of-plane magnetic field shows the presence of transverse modes followed by oblique modes characterised by tilted beam filaments at the back of the bunch. When the longitudinal beam size σ_x is doubled and η gets reduced to 0.18, the magnetic field growth rate slightly decreases to $\Gamma_{Bz} = 7.6 \times 10^{-4}\,\omega_p$ (Fig. 4.6 (b)). Here, E_y and B_z energies continue to show an overlapping trend while the growth rate of E_x energy becomes more similar. The out-of-plane magnetic field shows more oblique filaments (Fig. 4.6 (f)). In the case of $\sigma_x = 5\sigma_{x,0}$ and $\eta = 0.074$, B_z, E_x and E_y energies trend overlap perfectly, as displayed in Fig. 4.6 (c). The fields exhibit the same growth rate $\Gamma_{Bz} = \Gamma_{Ex} = \Gamma_{Ey} = 6.5 \times 10^{-4}\,\omega_p$. In this case the fields start to grow exponentially approximately after the beam has propagated 15 cm into the plasma, slightly later than when shorter beams are considered. Figure 4.6 (g) illustrates the topology of B_z for the same case. The field exhibits a lower intensity compared to the fields driven by shorter beams but displays a higher number of filaments. The largest longitudinal beam size modelled has been $6.29\sigma_{x,0}$, corresponding to one plasma wavelength, λ_p with $\lambda_p = 2\pi c/\omega_p$. In this case the rate at which B_z grows is observed to decrease to $\Gamma_{Bz} = 4.1 \times 10^{-4}\,\omega_p$ (Fig. 4.6 (d)). Here E_x and B_z energies display the same trend while the E_y energy starts to increase before the other components. Thus, this study suggest that longer longitudinal beams with lower density still trigger kinetic instabilities leading to the generation of magnetic fields. By analysing the slope of the curve in Fig. 4.6 (a)-(d) it was represented the growth rate versus the longitudinal beam size in Fig 4.7. The growth of these fields occurs at a slower rate, as shown in Fig. 4.7. Moreover, the plot of Fig. 4.7 points out that for beam shorter than λ_p, the growth rate decreases quadratically, increasing the beam length. Additionally, as the

longitudinal beam size increases, a corresponding decrease in the magnitude of B_z is observed.

4.3 Relativistic electron beam propagation through a static plasma

This section explores the microphysics connected to the propagation of a relativistic electron beam in a static unmagnetised plasma. It is known that such configuration leads to the generation of strong magnetic fields due to the CFI [33]. The primary goal of the present study is to test whether the physics of the CFI and the resulting magnetic field generation can be probed with electron beams produced by CLARA [104]. Thus, 2D simulations using OSIRIS [74], [75] were performed to investigate the interaction between an electron beam and a uniform plasma. The beam velocity was set to $\mathbf{u}_b = \gamma_b v_b \mathbf{e}_x$, with a Lorentz factor of $\gamma_b = 117.24$, equivalent to 59.5 MeV. This energy closely matches that of the CLARA electron beam. An electron bunch with longitudinal and transverse sizes of $\sigma_x = 4\,c/\omega_p = 30\,\mu\text{m}$ and $\sigma_y = 8.30\,c/\omega_p = 62.5\,\mu\text{m}$ respectively, was considered. The beam density was $n_{b0} = 8.47 \times 10^{-4} n_0$ where $n_0 = 5 \times 10^{17} \text{cm}^{-3}$ is the electron plasma background density. The thermal velocity of the beam was $v_{th}/c = 0.01$. These beam parameters will be attainable at CLARA with the upgrade that provide a beam energy up to 250 MeV. The system was studied numerically with a window of sizes $L_x = 78\,c/\omega_p$ and $L_y = 336\,c/\omega_p$ (from $-L_y/2$ to $L_y/2$) moving at the speed of light along the x direction and discretised in $N_x = 624$ and $N_y = 2688$ cells with absorbing boundary conditions for fields and particles in the transverse direction. The time step was set to $0.072\,\omega_p^{-1}$. Each cell in the simulation contains 16 particles-per-cell per species and a fourth order interpolation scheme has been selected.

The temporal changes in electromagnetic energy that occur during the propagation of the electron beam into the static unmagnetised plasma are shown in Fig. 4.8, (the parameters are normalised to the total kinetic energy of the particles ϵ_p). As the electron beam passes through the plasma, the electromagnetic fields start to grow. The electric field components E_x and E_y undergo significant amplification, reflecting the pronounced influence of the beam-plasma interaction. Simultaneously, the magnetic field component B_z experiences an increase due to the beam current, which is responsable for the magnetic field itself. During the non-linear stage, which occurs approximately after 2.5 cm of propagation, distinct changes are observed in the evolution of the electromagnetic field components. The E_y component shows a decreasing energy trend while the B_z component remains constant. Additionally, the E_x component shows an amplification of the energy. The out-of-plane transverse magnetic field topology is reported in Fig. 4.9 for two distinct plasma penetration
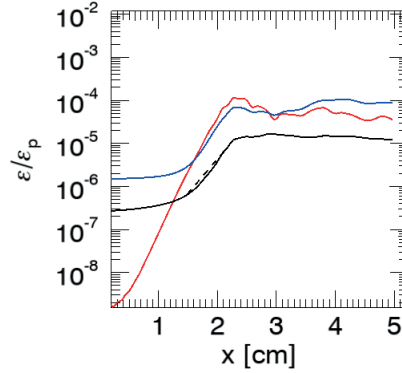
Figure 4.8: Electromagnetic energy of B_z (black), E_x (blue) and E_y (red) versus electron beam propagation distance for the interaction between a relativistic electron beam and a plasma. The black dashed line shows the fit of B_z growth rate.

distances 2.04 cm (Fig. 4.9 (a)) and 4.90 cm (Fig. 4.9 (b)). The filaments begin to become evident qualitatively after the beam has propagated for 2 cm into the plasma (Fig. 4.9 (a)). After approximately 4 cm of beam propagation through the plasma, the filaments increase the size and intensity (Fig. 4.9 (b)). This phenomenon can be attributed to the non-linear effects and interactions between the filaments as they travel through the plasma. Figure 4.10 shows the electric field component in the box E_x. The filamentary structures observed in the longitudinal electric field after a propagation distance of 2.04 cm (Fig. 4.10 (a)) are a direct consequence of the collective plasma response to the presence of the electron beam. The longitudinal electric field E_x has undergone transversal expansion after propagating a distance of 4.90 cm (Fig. 4.10 (b)).

The particle density of the electron beam is reported in Fig. 4.11. After 2 cm of electron beam propagation into the plasma, interesting filamentary structures start to appear within the beam (Fig. 4.11 (a)). These filaments correspond to localised regions of enhanced particles density or electron clustering. The presence of these filaments indicates the formation of the CFI resulting from the interplay between the beam and the surrounding plasma. With continued propagation of the electron beam beyond 4 cm (Fig. 4.11 (b)), the filaments of the particle density become more pronounced.

4.4   Summary

The interaction of an ultra-relativistic neutral electron-positron beam with a magnetised plasma has been investigated using 2D numerical simulations based on the PIC method. The development of a mixture between purely transverse and oblique
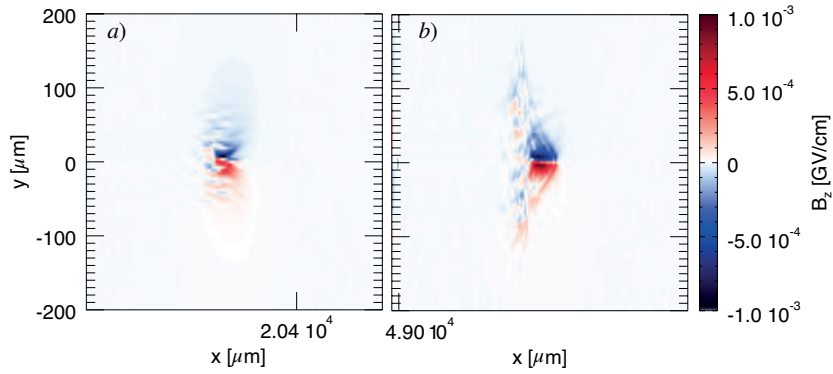
Figure 4.9: Out-of-plane magnetic field B_z after the beam has propagated 2.04 (a) and 4.90 (b) cm into the plasma.
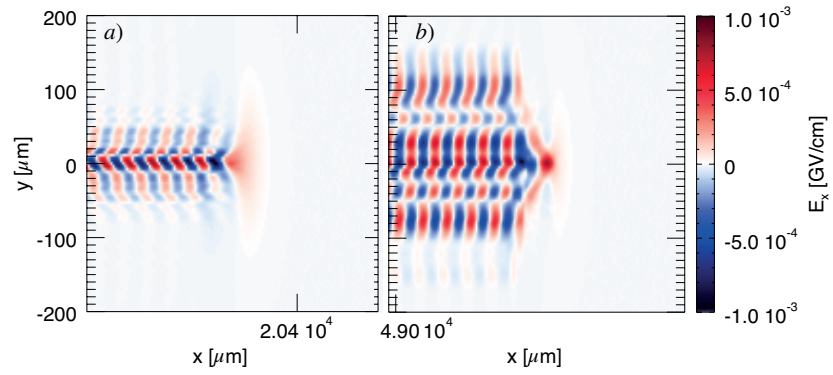

Figure 4.10: Longitudial electric field E_x after the beam has propagated 2.04 (a) and 4.90 (b) cm into the plasma.
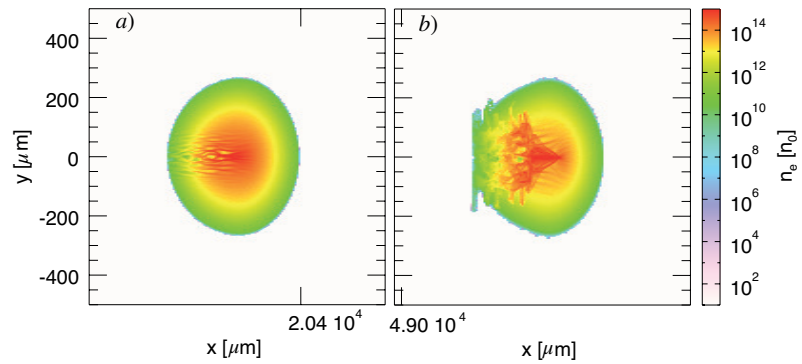

Figure 4.11: Electron beam density after the beam has propagated 2.04 (a) and 4.90 (b) cm into the plasma.

modes has been observed. For the modelled beam parameters, in the absence of a background magnetic field in the beam propagation direction, transverse modes due to the CFI are predominant. When a background magnetic field is considered, the importance of oblique modes over transverse modes increases when increasing the magnetisation level. In any case, the kinetic instabilities triggered by the fireball beam propagation lead to the exponential growth of a magnetic field in the transverse out-of-plane direction. The rate at which this magnetic field grows slows down as the plasma magnetisation level increases. Oblique modes becomes more significant as filaments become more tilted with greater amounts of plasma magnetisation. The effect of longitudinal beam variation was also explored, demonstrating that even less dense, longer longitudinal beams can still cause kinetic instabilities, although the magnetic field grows at a slower rate. For ISM magnetisation levels significantly lower ($\approx$ Gauss) than those considered in this study, a strong magnetic field is generated by the CFI. These findings are useful for understanding the results of Sinha [37], who investigated the polarisation effect of the external magnetic field on the synchrotron radiation produced by a fireball beam. Sinha's research provided valuable insights into the polarisation characteristics influenced by such magnetic fields. However, limited research has been conducted on the structure of the filaments and fields generated by the CFI in an external magnetic field. By elucidating the detailed dynamics of CFI under various magnetisation levels and longitudinal beam variations, this work supports and expands upon Sinha's observations. This deeper understanding of filament structures and magnetic field growth is essential for interpreting the polarisation effects noted by Sinha, particularly in explaining the recent observations of circularly polarised radiation from GRBs.

The second phase of the numerical investigation into CFI involved the examination of CLARA laboratory parameters for the relativistic electron beam. The primary objective of this experiment was to understand if the propagation of the electron beam into the plasma induces the generation of transverse magnetic. The results show the growth of the electric field components and also the transverse magnetic field. Considering the CLARA electron beam parameters is possible to observe that the CFI is the mechanism responsible for magnetic field generation.

Chapter 5

Conclusions and perspectives

5.1 Conclusions

In plasma physics, the development and amplification of magnetic fields in originally unmagnetised plasmas is a long-standing challenge that has relevance to both laboratory studies and astrophysics events. The generation of collisionless shocks in the absence of the ambient magnetic field appears to be caused by the CFI. The observation of GRBs and their afterglows prompted scientific investigations into the filamentation instability, with the goal of understanding how it could account for the substantial increase in magnetic fields necessary for generating the observed electromagnetic spectrum in GRBs. This thesis examines the importance of plasma instabilities in the self-consistent creation of magnetic fields in the astrophysics context as well as the implications for exploring magnetic field structure in beam-plasma interactions. The studies involve a combination of theoretical derivations and numerical simulations. The numerical simulations, specifically, were executed through a kinetic methodology, employing two distinct PIC codes: OSIRIS and ECsim.

Chapter 3 examined the onset and evolution of the CFI driven by two identical counterpropagating plasmas composed of electrons and ions. The 2D simulations were conducted using the ECsim code to evaluate its accuracy in modeling the CFI. The growth rate of the instability was analyzed, yielding a numerical growth rate of $\Gamma^{\mathrm{Num}} = 0.13\,\omega_{\mathrm{pi}}$. This result was compared to the theoretical growth rate $\Gamma^{\mathrm{Th}} = 0.12\,\omega_{\mathrm{pi}}$. The close agreement between these values demonstrates the high accuracy and reliability of the ECsim code in modeling the CFI. The evolution of the magnetic field was analysed for various ion-to-electron mass ratios $m_i/m_e = 200, 400$ and 1000, different initial anisotropy values and drift velocities in a range $v_i = v_e = [0.1 - 0.044]\,c$. The main case analyzed considered the macroscopic parameters of the system with an ion-to-electron mass ratio of $m_i/m_e = 1000$ and ion and electron velocities of $v_i = v_e = \pm 0.044\,c$. The ion-to-electron mass ratio used in the simulations is sufficiently close to the

actual proton-to-electron mass ratio, enabling accurate observation of scale separation effects. The magnetic field generated by the instability maintains its strength over hundreds of plasma periods. Significant changes in ion behavior occur during the initial linear phase of the instability. This phase is characterised by a rapid reduction in ion anisotropy. It is accompanied by the conversion of parallel kinetic energy into perpendicular heating. This phenomenon indicates a dynamic process in which ion motion transitions, influencing energy distribution and thermalisation. After the linear phase of the instability, there is a continuous decrease in ion anisotropy. The significance of anisotropy becomes evident in guiding the long-term behavior of the instability, characterised by the continual coalescence of magnetic filaments. The relationship between mass ratios and the rates at which filaments merge becomes apparent as smaller mass ratios consistently result in accelerated rates of filament coalescence. The magnetic field cascades filaments towards larger and larger spatial scales at different merging rates, depending on the value of m_i/m_e. In all cases investigated, the merging rate is proportional to t^β with β varying between 0.63 and 1.05. As observed, mass ratios significantly influence the dynamics of filament merging. Furthermore, higher drift velocities contribute to a more rapid merging of the filamentary structures.

Chapter 4 utilised 2D kinetic simulations conducted with the OSIRIS code to depict the underlying physics of ultra-relativistic electron-positron fireball beams propagating through a static, slightly magnetised plasma. These simulations involved a uniform background magnetic field $\mathbf{B}_0$ with varying amplitudes, specifically ranging from 0 to 8.5 MG.

An evolution toward a mixture of both purely transverse and oblique modes has been noted. When considering the beam parameters in the absence of a background magnetic field in the direction of beam propagation, the dominant modes are transverse modes attributed to the CFI. However, when incorporating a background magnetic field, the significance of oblique modes relative to transverse modes grows with the increasing level of magnetisation. In any case, kinetic instabilities triggered by the fireball beam's propagation lead to exponential growth of a magnetic field in the transverse out-of-plane direction. The growth rate of this magnetic field slows as the level of plasma magnetisation increases. Simultaneously, oblique modes gain greater significance as filaments tilt more with increasing plasma magnetisation. Additionally, it was illustrated the propagation of a relativistic electron beam within a static and non-magnetised plasma. The numerical investigation of CFI involved exploring potential CLARA laboratory parameters for the relativistic electron beam. The primary goal of this experiment was to determine if the electron beam's entry into the plasma leads to the creation of a transverse magnetic field. The results demonstrate the growth of electric field components and the development of the transverse magnetic field.

5.2 Future work

The research presented in this thesis can serve as a foundation for investigating the formation of magnetic fields in laboratory settings. For an extension of Chapter 3, it would be interesting to investigate on multi-dimensional simulation of finite plasma interactions. Recent studies have demonstrated that during electron-positron plasma collisions, the plasma clouds decelerates. As a result, kinetic energy is transferred to the electromagnetic field through the Weibel instability. Nonetheless, the electron-proton cloud interactions remains unexplored and necessitate further investigation. This study aims to determine if ion Weibel instability contributes to slowing down the clouds further and strengthening the magnetic field. The results of this research are important for understanding how this instability evolves over space and time in systems of finite size. This preliminary research on the fireball beam can give a global comprehension of an external magnetic field on the CFI driven by an ultra-relativistic neutral fireball beam when travelling through a static plasma. The OSIRIS code, which performed the 2D particle-in-cell simulations, has been used to investigate the effects of various magnetic field intensities and the effect of beam flow velocities. A comprehensive experiment will certainly need to be designed using fully 3D simulations. The higher dimension may alter how interactions take place and how powerful the resulting fields are.

Bibliography

[1] T. Piran, "The physics of gamma-ray bursts," *Reviews of Modern Physics*, vol. 76, p. 1143, (2005).

[2] D. A. Uzdensky and S. Rightley, "Plasma physics of extreme astrophysical environments," *Reports on Progress in Physics*, vol. 77, p. 036 902, (2014).

[3] M. V. Medvedev and A. Loeb, "Generation of magnetic fields in the relativistic shock of gamma-ray burst sources," *The Astrophysical Journal*, vol. 526, p. 697, (1999).

[4] M. V. Medvedev, M. Fiore, R. A. Fonseca, L. O. Silva, and W. B. Mori, "Long-time evolution of magnetic fields in relativistic gamma-ray burst shocks," *The Astrophysical Journal*, vol. 618, p. L75, (2004).

[5] A. Bell, "The acceleration of cosmic rays in shock fronts–I," *Monthly Notices of the Royal Astronomical Society*, vol. 182, p. 147, (1978).

[6] A. Grassi, "Collisionless shocks in the context of Laboratory Astrophysics," *Université Pierre et Marie Curie et University of Pisa*, (2017).

[7] Y. Matsumoto, T. Amano, T. N. Kato, and M. Hoshino, "Stochastic electron acceleration during spontaneous turbulent reconnection in a strong shock wave," *Science*, vol. 347, p. 974, (2015).

[8] A. Spitkovsky, "On the structure of relativistic collisionless shocks in electron-ion plasmas," *The Astrophysical Journal*, vol. 673, p. L39, (2007).

[9] L. O. Silva, R. A. Fonseca, J. W. Tonge, J. M. Dawson, W. B. Mori, and M. V. Medvedev, "Interpenetrating plasma shells: Near-equipartition magnetic field generation and nonthermal particle acceleration," *The Astrophysical Journal*, vol. 596, p. L121, (2003).

[10] E. S. Weibel, "Spontaneously growing transverse waves in a plasma due to an anisotropic velocity distribution," *Physical Review Letters*, vol. 2, p. 83, (1959).

[11] B. D. Fried, "On the mechanism for instability of transverse plasma waves," *The Physics of Fluids*, vol. 2, p. 83, (1959).

[12] T. N. Kato and H. Takabe, "Nonrelativistic collisionless shocks in unmagnetized electron-ion plasmas," *The Astrophysical Journal*, vol. 681, p. L93, (2008).

[13] K. Koyama, R. Petre, E. V. Gotthelf, U. Hwang, M. Matsuura, M. Ozaki, and S. S. Holt, "Evidence for shock acceleration of high-energy electrons in the supernova remnant sn1006," *Nature*, vol. 378, p. 255, (1995).

[14] R. Schlickeiser and P. K. Shukla, "Cosmological magnetic field generation by the Weibel instability," *The Astrophysical Journal*, vol. 599, p. L57, (2003).

[15] J. Granot, T. Piran, O. Bromberg, J. L. Racusin, and F. Daigne, "Gamma-ray bursts as sources of strong magnetic fields," *Space Science Reviews*, vol. 191, p. 471, (2015).

[16] R. W. Klebesadel, I. B. Strong, and R. A. Olson, "Observations of gamma-ray bursts of cosmic origin," *The Astrophysical Journal*, vol. 182, p. L85, (1973).

[17] https://gammaray.nsstc.nasa.gov/batse/grb/skymap, "The burst and transient source experiment," (15/05/2023).

[18] J. N. Bahcall and J. P. Ostriker, "Unsolved problems in astrophysics," Princeton University Press, (1997).

[19] J. Hjorth, J. Sollerman, P. Møller, J. P. U. Fynbo, S. E. Woosley, C. Kouveliotou, N. R. Tanvir, J. Greiner, M. I. Andersen, A. J. Castro-Tirado, J. Fruchter A. S. ad Gorosabel, P. Jakobsson, L. Kaper, S. Klose, N. Masetti, H. Pedersen, K. Pedersen, E. Pian, E. Palazzi, J. E. Rhoads, E. Rol, E. P. J. van den Heuvel, P. M. Vreeswijk, D. Watson, and R. A. Wijers, "A very energetic supernova associated with the Gamma-Ray Burst of 29 March 2003," *Nature*, vol. 423, p. 847, (2003).

[20] J. Goodman, "Are gamma-ray bursts optically thick?" *The Astrophysical Journal*, vol. 308, p. L47, (1986).

[21] G. P. Zank and R. G. Greaves, "Linear and nonlinear modes in nonrelativistic electron-positron plasmas," *Physical Review E*, vol. 51, p. 6079, (1995).

[22] N. Shukla, S. F. Martins, P. Muggli, J. Vieira, and L. O. Silva, "Interaction of ultra-relativistic fireball beam with plasma," *New Journal of Physics*, vol. 22, p. 013 030, (2020).

[23] W. Coburn and S. E. Boggs, "Polarization of the prompt Gamma-ray emission from the Gamma-Ray Burst of 6 december 2002," *Nature*, vol. 423, p. 415, (2003).

[24] K. I. Nishikawa, J. Niemiec, P. E. Hardee, M. Medvedev, H. Sol, Y. Mizuno, B. Zhang, M. Pohl, M. Oka, and D. H. Hartmann, "Weibel instability and associated strong fields in a fully three-dimensional simulation of a relativistic shock," *The Astrophysical Journal*, vol. 698, p. L10, (2009).

[25] A. Bret, "Weibel, two-stream, filamentation, oblique, bell, Buneman... which one grows faster?" *The Astrophysical Journal*, vol. 699, p. 990, (2009).

[26] S. Dado, A. Dar, and A. De Rújula, "Critical Tests of Leading Gamma Ray Burst Theories," *Universe*, vol. 8, p. 350, (2022).

[27] H. S. Park, D. D. Ryutov, J. S. Ross, N. L. Kugland, S. H. Glenzer, C. Plechaty, S. M. Pollaine, B. A. Remington, A. Spitkovsky, and L. Gargate, "Studying astrophysical collisionless shocks with counterstreaming plasmas from high power lasers," *High Energy Density Physics*, vol. 8, p. 38, (2012).

[28] N. L. Kugland, D. D. Ryutov, P. Y. Chang, R. P. Drake, G. Fiksel, D. H. Froula, S. H. Glenzer, G. Gregori, M. Grosskopf, and M. Koenig, "Self-organized electromagnetic field structures in laser-produced counter-streaming plasmas," *Nature Physics*, vol. 8, p. 809, (2012).

[29] W. Fox, G. Fiksel, A. Bhattacharjee, P. Y. Chang, K. Germaschewski, S. X. Hu, and P. M. Nilson, "Filamentation instability of counterstreaming laser-driven plasmas," *Physical Review Letters*, vol. 111, p. 225 002, (2013).

[30] C. M. Huntington, F. Fiuza, J. S. Ross, A. B. Zylstra, R. P. Drake, D. H. Froula, G. Gregori, N. L. Kugland, C. C. Kuranz, and M. C. Levy, "Observation of magnetic field generation via the Weibel instability in interpenetrating plasma flows," *Nature Physics*, vol. 11, p. 173, (2015).

[31] J. S. Ross, S. H. Glenzer, P. Amendt, R. Berger, L. Divol, N. L. Kugland, O. L. Landen, C. Plechaty, B. Remington, and D. Ryutov, "Characterizing counter-streaming interpenetrating plasmas relevant to astrophysical collisionless shocks," *Physics of Plasmas*, vol. 19, p. 056 501, (2012).

[32] F. Fiuza, G. F. Swadling, A. Grassi, H. G. Rinderknecht, D. P. Higginson, D. Ryutov, C. Bruulsema, R. P. Drake, S. Funk, and S. Glenzer, "Electron acceleration in laboratory-produced turbulent collisionless shocks," *Nature Physics*, vol. 16, p. 916, (2020).

[33] B. Allen, V. Yakimenko, M. Babzien, M. Fedurin, K. Kusche, and P. Muggli, "Experimental study of current filamentation instability," *Physical Review Letters*, vol. 109, p. 185 007, (2012).

[34] C. M. Huntington, A. G. R. Thomas, C. McGuffey, T. Matsuoka, V. Chvykov, G. Kalintchenko, S. Kneip, Z. Najmudin, C. Palmer, and V. Yanovsky, "Current filamentation instability in laser wakefield accelerators," *Physical Review Letters*, vol. 106, p. 105 001, (2011).

[35] N. Shukla, J. Vieira, P. Muggli, G. Sarri, R. Fonseca, and L. O. Silva, "Conditions for the onset of the current filamentation instability in the laboratory," *Journal of Plasma Physics*, vol. 84, p. 905 840 302, (2018).

[36] G. Sarri, K. Poder, J. M. Cole, W. Schumaker, A. Di Piazza, B. Reville, T. Dzelzainis, D. Doria, L. A. Gizzi, G. Grittani, S. Kar, C. H. Keitel, K. Krushelnick, S. Kuschel, S. P. D. Mangles, Z. Najmudin, N. Shukla, L. O. Silva, D. Symes, A. G. R. Thomas, M. Vargas, J. Vieira, and M. Zepf, "Generation of neutral and high-density electron-positron pair plasmas in the laboratory," *Nature Communications*, vol. 6, p. 6747, (2015).

[37] U. Sinha, C. H. Keitel, and N. Kumar, "Polarized light from the transportation of a matter-antimatter beam in a plasma," *Physical Review Letters*, vol. 122, p. 204 801, (2019).

[38] U. Sinha and N. Kumar, "Pair-beam propagation in a magnetized plasma for modeling the polarized radiation emission from gamma-ray bursts in laboratory astrophysics experiments," *Physical Review E*, vol. 101, p. 063 204, (2020).

[39] K. Wiersema, S. Covino, K. Toma, K. Van Der Horst A.J.and Varela, M. Min, J. Greiner, R. Starling, N. Tanvir, R. Wijers, *et al.*, "Circular polarization in the optical afterglow of GRB 121024A," *Nature*, vol. 509, p. 201, (2014).

[40] H. Chen and F. Fiuza, "Perspectives on relativistic electron–positron pair plasma experiments of astrophysical relevance using high-power lasers," *Physics of Plasmas*, vol. 30, p. 020 601, (2023).

[41] F. Fiuza, R. A. Fonseca, J. Tonge, W. B. Mori, and L. O. Silva, "Weibel-instability-mediated collisionless shocks in the laboratory with ultraintense lasers," *Physical Review Letters*, vol. 108, p. 235 004, (2012).

[42] A. Stockem, F. Fiuza, A. Bret, R. A. Fonseca, and L. O. Silva, "Exploring the nature of collisionless shocks under laboratory conditions," *Scientific Reports*, vol. 4, p. 1, (2014).

[43] A. Grassi, M. Grech, F. Amiranoff, F. Pegoraro, A. Macchi, and C. Riconda, "Electron Weibel instability in relativistic counterstreaming plasmas with flow-aligned external magnetic fields," *Physical Review E*, vol. 95, p. 023 203, (2017).

[44] C. D. Arrowsmith, N. Shukla, N. Charitonidis, R. Boni, H. Chen, T. Davenne, A. Dyson, D. H. Froula, J. T. Gudmundsson, and B. T. Huffman, "Generating ultradense pair beams using 400 GeV/c protons," *Physical Review Research*, vol. 3, p. 023 103, (2021).

[45] N. Shukla, K. Schoeffler, E. Boella, J. Vieira, R. Fonseca, and L. O. Silva, "Interplay between the Weibel instability and the Biermann battery in realistic laser-solid interactions," *Physical Review Research*, vol. 2, p. 023 129, (2020).

[46] C. Zhang, C. K. Huang, K. A. Marsh, C. E. Clayton, W. B. Mori, and C. Joshi, "Ultrafast optical field–ionized gases—A laboratory platform for studying kinetic plasma instabilities," *Science Advances*, vol. 5, eaax4545, (2019).

[47] C. Zhang, J. Hua, Y. Wu, Y. Fang, Y. Ma, T. Zhang, S. Liu, B. Peng, Y. He, and C. Huang, "Measurements of the growth and saturation of electron Weibel instability in optical-field ionized plasmas," *Physical Review Letters*, vol. 125, p. 255 001, (2020).

[48] S. Göde, C. Rödel, K. Zeil, R. Mishra, M. Gauthier, F. E. Brack, T. Kluge, M. J. MacDonald, J. Metzkes, and L. Obst, "Relativistic electron streaming instabilities modulate proton beams accelerated in laser-plasma interactions," *Physical Review Letters*, vol. 118, p. 194 801, (2017).

[49] G. G. Scott, C. M. Brenner, V. Bagnoud, R. J. Clarke, B. Gonzalez-Izquierdo, J. S. Green, R. I. Heathcote, H. W. Powell, D. R. Rusby, B. Zielbauer, P. McKenna, and D. Neely, "Diagnosis of Weibel instability evolution in the rear surface density scale lengths of laser solid interactions via proton acceleration," *New Journal of Physics*, vol. 19, p. 043 010, (2017).

[50] D. R. Rusby, C. D. Armstrong, G. G. Scott, M. King, P. McKenna, and D. Neely, "Effect of rear surface fields on hot, refluxing and escaping electron populations via numerical simulations," *High Power Laser Science and Engineering*, vol. 7, E45, (2019).

[51] M. Tabak, J. Hammer, M. E. Glinsky, W. L. Kruer, S. C. Wilks, J. Woodworth, E. M. Campbell, M. D. P., and R. J. Mason, "Ignition and high gain with ultrapowerful lasers," *Physics of Plasmas*, vol. 1, p. 1626, (1994).

[52] S. Atzeni and J. Meyer-ter-Vehn, "*The physics of inertial fusion: beam plasma interaction, hydrodynamics, hot dense matter*," Oxford Science Publication, (2004).

[53] R. Kodama, P. Norreys, K. Mima, A. E. Dangor, R. G. Evans, H. Fujita, Y. Kitagawa, K. Krushelnick, T. Miyakoshi, and N. Miyanaga, "Fast heating of ultrahigh-density plasma as a step towards laser fusion ignition," *Nature*, vol. 412, p. 798, (2001).

[54] P. A. Norreys, R. Scott, K. Lancaster, J. Green, A. Robinson, M. Sherlock, R. Evans, M. G. Haines, S. Kar, and M. Zepf, "Recent fast electron energy transport experiments relevant to fast ignition inertial fusion," *Nuclear Fusion*, vol. 49, p. 104 023, (2009).

[55] L. O. Silva, R. A. Fonseca, J. W. Tonge, W. B. Mori, and J. M. Dawson, "On the role of the purely transverse Weibel instability in fast ignitor scenarios," *Physics of Plasmas*, vol. 9, p. 2458, (2002).

[56] S. Atzeni, "Physics of Fast Ignition and target studies for the HiPER project," *IOP Plasma Physics Group Annual Meeting*, (2018).

[57] C. K. Birdsall and A. B. Langdon, "*Plasma physics via computer simulation*," CRC Press, (2004).

[58] R. W. Hockney and J. W. Eastwood, "*Computer simulation using particles*," Institute of Physics Publishing, (1988).

[59] J. M. Dawson, "Particle simulation of plasmas," *Reviews of Modern Physics*, vol. 55, p. 403, (1983).

[60] T. H. Stix, "*Waves in plasmas*," Springer Science & Business Media, (1992).

[61] C. Z. Cheng and G. Knorr, "The integration of the Vlasov equation in configuration space," *Journal of Computational Physics*, p. 330, (1976).

[62] R. L. Liboff, "*Kinetic theory: classical, quantum, and relativistic descriptions*," Springer Science & Business Media, (2003).

[63] G. Lapenta, "Particle simulations of space weather," *Journal of Computational Physics*, vol. 231, p. 795, (2012).

[64] J. Villasenor and O. Buneman, "Rigorous charge conservation for local electromagnetic field solvers," *Computer Physics Communications*, vol. 69, p. 306, (1992).

[65] A. Taflove, "*Computational electrodynamics: The finite-difference time-domain method*," Artech House, (2005).

[66] R. Courant, K. Friedrichs, and H. Lewy, "On the partial difference equations of mathematical physics," *IBM Journal of Research and Development*, vol. 11, p. 215, (1967).

[67] B. B. Godfrey, "Numerical Cherenkov instabilities in electromagnetic particle codes," *Journal of Computational Physics*, vol. 15, p. 504, (1974).

[68] E. Isaacson and H. B. Keller, "*Numerical Analysis and numerical methods*," Courier Corporation, (1994).

[69] ——, "*Analysis of numerical methods*," Courier Corporation, (2012).

[70] D. Tskhakaya, K. Matyash, R. Schneider, and F. Taccogna, "The Particle-In-Cell Method," *Contributions to Plasma Physics*, vol. 47, p. 563, (2007).

[71] D. C. Barnes and L. Chacón, "Finite spatial-grid effects in energy-conserving particle-in-cell algorithms," *Computer Physics Communications*, vol. 258, p. 107 560, (2021).

[72] J. Brackbill and G. Lapenta, "A method to suppress the finite-grid instability in plasma simulations," *Journal of Computational Physics*, vol. 114, p. 77, (1994).

[73] M. D. Meyers, C. K. Huang, Y. Zeng, S. A. Yi, and B. J. Albright, "On the numerical dispersion of electromagnetic particle-in-cell code: Finite grid instability," *Journal of Computational Physics*, vol. 297, p. 565, (2015).

[74] R. A. Fonseca, L. O. Silva, F. S. Tsung, V. K. Decyk, W. Lu, C. Ren, W. B. Mori, S. Deng, S. Lee, T. Katsouleas, and J. C. Adam, "OSIRIS: A three-dimensional, fully relativistic particle in cell code for modelling plasma-based accelerators," *International Conference on Computational Science*, vol. 2331, p. 342, (2002).

[75] R. A. Fonseca, S. F. Martins, L. O. Silva, J. W. Tonge, F. S. Tsung, and W. B. Mori, "One-to-one direct modelling of experiments and astrophysical scenarios: Pushing the envelope on kinetic plasma simulations," *Plasma Physics and Controlled Fusion*, vol. 50, p. 124 034, (2008).

[76] J. P. Boris, "*Relativistic plasma simulation-optimization of a hybrid code,*" Proceeding of Fourth Conference on Numerical Simulations of Plasmas, (1970).

[77] F. Li, P. Yu, X. Xu, F. Fiuza, V. K. Decyk, T. Dalichaouch, A. Davidson, A. Tableman, W. An, F. S. Tsung, R. A. Fonseca, W. Lu, and W. B. Mori, "Controlling the numerical Cherenkov instability in PIC simulations using a customized finite difference Maxwell solver and a local FFT based current correction," *Computer Physics Communications*, vol. 214, p. 6, (2017).

[78] F. Li, K. Miller, X. Xu, F. S. Tsung, V. K. Decyk, W. An, R. A. Fonseca, and W. B. Mori, "A new field solver for modeling of relativistic particle-laser interactions using the particle-in-cell algorithm," *Computer Physics Communications*, vol. 258, p. 107 580, (2021).

[79] S. Markidis and G. Lapenta, "The energy conserving particle-in-cell method," *Journal of Computational Physics*, vol. 230, p. 7037, (2011).

[80] D. Gonzalez-Herrero, E. Boella, and G. Lapenta, "Performance analysis and implementation details of the Energy Conserving Semi-Implicit Method code (ECsim)," *Computer Physics Communications*, vol. 229, p. 162, (2018).

[81] J. U. Brackbill and D. W. Forslund, "An implicit method for electromagnetic plasma simulation in two dimensions," *Journal of Computational Physics*, vol. 46, p. 271, (1982).

[82] A. B. Langdon, B. I. Cohen, and A. Friedman, "Direct implicit large time-step particle simulation of plasmas," *Journal of Computational Physics*, vol. 51, p. 107, (1983).

[83] G. Lapenta, D. Gonzalez-Herrero, and E. Boella, "Multiple-scale kinetic simulations with the energy-conserving semi-implicit particle in cell method," *Journal of Plasma Physics*, vol. 83, (2017).

[84] G. Lapenta, "Exactly energy conserving semi-implicit particle in cell formulation," *Journal of Computational Physics*, vol. 334, p. 349, (2017).

[85] D. Gonzalez-Herrero, A. Micera, E. Boella, J. Park, and G. Lapenta, "ECsimcyl: Energy Conserving Semi-Implicit particle in cell simulation in axially symmetric cylindrical coordinates," *Computer Physics Communications*, vol. 236, p. 153, (2019).

[86] D. W. Hewett and C. W. Nielson, "A multidimensional quasineutral plasma simulation model," *Journal of Computational Physics*, vol. 29, p. 219, (1978).

[87] D. Burgess, D. Sulsky, and J. Brackbill, "Mass matrix formulation of the FLIP particle-in-cell method," *Journal of Computational Physics*, vol. 103, p. 1, (1992).

[88] A. Bret, L. Gremillet, and M. E. Dieckmann, "Multidimensional electron beam-plasma instabilities in the relativistic regime," *Physics of Plasmas*, vol. 17, p. 120 501, (2010).

[89] B. D. Fried and S. D. Conte, "*The plasma dispersion function: the Hilbert transform of the Gaussian,*" Academic Press, (2015).

[90] R. C. Davidson, D. A. Hammer, I. Haber, and C. E. Wagner, "Nonlinear development of electromagnetic instabilities in anisotropic plasmas," *The Physics of Fluids*, vol. 15, p. 317, (1972).

[91] S. Wolfram, "Wolfram research, inc., mathematica, version 9.0," (2012).

[92] R. Kumar, D. Eichler, and M. Gedalin, "Electron heating in a relativistic, Weibel-unstable plasma," *The Astrophysical Journal*, vol. 806, p. 165, (2015).

[93] A. Achterberg and J. Wiersma, "The Weibel instability in relativistic plasmas-I. Linear theory," *Astronomy & Astrophysics*, vol. 475, p. 1, (2007).

[94] C. Ruyer, L. Gremillet, A. Debayle, and G. Bonnaud, "Nonlinear dynamics of the ion Weibel-filamentation instability: An analytical model for the evolution of the plasma and spectral properties," *Physics of Plasmas*, vol. 22, p. 032 102, (2015).

[95] C. Ruyer and F. Fiuza, "Disruption of current filaments and isotropization of the magnetic field in counterstreaming plasmas," *Physical Review Letters*, vol. 120, p. 245 002, (2018).

[96] M. Zhou, N. F. Loureiro, and D. A. Uzdensky, "Multi-scale dynamics of magnetic flux tubes and inverse magnetic energy transfer," *Journal of Plasma Physics*, vol. 86, p. 535 860 401, (2020).

[97] M. Takamoto, Y. Matsumoto, and T. N. Kato, "Magnetic field saturation of the ion Weibel instability in interpenetrating relativistic plasmas," *The Astrophysical Journal Letters*, vol. 860, p. L1, (2018).

[98] T. N. Kato, "Saturation mechanism of the Weibel instability in weakly magnetized plasmas," *Physics of Plasmas*, vol. 12, p. 080 705, (2005).

[99] S. P. Davis, R. Capdessus, E. d'Humières, S. Jequier, I. Andriyash, and V. Tikhonchuk, "Numerical simulations of energy transfer in counter-streaming plasmas," *High Energy Density Physics*, vol. 9, p. 231, (2013).

[100] C. Ruyer, L. Gremillet, G. Bonnaud, and C. Riconda, "Analytical predictions of field and plasma dynamics during nonlinear Weibel-mediated flow collisions," *Physical Review Letters*, vol. 117, p. 065 001, (2016).

[101] M. Lemoine, L. Gremillet, G. Pelletier, and A. Vanthieghem, "Physics of Weibel-mediated relativistic collisionless shocks," *Physical Review Letters*, vol. 123, p. 035 101, (2019).

[102] G. Lapenta, J. U. Brackbill, and P. Ricci, "Kinetic approach to microscopic-macroscopic coupling in space and laboratory plasmas," *Physics of Plasmas*, vol. 13, p. 055 904, (2006).

[103] V. Yakimenko, Alsberg, L, E. Bong, G. Bouchard, C. Clarke, C. Emma, S. Green, C. Hast, M. J. Hogan, J. Seabury, N. Lipkowitz, and G. Yocky, "FACET-II facility for advanced accelerator experimental tests," *Physical Review Accelerators and Beams*, vol. 22, p. 101 301, (2019).

[104] D. Angal-Kalinin, A. Bainbridge, A. D. Brynes, R. Buckley, S. Buckley, G. Burt, R. Cash, H. C. Cortes, D. Christie, J. A. Clarke, *et al.*, "Design, specifications, and first beam measurements of the compact linear accelerator for research and applications front end," *Physical Review Accelerators and Beams*, vol. 23, p. 044 801, (2020).

[105] J. Gold, "Relativistic jet interaction with plasma," *Lancaster University*, (2021).

[106] A. Bret, M. C. Firpo, and C. Deutsch, "Characterization of the initial filamentation of a relativistic electron beam passing through a plasma," *Physical Review Letters*, vol. 94, p. 115 002, (2005).